FABRICATION AND CHARACTERIZATION OF ALUMINIUM BASED FUNCTIONALLY GRADED COMPOSITES VIA FRICTION STIR PROCESSING

A thesis submitted in partial fulfilment of the requirements for the award of the Degree of

DOCTOR OF PHILOSOPHY
in
MECHANICAL ENGINEERING

Bikkina Venkatesh
(Roll No: 716129)

Supervisor
Dr. T. Sadasiva Rao

and

Co-Supervisor
Prof. Adepu Kumar

DEPARTMENT OF MECHANICAL ENGINEERING
NATIONAL INSTITUTE OF TECHNOLOGY,
WARANGAL (TS) - 506004, INDIA.

2021

CERTIFICATE

This is to certify that the dissertation work entitled **"Fabrication and Characterization of Aluminium based Functionally Graded Composites via Friction stir processing"**, which is being submitted by **Mr. B. Venkatesh** (Roll No. 716129), is a bonafide work submitted to the Department of Mechanical Engineering, National Institute of Technology, Warangal in partial fulfillment of the requirement for the award of the degree of **Doctor of Philosophy in Mechanical Engineering.**

To the best of our knowledge, the work incorporated in this thesis has not been submitted elsewhere for the award of any degree.

Dr. T.Sadasiva Rao
Supervisor
Department of Mechanical Engineering
National Institute of Technology
Warangal- 506004

Prof. Adepu Kumar
Co-supervisor
Department of Mechanical Engineering
National Institute of Technology
Warangal-506004

Prof. Adepu Kumar
Head
Department of Mechanical Engineering
National Institute of Technology
Warangal- 506004

Dedicated

To

My beloved mother and brother

APPROVAL SHEET

This Thesis entitled **"Fabrication and Characterization of Aluminium based Functionally Graded Composites via Friction stir processing"**, by **B. Venkatesh** is approved for the **Degree of Doctor Philosophy**

Examiners

Supervisor	**Co-supervisor**
Dr. T.Sadasiva Rao	**Prof.Adepu Kumar**
(Assistant Professor. MED)	**(Professor. MED)**

Chairman

Prof. A. Kumar, MED, NIT
WARANGAL

DECLARATION

This is to certify that the work presented in the thesis entitled **"Fabrication and Characterization of Aluminium based Functionally Graded Composites via Friction stir processing"** is a bonafide work done by me under the supervision of Dr T.Sadasiva Rao and Prof. Adepu Kumar, and was not submitted elsewhere for the award of any degree.

I declare that this written submission represents my ideas in my own words and where others' ideas or words have been included, I adequately cited and referenced the sources. I also declare that I have adhered to all principles of academic honesty and integrity and have not misrepresented or fabricated or falsified any idea/data/fact/source in my submission. I understand that any violation of the above will be a cause for disciplinary action by the Institute and can also evoke penal action from the sources which have thus not been properly cited or from whom proper permission has not been taken when needed.

B. Venkatesh
Roll No.: 716129
Date: 03-12-2021

ACKNOWLEDGMENT

I would like to express my sincere thanks and gratitude to my supervisor(s), Dr. T.Sadasiva Rao and Prof. Adepu Kumar, Mechanical Engineering Department, National Institute of Technology, Warangal, for his continuous guidance, support, enthusiasm, and motivation in my Ph.D. research work.

Besides my supervisor, I would like to thank the rest of my Doctoral scrutiny committee: Prof.A.Venugopal and Prof.K.V.S Srinadh (Mechanical Engineering Department), and Dr.Asit Kumar Khanra (Materials and Metallurgical Engineering Department), for their insightful comments and encouragement, but also for the hard questions which incented me to widen my research from various perspectives.

I wish to sincerely thank university authorities, Prof. N.V. RAMANA RAO, Director, National Institute of Technology, Warangal and other top officials who gave me an opportunity to carry out research work.

I also sincerely thank Prof.Adepu Kumar, Head of the Department of Mechanical Engineering, National Institute of Technology, Warangal for his continuous support towards carrying out research work. I would like to extend my thanks to all the faculty members in the Department of Mechanical Engineering Department for their valuable suggestions and encouragement. I am also thankful to all the supporting and technical staff of the Department of Mechanical Engineering who has directly or indirectly helped during the course of my work.

I express my heart-felt gratitude to Dr. M Raja Vishwanathan, (Humanities & Social Science Department) for his endless help and support during this work.

I would like to express my sincere thanks to my fellow lab mates Mr. K.Nagu, Mr. K.Kranthi Kumar, Mr. M.Satyanarayana and Mr. R.Shasidhar for their wholehearted support during the entire tenure for the successful completion of the work.

I owe a lot to my beloved friends Mr. Abeyram M. Nithin, Mr. Santanu Saisdharan, Mr. K Madhu Kishore Raghunath and Mr.G. Kalyan Ramana (IIT Hyderabad) who encouraged and extended their helping arms towards me at every stage of my personal and academic life and longed to see this achievement come true.

Words are inadequate to express my gratitude to all my family members especially Bikkina Uma Maheswari (Mother), Bikkina Harish (Brother), who constantly stood as a source of happiness, encouragement, confidence and untiring support.

(Bikkina Venkatesh)

ABSTRACT

Functionally graded materials (FGM) are a new class of engineering materials which exhibit spatial gradation in composition and/or structure in preferred orientation. The gradual variation in composition produces superior mechanical properties without any poor interface. It eliminates sharp interfaces that exist in traditional composite materials which leads to failure. Due to these drawbacks, these materials have the potential to minimize thermal and residual stress concentrations in various engineering applications and service environments. With the help of FGM, designers can tailor the material responses accordingly to satisfy the design criteria. The unique characteristic feature of FGM is the ability to customize a material for specific function and application. FGM find wide applications in defense, medical, aerospace, optoelectronics etc.

In this investigation, the reinforcement particles were incorporated in the base matrix to create microstructural gradient along the depth. An attempt was made to develop a novel method of tailor-made functionally graded Al/SiC composite by placing SiC particles in pre-prepared square-shaped grooves. The results indicated that the increase in FSP pass number causes better and uniform dispersion of SiC particles. The microhardness values were influenced by the number of passes and improved for pass-3 when compared to as-received 6082-Al. Wear resistance of Al/SiC FG samples also increased as a result of the addition of SiC particles.

To reduce the pass number and predict the variation in the volume percentage of SiC particles in FGM, Al/SiC compositional gradient was created with a newly designed hybrid tool over a predefined length as per the developed process model. The new approach involved a mathematical model for positioning the holes in such a manner that the composition of the reinforcement (SiC) varied from maximum to minimum over a given length. Two tools with different pin profiles: conventional tool (CON) and hybrid tool (HYB), were employed for the process. The CON tool consisted of threads with zero flats while the HYB tool was a combination of threaded part and square (four flats) cross-section. The impact of pin profiles on the dispersion of SiC particles in the stir zone (SZ) of the processed specimens was studied and it was found be to more effective with HYB tool. This was because of the pulsating action induced by the flat edges and flow of material in downward direction. The HYB tool showed a 6.03% improvement in tensile strength vis-à-vis the sample processed by the CON tool as evidenced by mechanical properties and validated by electron backscatter diffraction analysis. The sizes of the grain in SZ for CON and HYB tools were 4.8 μm and 2.7 μm respectively and

a huge fraction of high angle boundaries was observed in the HYB tool when compared to CON tool. The corrosion and wear resistance of FG samples also improved with the addition of SiC particles. The FG sample fabricated with HYB tool demonstrated superior corrosion resistance. Due to the selective dissolution of the reinforcement particle-matrix interface, the localized corrosion protection of FG samples prepared using the HYB tool was better than that achieved by CON tool FG sample. The wear resistance of FG sample fabricated with HYB tool had enhanced because of uniform dispersion of reinforcing ceramic particles in the matrix with significant increase in hardness and strong interfacial bonding of reinforcing ceramic particles in the matrix.

TABLE OF CONTENTS

LIST OF FIGURES

LIST OF TABLES

Abbreviations and Symbols

AISI	American Iron and Steel Institute
Al	Aluminium
AM	Additive Manufacturing
AMMC	Aluminium Metal Matrix Composites
AS	Advancing Side
ASTM	American Society for Testing and Materials
AWS	American Welding Society
B_4C	Boron Carbide
BM	Base Material
CAD	Computer Aided Design
CCD	Charged Coupled device
CMNC	Ceramic Matrix Nanocomposites
CON	Conventional Tool
CVD	Chemical Vapor Deposition
D	Drilled hole diameter
DXR	Dynamically Recrystallized Region
DXZ	Dynamic Recrystallization
EBSD	Electron Back Scatter Diffraction
EBW	Electron Beam Welding
EDAX	Energy dispersive X-ray spectroscopy
EDM	Electric Discharge Machining
EDS	Energy dispersive spectroscopy
EL	Elongation
EN	European Norms
FE	Finite Element Analysis
FGM	Functionally Graded Materials
FSP	Friction Stir Processing
FSVP	Friction Stir Vibration Assisted Processing

FSW	Friction Stir Welding
GBM	Grain Boundary Misorientation
GND	Geometrically Necessary Dislocations
GTAW	Gas Tungsten Arc Welding
HAGB	High Angle Grain Boundaries
HAZ	Heat Affected Zone
HCP	Hexagonal Close Packing
HYB	Hybrid Tool
K_{max}	Maximum composition
K_{min}	Minimum composition
LAGB	Low Angle Grain Boundaries
LBW	Laser Beam Welding
LCD	Liquid Crystal Display
LM	Layered Manufacturing
L_p	Length of the pin
MIG	Metal Inert Gas
MMC	Metal Matrix Composites
MMNC	Metal Matrix Nanocomposites
MoS_2	Molybdenum disulfide
MWCNT	Multi-walled Carbon Nano Tubes
NCFSW	Numerically Controlled Friction Stir Welding
NZ	Nugget Zone
OCP	Open Circuit Potential
PM	Powder Metallurgy
PMNC	Polymer Matrix Nanocomposites
POD	Pin on Disc
R_a	Surface roughness
RHA	Rice Husk Ash
RP	Rapid Prototyping

RS	Retreating Side
SCE	Saturated Calomel Electrode
SEM	Scanning Electron Microscope
SFF	Solid Free Fabrication
SFSP	Submerged Friction Stir Processing
SiC	Silicon Carbide
SMMC	Surface Metal Matrix Composites
SPD	Severe Plastic Deformation
SPS	Spark Plasma Sintering
SZ	Stir Zone
TiB_2	Titanium diboride
TiC	Titanium Carbide
TIG	Tungsten Inert Gas
TMAZ	Thermo Mechanically Affected Zone
TWI	The Welding Institute
UFG	Ultra-Fine Grained
UTM	Universal Testing Machine
UTS	Tensile strength
WC	Tungsten Carbide
XRD	X-Ray Diffraction
YS	Yield strength
δl_i	Grid length

Chapter-1

Introduction

1.1. History and development of welding

About 3000 years ago, the Egyptians started the concept of joining when they joined a piece of iron with the help of forging. Several war weapons, tools and household appliances from the Egyptians represent the finest examples of forge-welded equipment. Around 2000 years ago, during the Bronze Age, round gold boxes were made by pressure welding. In the Middle Ages, numerous objects were made from iron and other metals. The iron pillar of Delhi in India is one of the finest examples of the largest welds in the 17th century. Commercial welding techniques were invented in various parts of the world in the 19th century.

In the mid-18th century, Sir Humphrey Davies created an arc between two electrodes using a battery and invented an electrical generator. However, this method (arc lighting) became popular in the mid-18th century. Arc welding, gas welding, and cutting were studied in the early 19th century. The first U.S. patent was by C.L. Coffin for arc welding processes using a metal electrode in 1892. An electric arc is used to transfer the metal over the line of joint with the help of an electrode. During the same period, gas welding and cutting were promoted by installing an external blowpipe to supply oxygen and later to liquefy air.

The demand for welding metals expanded dramatically during World War-I, that led to the invention of new welding and joining techniques to meet the demand in the United States (US) and Europe. After the war in 1919, the American Welding Society (AWS) was founded with the goal of advanced welding and allied processes. In 1920 automatic welding and various types of electrodes with and without coating were developed. In 1941, Heliarc welding (helium for shielding) was invented and patented by Meredith. Gas shielded welding was developed by the Battelle Memorial Institute in 1948. The same principle was used in gas tungsten arc welding (GTAW) by replacing the tungsten electrode. Many welding techniques were later developed to improve their applications. Electron beam welding was developed in 1940 by the French Atomic Energy Commission. In this welding technique, electrons were employed as a source of vacuum heat.

Friction welding was developed in the Soviet Union and later approved in the USA and Great Britain. Laser beam welding was first developed as a communicator at Bell Telephone Laboratories and later improved towards welding. In 1991, the Welding Institute (TWI) in Cambridge developed a new type of solid-state welding process called friction stir welding (FSW) for joining similar and dissimilar metals.

1.2. Fusion and Solid-State Welding methods

Currently there are several welding/joining techniques available and when demand arises, more welding/joining techniques will be established and will be incorporated into metal working operations. Several welding/joining techniques are currently available and as demand increases additional welding/joining techniques will be developed and integrated into metal working operations. The welding/joining techniques are categorised into two groups, namely, solid-state welding and fusion welding. In fusion welding technique, melting of parent material occurs and only a few welding processes necessitate the use of consumable electrode/filler wire rolls.

The use of consumable for joining/welding is necessary for few welding techniques (such as tungsten inert gas (TIG), metal inert gas (MIG), laser beam welding (LBW) and electron beam welding (EBW). These welding techniques work under high-temperature conditions, which leads to the formation of unfavourable phase at the joint/weld. The formation of unfavourable phase decreases metallurgical and mechanical properties of the weld. Solid-state processes were introduced to overcome the drawbacks in fusion welding processes [1,2].

Solid-state welding processes have several advantages over fusion welding processes. In solid-state welding, the joining takes place below the melting temperature of the metal. It means there is no chance of formation of unfavourable phases at the line of joint and no filler materials/electrodes are required for joining the metals. No inert gas/ vacuum is required to join metal because it operates below melting temperature of the base metal. Explosive welding, hot pressure welding, forge welding, friction welding, friction surfacing and friction stir welding etc. fall under the category of solid-state welding. Dissimilar metal joining may be possible with solid-state welding processes.

1.3. Friction stir welding

Friction stir welding (FSW) is one of the most innovative solid state welding techniques for welding of Al alloys. FSW was invented in 1991 and patented by The Welding Institute (TWI) Cambridge, United Kingdom [3,4]. It is the most promising welding technology for aluminum alloys and is also being expanded to join various materials such as Mg, Cu, steel, Ti, polymers, etc. In FSW, a rotating tool (with a shoulder having profiled pin) is plunged into the joining line between two metal plates and transverses along the line of joint. The frictional heat produced by the rotating tool plasticizes the material around the tool and forms a joint.

During the joining process, the material around the pin undergoes severe plastic deformation (SPD) and travels towards the retreating side (RS) from beneath the pin on the advancing side (AS) where it is forged to form the joint. This consequently leads to solid-state bond between two plates. The schematic diagram of FSW is shown in Fig.1.1

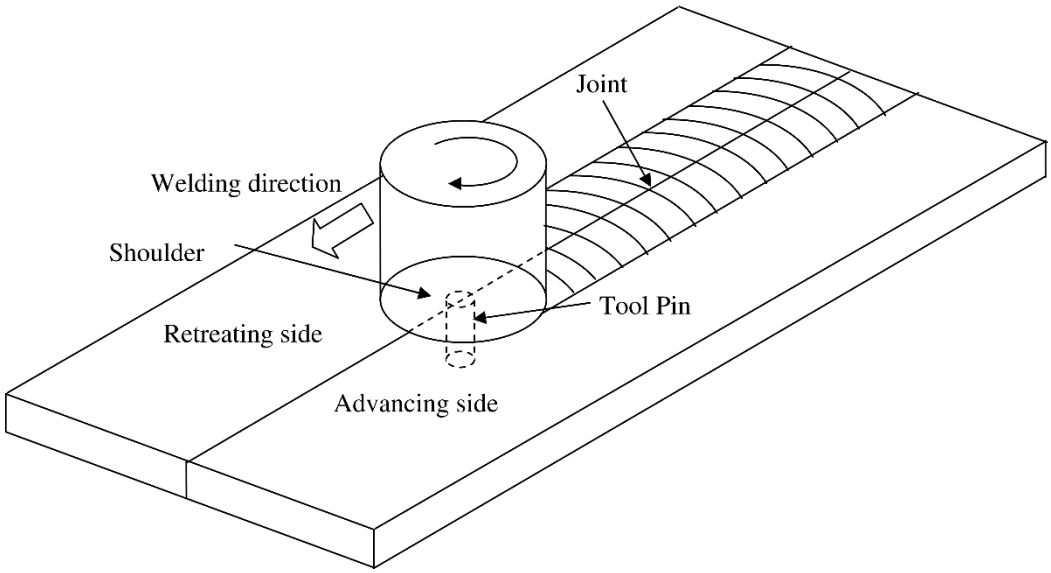

Fig. 1.1 Schematic diagram of FSW[5]

1.3.1. Process parameters

FSW is considered to be a combination of extrusion, forging and stirring the material that creates high strain rate and temperature. In addition, the process involves complex movement of material and intense plastic deformation. In order to identify the effective process parameters of FSW on the quality of the joining process, the Ishikawa cause-and-effect diagram was created and shown in Fig.1.2. The main process parameters are tool geometry, tool rotational speed, transverse speed, axial force and tilt angle.

In FSW, the frictional heat is generated between the tool and base material plate. The tool geometry plays a vital role for the generation of this frictional heat. Improper tool geometry selection results in the formation of defects along the joint. In most cases, the defects occur due to the lack of heat generation in FSW. Tool rotational speed and transverse speed are the main parameters to generate enough heat. Insufficient axial force results in formation of improper joint with defects. Setting a suitable tilting angle in the welding direction ensures that the material is mechanically trapped more efficiently by the tool shoulder. The tilt angle of the tool offers sufficient space for the plasticized material to travel around the processed region and leads to good sound welds.

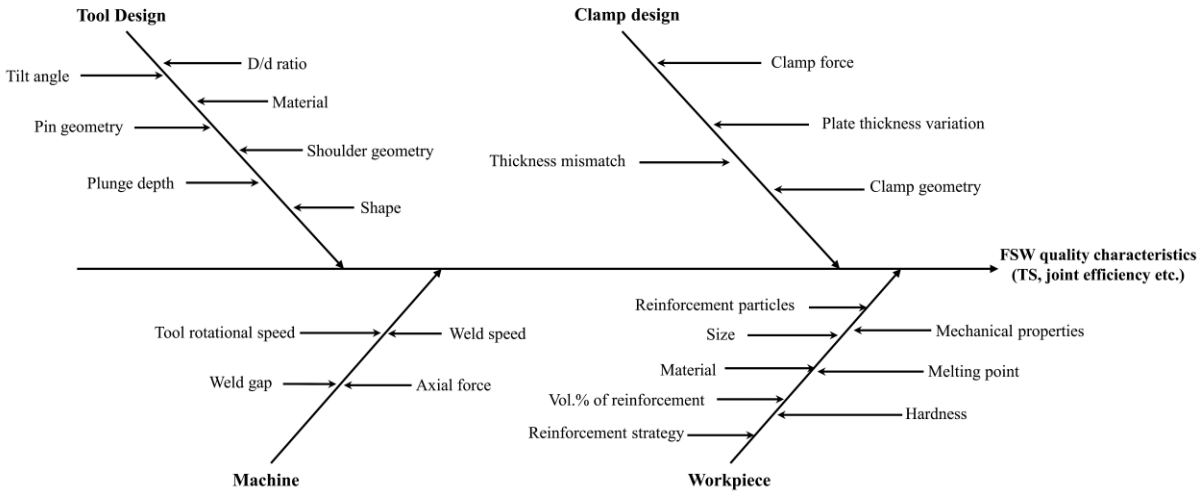

Fig. 1.2. Cause-effect diagram

1.3.2. Tool geometry

In FSW, tool geometry plays an influential role for the generation of frictional heat. The frictional heat is required for plasticization of material, grain recrystallization and formation of weld. It is critical in tool design that flow of material has sufficient direction and quantity during welding. In general, the larger the volume of material to be stirred, the better the welding quality, which, however, correlates strongly with other technological parameters (rotational speed, welding speed). There will certainly be a horizontal flow of material during welding, but if some oxide appears on the surface of the base material, the vertical flow of material will be very strong, and this is especially true with lap welding. When there is no vertical flow during welding, the oxide layer remains on or at the joint line [6–8]. Figure 1.4 a and b depicts the vertical and horizontal flow of the material around the tool

FSW tool mainly consists of shoulder and pin as depicted in Fig.1.3

The basic functions of the tool are as follows:

1. Heat generation
2. Plasticization of material to fabricate the joint
3. Control the material flow within the processed region

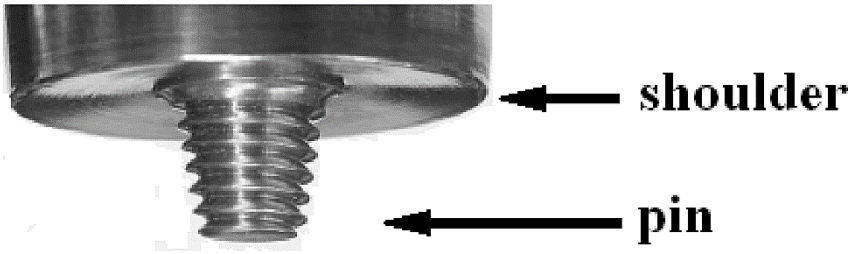

Fig. 1.3. FSW tool with shoulder and pin[9]

Initially, when the tool is plunged, heat is generated due to the contact between the tool and the workpiece. During the plunging action, high amount of heat is generated that plasticizes the material. This continues until the tool shoulder contacts the surface of the workpiece. The second function of the tool is to 'stir' and 'move' the material. The plastic deformation and frictional heating of the workpiece are required to stir the material and is influenced by the design of FSW tool. The majority of the heat during the process is generated with the aid of shoulder, which exerts downward force on the surface of workpiece, compressing the plasticized material around the tool pin. Additionally, it prevents escape of the plasticized material from the workpiece joint line. The shoulder and pin diameter; tool pin profile and pin length; and shoulder profile are important parameters for determining weld quality. Another important parameter is the tool material, which determines the suitability of a tool for a specific application [10].

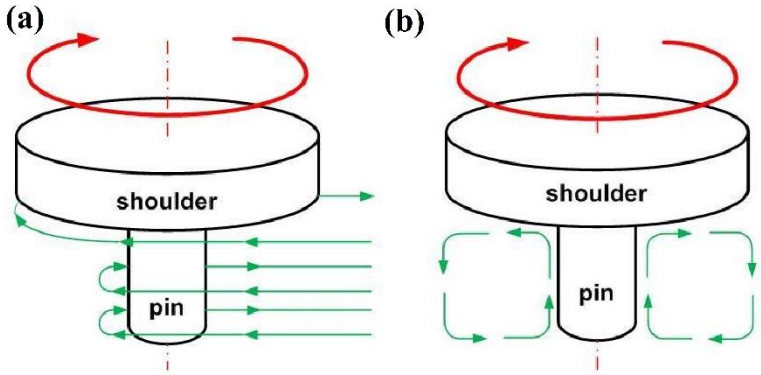

Fig. 1.4. (a) Flow of material in horizontal direction (b) Flow of material in vertical direction[8]

1.3.3. Tool shoulder geometry

The tool shoulder performs the frictional heating and deformation during the welding of thin metal plates. The tool shoulder profiles are designed with geometric features to enhance the interaction between workpiece and the tool shoulder. This improves the plastic deformation

induced by the tool shoulder, which leads to better material mixing and welding quality. The most typical shoulder outer surfaces are shown in Fig.1.5 [11]. Various shoulder features such as concave shoulder (serves as a reservoir for the forging action of the shoulder), scrolls, ridges or knurling, grooves and concentric circles, convex shoulders have been developed. The concave shoulder shape is proficient to produce simple and good sound welds. It also restricts plasticized material from the sides of the shoulder [12].

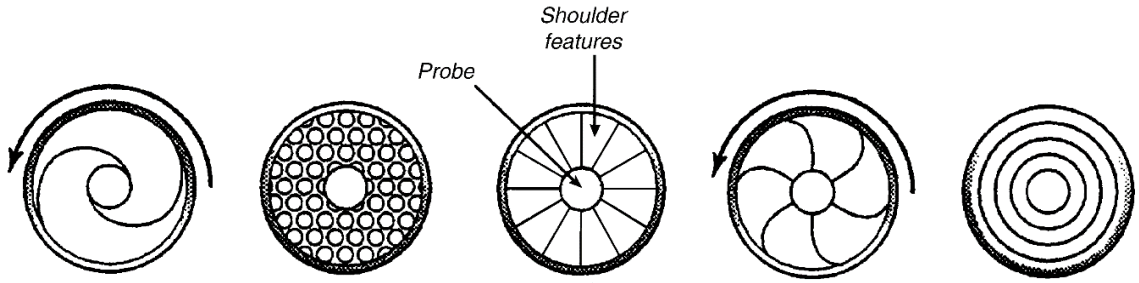

Fig. 1.5. Different tool shoulder geometries [10]

1.3.4. Tool pin geometry

The tool pin is designed to enhance the subsurface flow of material and heat generation. The tool pin is mainly responsible for controlling the welding speed and deformation depth. In addition, its geometry influences the plasticized flow of material and joint performance. In addition, the deformation depth and tool speed are determined by the pin design. The most commonly used pin designs are [13–15]:

Cylindrical pin with round bottom

A rounded end of the pin tool reduces tool wear during plunging and improves the strength of weld root directly below the pin base. The best radius of the dome was given as 75% of diameter of the pin. It was claimed that the smaller the dome radius, the higher the chance of a poor-quality weld, especially just below the pin. Machining a radius at the thread root increases tool life by eliminating stress concentrations at the thread root.

Flat-bottom cylindrical pin

The frictional velocity of rotating cylinder changes from zero in the centre of the cylinder to highest value at the cylinder ends. The local velocity combined with the coefficient of friction between the tool pin and the plate determines the deformation during stirring. The lowest point

of the flat-bottomed pin inclined at a low angle normal to the tool axis to end of the pin where the speed is maximum.

Truncated cone pin

A simple alteration of a cylindrical pin is truncated cone pin. The cylindrical pins were used for welding aluminum alloy plate with a thickness of 12mm. However, the researchers wanted to weld thicker sheets at higher travel speeds using friction stir welding. Cone pins have lower transverse loads than cylindrical pins, and the largest moment load is at the base of the cone.

After the basic pin geometries are described, tool development continued and later, unusual pin geometries were created (refer Fig.1.6):

MX triflute pin

It contains three flutes connected to a helical ridge. They reduce the displaced volume of a pin by about 70% and provide additional deformation. It can be employed to weld thicker section of aluminium alloys.

A-skew TM

The pin geometry is similar to the design of MX triflute. It allows for better weld properties and faster travel speeds. It also reduces asymmetry in the welds.

Trivex pin

In comparison to an MX triflute pin of comparable dimensions, it produced a reduction of 18 to 25% in traversing forces and a 12% decrease in forging (normal) forces.

Threadless pins

These are useful in certain FSW applications where features of the thread would not survive without excessive wear or fracture. Tools operated in aggressive environments cannot maintain the properties of threading tools without excessive pin wear. The tool pin for these conditions usually composed of simple design with robust features.

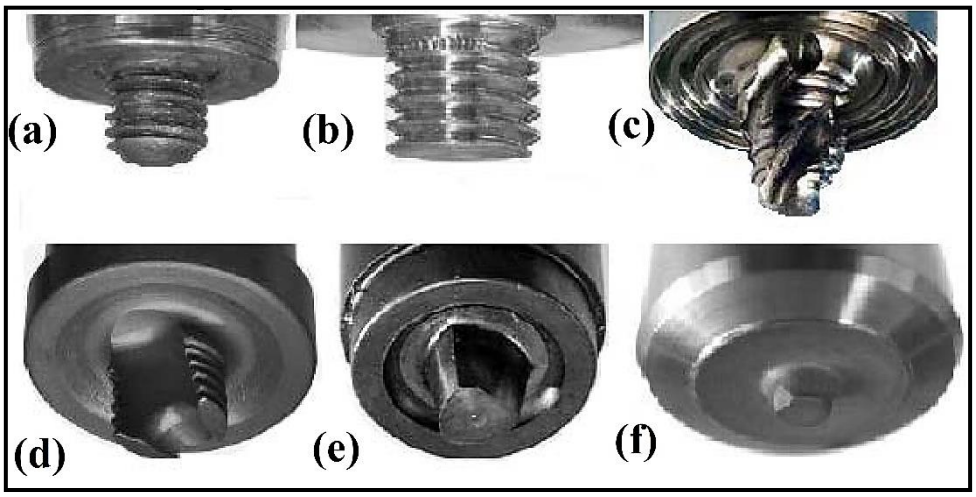

Fig. 1.6. Different pin geometries [10]
a. round-bottom, b. flat-bottom, c. MX triflute, d. A-skewTM, e. Trivex, f. threadless

1.3.5. Advantages, limitation and applications of friction stir welding

Friction stir welding has many advantages over fusion welding processes:

- Eco-friendly technique
- Energy efficient process
- Good mechanical properties can be obtained in the as-welded condition
- No consumables are required like electrodes and gas shield
- Similar and dissimilar joints can be easily done
- Welding preparation is minimal
- Reduces distortion in parent components
- Easily operated in all directions
- No toxic fumes are released
- Improved fatigue performance through elimination of stress concentrators
- Maintenance cost is very low

Limitations:

- Exit hole occurs when the tool is withdrawn after the process
- Heavy down forces are required for large welds
- Less flexible than fusion welding techniques

Applications:

- Next generation monolithic metallic wing,
- Shipbuilding and Offshore
    - Hulls
    - Freezer panels
    - Honeycomb panels
    - Helicopter landing platforms
- Automobile industries
    - Aluminum Engine Cradles
    - Suspension struts
- Aerospace and aeronautical industries
    - Wings
    - Panels
    - Empennages
    - Cryogenic fuel tanks
    - Monolithic metal wings
    - Metallic fuselages
- Sports industries
- Fabrication industries
- Rail industries
    - Railway goods wagons
    - Rolling stocks
    - Railway tankers
    - Trams
    - Underground carriages

1.4. Friction stir processing

Friction stir processing (FSP) is a new grain refining technique based on the concepts of friction state welding (FSW), that has found increased interest in the recent decades. FSP is based on the severe deformations in process of FSW that refines the structure of grains as well as secondary phase particles (SPP) of the material. The ultra-fine structures (UFG) formed by the process is desirable owing to its superior mechanical properties. Therefore, the creation of

the dynamic recrystallization zone (DXZ) is an essential aspect of this process. The processed region of the material undergoing FSP is locally exposed to higher temperatures thereby causing strong plastic deformation. Several studies have investigated the production of large volumes of UFG structures in a material by processing through multi-pass using FSP [16,17].

However, the advantage of FSP is to better modify the surface of components wherever required and this should be explored in depth. The technique also encompasses several variables and parameters in FSP and careful selection and optimization of parameters is required in order to achieve the desirable microstructures in the material.[18,19].

Advantages of FSP

- Microstructural refinements, homogeneity of grains and densification can be easily achieved by FSP
- Properties of processed material can be optimized and controlled accurately by FSP.
- The depth of the microstructural refinement of the material can be refined as per requirement by adjusting the tool dimensions (pin length).
- No external heat supply is required during the operation and the frictional heat generated by FSP is eco-friendly.
- The change of size and shape of the processed region during the FSP is negligible when compared with other conventional processes.

1.5. FSP vs. traditional techniques

Conventional methods (such as thermal spraying, laser cladding, plasma transferred arc) for fabricating surface composite materials involve melting of particles and injection of liquid phase into the composite layer. Due to cast microstructure of the composites, these processes can lead to the development of interfacial reaction layers at the matrix/particle interface. In these processes, there is considerable possibility of particle segregation which is due to differences in particle and melt densities. Fusion process involves high heat input and is prone to contamination. These processes produce a lot of energy and consume a lot of it.

In contrast, FSP is a solid-state process that is characterized by low heat inputs and can consume low energy. Due to grain refinement during FSP process, it provides better microstructural characteristics than traditional methods. Additionally, it offers wider operating range and selective processing. It reduces cost because of low energy consumption (utilizes

only 2.5 percent of the energy required for laser weld). As a result, FSP has become a viable option for fabrication of surface composites [20,21].

1.6. Composites

Composite material is defined as a combination of two or more materials or different phases of single material, with superior properties and illustrates better properties than any of the added component material. For fabrication of composite materials, the reinforcement particle size, amount and distribution in the matrix material plays an important role to obtain superior or limit the overall properties of the composite material.

In nanocomposites one of the phase/materials contain the size in the range of nanometre (1nm – 100 nm). There are several types of nanocomposites and these are distinguished as ceramic matrix nanocomposites (CMNC), metal matrix nanocomposites (MMNC) and polymer matrix nanocomposites (PMNC) [22,23].

1.6.1. Metal matrix nanocomposites (MMNC)

From the past two decades, the use of metal matrix nanocomposites in manufacturing industries is increased massively due to their superior properties and durability. Several fabrication techniques have been used to produce MMNCs. While manufacturing MMNCs it is not only important to get superior properties but also distribute uniformly the nano-reinforcement particles into the matrix and avoid un-interface bonding. Poor interface bonding and nonuniform distribution of reinforcement particles lead to deterioration of its properties and reduce the life of the component. A good combination of reinforcements and the metal matrix will improve two distinct properties like ductility and high strength. This combination of strength to weight ratio implies that , MMCs application will increase massively in manufacturing industries [24,25]. Aluminum metal matrix composites (AMMCs) are the best example for these kinds of MMCs. Around 40 years ago, AMMCs were being used in aerospace and defence sectors, especially for fabrication of space shuttle orbiter frame and rib truss members made of continuous boron fiber reinforced aluminum matrix material. Some other applications like landing gear drag link (for weight reduction) and high-gain antenna boom (Hubble Space Telescope) etc. An optimum combination of nano ceramic reinforcement and aluminum matrix composite material increases a wide range of applications in manufacturing industries [26].

1.6.2. Importance of metal matrix composites

Recently, aluminum alloys are very promising materials and have considerable applications in aerospace, automobile, military, ship and transportation industries because of their outstanding properties (low density, good resistance to corrosion, excellent thermal conductivity and high specific strength, etc.). 6XXX series aluminium alloys are very extensively used as alloys in industries. A versatile extruded alloy with medium to high strength, inexpensive and easy to machine capabilities, 6061 alloys has been an attractive material for industries. In the last two decades, the use of metal matrix composites (MMCs) in manufacturing industries has become essential for producing high strength and light weight components. The combination of ductility and toughness of MMCs is employed for a wide range of applications in smart industries [27,28].

Most of the aerospace, automobile and defense industries are developing a massive number of components by using Aluminum metal matrix composites (AMMCs). In addition, to improving the properties of AMMCs, nano reinforcement particles are incorporated into the matrix. Nano-reinforced AMMCs show extraordinary potential in all manufacturing industries. Al_2O_3 and SiC particles are mostly used as reinforcement for Al alloys and their products. To achieve superior properties is not only a major challenge, the distribution of reinforcement particle in an even manner is a difficult task obtained from conventional methods. Fabrication of MMCs can be done by applying various techniques. Producing MMCs by casting or liquid infiltration method leads to vigorous reaction between the reinforcement and the matrix material but simultaneously also leads to deterioration of properties of the MMCs because of poor wettability. Squeeze casting or pressure methods take a short time to fabricate the composites and, due to this, low reaction time between the molten metal and reinforcement lead to formation of conventional defects like shrinkage cavities and porosity [29].

Diffusion bonding is a solid-state technique for merging dissimilar or similar metals. In this process, the bonds form at a high temperature between in-contact metallic surfaces due to inter-diffusion of atoms. By this technique, the orientation and volume fraction of the fiber reinforcement cab be controlled easily but high processing temperature, pressure, and time make the technique expensive. This can be overcome by applying sinter-forging techniques to produce MMCs. The drawback of this technique is limited to producing smaller MMCs only. Since wear property is a surface deprivation property, the dispersion of reinforcement particles in the matrix and grain refinement is most important to obtain good surface properties of metal. It is very difficult to disperse reinforcement particles into the matrix using improper techniques

(conventional surface modification methods). Considering the above complications, Friction stir process (FSP) is best suited for preparation of surface composites and surface modifications. Friction stir processing (FSP), a recently developed surface modification technique, is found to provide a solution to the conventional surface processing issues and is related to differential fusion weld structures. Previously, a few researchers studied the effect of SiC on different grades of aluminum by using multiple passes of FSP. Many researchers worked on different reinforcements and combinations with multi-pass FSP [30–33].

1.7 Functionally graded materials

The result of scientific advances in materials science and the continuous developments in modern industry has led to continuous demand for advanced materials. This demand for advanced materials with specific properties has led to the gradual transformation of the materials from their basic (monolithic) states into composites. Recent advances in materials processing and engineering have resulted in the development of functionally-graded materials (FGMs). These are second-generation composite materials that have been designed to provide superior performance.

An FGM is a type of composite material that is classified by its graded structure. Specifically, FGM is usually composed of composite material whose property varies spatially and is intended to optimize the performance by distribution property. It might be a gradual variation in structure, texturization level, grain size, chemical characteristics and physical characteristics layer by layer [34,35]. The gradation property in FGMs enables the reduction of thermal stress, stress concentration and residual stress found in conventional composites. The gradient material properties allow the designer to customize material responses to meet the design criteria. FGMs resolve practical issues that arise from the fabrication and application of composite materials. FGMs are used in nuclear, aerospace, optoelectronics, orthopaedics, bioengineering, defense etc. These materials have high efficiency and multi-functional role in the latest generation of spacecrafts [36,37].

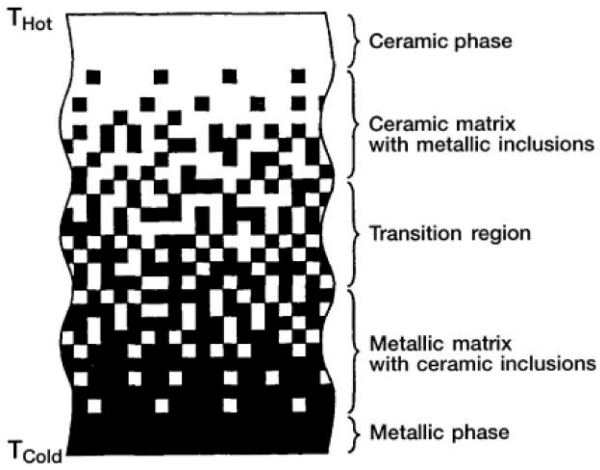

Fig. 1.7. Continuously graded structure [38]

For example, when the space shuttle returns to the earth's atmosphere, ceramic tiles are employed to prevent heat from being produced. But, to the difference in coefficient of thermal expansion, these tiles are likely to crack at the interface. In this case, conventional homogenous materials are ineffective. To resolve such limitation of conventional materials under severe conditions researchers from Japan in 1984 suggested the idea of FGM. As a result, the heat resistance and load-bearing capacity of the compositional gradient made of ceramic and metal eliminated the problem of cracked tiles on the space shuttle [39]. Figure 1.7 depicts the progressive transition of the microstructure towards temperature gradient.

There are different processing techniques available to fabricate FGMs, and these include liquid, solid and gas-based approaches such as chemical vapor deposition (CVD) [40], thermal spraying [41], centrifugal casting [42], gel-casting [43], powder metallurgy (PM) [44], spark plasma sintering (SPS) [45], layered manufacturing (LM) [46], friction stir processing (FSP)[47] etc. Among the processing techniques, the CVD method utilizes heat, light or plasma as a source of energy and primarily aims to produce a thin graded film. The gas ratio, flux rates, type of gas employed and deposition temperature should be carefully regulated to achieve a gradient chemical composition in FGM. However, CVD method has several drawbacks such as being energy-intensive and often produces toxic gases as by-products [48].

Another widely used method for gradient FGM is the centrifugal casting wherein the compositional gradient is formed due to density differences between metal matrix and reinforcement material. It is based on the phenomena of natural transport. As a result of centrifugation, the higher-density particles transfer to the outer region and lower density particles migrate to inner region. The FGM manufacturing methods based on centrifugal force are classified into three categories, namely, centrifugal slurry, centrifugal method, and

centrifugal pressure method. In the centrifugal method, a homogeneous mixture of molten metal with ceramic or intermetallic particles is exposed to centrifugal force in order to attain the desired gradation. The difference in the centrifugal force caused due to the variation in density of the solid and molten metal results in the formation of composition gradient. In centrifugal slurry method, the slurry is exposed to the centrifugal force and it involves two types of solid particles i.e., high-velocity particles and low-velocity particles. The liquid portion of the slurry is extracted after full sedimentation, and it is no longer part of FGM. Moreover, the centrifugal pressurization process employs only centrifugal force to create nominal pressure. In this method, compositional gradient must be formed before the centrifugal force is applied. Although the centrifugal method may produce continuous gradients, this method is restricted to radial gradient FGMs [49].

On the other hand, the PM method is known as a cost-effective method to fabricate bulk FGM. The method involves powder production, mixing, stacking, pressing and sintering. FGMs produced by PM have a layered structure that does not achieve a continuous composition gradient. But, FGMs produced using PM always contain a finite quantity of pores that degrade mechanical, physical, corrosion and wear properties [50].

Solid freeform fabrication (SFF), commonly referred to as 3D printing, produces complex gradient components by using computer aided design (CAD) data. This process falls into the category of controlled blending. It is also known as additive manufacturing (AM) or rapid prototyping (RP). The unique feature of SFF is its ability to directly manufacture FGMs. It requires less tooling, shorter lead time and less wastage of materials. This method has an ability to optimize the properties and control the composition of built part. It does not necessitate the use of fixturing, tooling and other peripheral activities that are commonly associated with traditional processes. It offers numerous benefits such as increased production rate, better energy-efficiency, optimum use of materials, production of complex shaped components and freedom of design without constraints because the components are directly manufactured from CAD data. The SFF techniques developed for the production of 3D components are not suitable for conventional composite materials. The mass production of such components by economic means requires a rapid alternative. SFF also entails some challenges in terms of physical properties, dimensional accuracy and poor surface texture which requires post-processing operation [51].

The energy used during previous manufacturing processes is lost while the material is melting. This potential issue can be solved through the use of a surface adaptation process and

composite fabrication process that can be performed at temperatures below the melting point of base matrix.

Recently, FSP has been proven to be effective and versatile for producing surface composites and localized functional gradient on a micro-scale [52]. This is carried out under the same conditions as Friction stir welding (FSW). The theory and concept behind the two processes (FSP and FSW) is the same, but the goals are different. FSW is a joining process whereas, FSP is a surface modification process employed for microstructural refinement of workpiece material [53]. FSP has also been widely used to create surface metal matrix composites (MMC) where severe plastic deformation is caused by enforcing a non-consumable stirring tool on the workpiece surface. The FSP method is mainly controlled by the rotational and traveling speed of the tool. The major benefits of FSP, that sets it apart from other methods are precise control, microstructural refinement, no porosity, and superior metallurgical properties in the processed area. In addition, FSP is environmentally friendly, energy efficient and has low distortion of shape and size of the workpiece. It can also be used for the production of polymer composites. They play a vital role in the field of energy materials like fusion reactor that involve joining and processing of vanadium alloys. FSP can also be used to fabricate FGM wherein the reinforcement particles are packed in a groove in which the stirring process is performed [54].

1.8. Definition of the problem

The present work seeks to address the problem of incorporating reinforcement particles in the base matrix to create a microstructural gradient along the depth. The authors of this work attempted to develop a novel method of tailor-made functionally graded Al/SiC composite by placing SiC particles in pre-prepared square-shaped grooves and systematically evaluate its microstructural characteristics, mechanical properties (mainly wear behavior and microhardness) and correlate them with pass number.

Though FSP is widely used, the following problems are encountered while fabricating an FGM using a conventional tool (i) It is not possible to achieve uniform distribution of particles after one pass of FSP. (ii)There is particle agglomeration either on the retreating sides (RS) or on the advancing side (AS) although this can be reduced by multi-pass FSP. (iii) It will be difficult to predict the actual percentage volume of reinforcement particles distributed in the matrix. To overcome the shortcoming of a conventional tool, the authors attempted to create an Al/SiC compositional gradient with a newly designed hybrid tool over a predefined length

as per the developed process model. In this study, a novel HYB tool was designed and compared with CON tool to develop Al/SiC gradient composite. The effect of conventional and hybrid tools on the mechanical properties of the FG sample was then compared and it was concluded that FSP with hybrid tool improved the properties of Al/SiC FGM, effectively.

1.9. Research gaps identified from literature review

- Limited work has been reported on the fabrication of graded composites with varying tool depths.
- Detailed analysis of optimization of the number of passes is a challenging issue to improve the distribution of particles in graded composites.
- Most researchers have focused their attention on the conventional tool design and not enough work has been carried out on the hybrid tool design of the tool pin.
- There is insufficient research for coming up with a mathematical model of 1-dimensional graded material with a linear change in composition.
- The comparison of mechanical properties concerning the conventional and hybrid tools has not been adequately done in research.

1.10. Objectives of the study

The current work deals with a novel method for generationg tailor-made functionally graded Al/SiC composite and systematically evaluates microstructural characteristics, mechanical properties and correlates them with pass number and tool profile. The entire work is divided into five main objectives.

1. To create microstructural gradient along the depth by varying tool pin and reinforcement volume percentage using FSP.
2. To analyze the effect of multi-pass on the FG samples developed for improving mechanical properties.
3. To develop an FGM using a mathematical model and characterize the processed FG samples.
4. To analyze the effect of conventional and hybrid tools on the characterization of functionally graded samples
5. To study the effect of pin profiles on corrosion properties of developed FGM samples.

1.11. Organization of thesis

The present thesis is arranged in the following sections.

CHAPTER-1

This chapter describes the current state of the art techniques, discusses the fundamental definitions and establishes a theoretical framework for the further interpretation of the results. This section consists of two main sections: Friction stir processing - where the basic concepts and physical principles of the process are detailed along with process parameters and some of the most important investigations concerning property enhancement via conventional FSP; Functionally graded materials - describing this class of materials, its conventional production methods and fabrication of composites through FSP.

CHAPTER-2

An up-to-date comprehensive review of research about the development of composites and methods of utilizing SiC in aluminium alloys is provided. The various issues related to reinforcement strategies and tool design are also discussed in this chapter. The research gaps observed after reviewing the articles are also given in this chapter.

CHAPTER-3

This chapter supplies the necessary information on experimental setup and methods that were followed to fabricate the graded structure. A brief description of the base material and reinforcements have been also included. Furthermore, the optimization of process parameters, tool design, pretesting of the samples and formulation of a mathematical model to create compositional gradient are listed. Finally, the techniques and procedures employed to characterize the graded surface are discussed.

CHAPTER-4

This chapter reports the preliminary results that were obtained in the optimization of process parameters. This section is divided into three main areas, concerning the characterization of base material, reinforcement particles, and SiC reinforced graded composites. It also discusses the experimental results obtained for Al/SiC graded samples processed with different pin

lengths and with a newly designed hybrid tool as per the developed process model. The experimental results of graded samples processed with different pin lengths are correlated with pass numbers. The graded samples produced by the novel-designed hybrid tool were compared with the conventional tool with respect to the mathematical models. Results obtained by metallography, SEM/EDS, EBSD, microhardness, tensile test, corrosion and wear analysis are presented and analyzed.

CHAPTER-5

The chapter reports the conclusions drawn from each objective and the summary explaining the work overall. The conclusions of the investigation to evaluate the varying tool pin lengths and mathematical model as an alternative method for fabrication of Al/SiC graded structure are provided. It also mentions the important findings of the research and the scope of research in future.

Chapter-2

Literature survey

2.1. Introduction

Aluminum alloys are extensively used in ship building, automobile, structural and aircraft applications. 6082-T6 Al alloy, in particular, is the most frequently chosen material for medium strength applications due to its malleability and weldability.

Metal matrix composites (MMCs) have superior mechanical properties when compared to unreinforced metals. Poor wear resistance of MMCs' limits its application in manufacturing industries. To make up for such drawbacks, reinforcement is essential, where hard ceramic particles are incorporated in soft aluminium matrix that enhance Young's modulus, yield strength and wear resistance. Young's modulus is the measure of stiffness or rigidity of a material. The Young's modulus is also referred to as the modulus of elasticity. It depends only slightly on the microstructure morphology of materials. A decrease in the values of elastic modulus is usually ascribed to the substantially increased volumetric share of grain boundaries. One of the reasons for a decrease in the Young's modulus is considered to be the elastic deformation of the grain boundaries. Several geometric models have been proposed, designed for assessing the volumetric share of atoms located within the region of grain boundaries as a function of the average grain diameter. The volumetric share of the grain boundaries can be calculated from the Palumbo relationship.

$$f_G = 1 - \left(\frac{d-\Delta}{d}\right)^3 \qquad (1)$$

Where f_G is the volumetric share of the grain boundaries, d is the grain diameter, and Δ is the thickness of the grain boundary.[55]. Sharma et.al used digital image correlation (DIC) technique to measure the Young's Modulus of graded structure produced by FSP. They reported that Young's Modulus values decreased every 2mm from the maximum composition side [56]. Hsu et.al used a mixture of Al-Ti powders to fabricate Al-Al_3Ti composites using in-situ FSP. They reported that Youngs modulus of composite increased 63% higher than the base metal due to fine microstructure and increase in volume fraction [57]. One of the major problems faced by the widespread use of MMCs in industry is cost-to-strength ratio. In these circumstances, surface metal matrix composites (SMMCs) are best suited. Conventional techniques such as casting, powder metallurgy leads to defect formation (like porosity, blow holes etc.). These shortcomings require a composite manufacturing and surface property modification process that can be carried out at temperatures below the melting points of the base matrix.

2.2. Friction stir welding (FSW)

Thomas et al. invented and patented friction stir welding (FSW) in 1991 and conducted initial experiments on aluminum and its alloys at The Welding Institute (TWI) of UK [3]. FSW is an incessant hot shear process, in which the rotating tool (harder tool material) is plunged in the abutting faces of the joint (soft base material). The relative motion between the substrate and the rotating tool generates heat (frictional heat) that plasticizes the material around the tool. The plasticized material moves forward with respect to the tool traverse direction and joins the base material. FSW can be applied to join similar, dissimilar, ferrous and non-ferrous materials and is suitable for aerospace, automobile, marine, rail and transportation industries [4]. FSW is a novel process to join aluminum alloy extrusions in solid state with efficient welding quality. Early periods PJ. Haagensen et al.[58] performed fatigue test on butt welded AA-6082 aluminum alloy by FSW and compared the results with MIG. The results showed that the welds formed with FSW had 50% higher fatigue strength than welds fabricated with MIG. G. Liu et al.[59] studied the microstructural and hardness properties of 6061-T6 aluminum alloy welds produced with FSW. The welded samples were characterized using light metallography and transition electron microscopy. From the microstructural and hardness analysis, it was revealed that the grain size at the stir zone (SZ) was reduced to 10 um and hardness was reduced to 65 HV. Rhodes et al. [60] studied the effect of FSW on microstructural properties of 7075 aluminum alloy. The size of the nugget zone (NZ) decreased to 2-4 µm due to the recrystallization in NZ and the dislocation density was lower than that of the parent/base metal.

Correlation of process parameters of FSW with modelling and experimentation was first done by Jata et al.[61] In dynamically recrystallized region (DXR), the grain size reduced to 9 µm and misorientation of grains (15^0 to 35^0) was observed by using orientation image microscopy. From the results, it was observed that the basic reason for recrystallization in DRX was continuous dynamic recrystallization mechanism. The effect of tool wear during FSW was investigated by Prado et al.[62] From the results, it was concluded that, tool rotational speed had significant effect on tool wear (with increase in tool rotational speed increases the tool wear). Pao et al.[63] studied the fatigue behavior of friction stir welded aluminum alloy under air and NaCl solution. The fatigue crack growth of FSWed samples was higher in 3.5% NaCl when compared with air medium.

2.3. Friction stir processing (FSP)

Since FSP is a relatively a new process, the researchers not only investigated the possible aluminum alloys that can be processed but also investigated the effects of process parameters on various mechanical and microstructural properties. This process can be easily adopted as a processing technique to produce finer grains. Extensive studies are being conducted in FSP to make it cost-effective in aerospace and automotive industries. Many researchers have dealt with the microstructural investigation of various friction stir welded and processed aluminum alloys [64–67].

They essentially examined grain refinement in the processed and heat affected zones. It was observed that the FSP of the commercial Al alloys of different grades (1100, 2024, 5083, 6082, 7075 and 7475) resulted in a significant improvement in superplastic properties. Various material properties such as tensile strength, micro-texture, fatigue and hardness were also examined for different aluminum alloys [68–72]. Efforts have also been made to study the influence of various process parameters such as rotational and traveling speeds on the properties and microstructure developed during the FSP. The heat and residual stresses generated during the process were investigated experimentally and modelled numerically using finite element analysis (FE). In 2001 researchers attempted to produce ultra-fine grained (UFG) microstructure via. FSW. From the results, it was observed that, FSW method is one of the most effective techniques to produce UFG microstructure with improved mechanical properties.

Douglas et al.[73] worked on Submerged friction stir processing (SFSP) to produce bulk ultra-fined grain structure. The experiments were carried out underwater using multi-pass FSP and it was observed from the results that the grain size was significantly reduced to 200 nm. Chuang et al.[67] utilized FSP technique to fabricate bulk multi-element Mg base alloys by varying parts of AZ31 sheets, Al and Zn foils under liquid nitrogen cooling conditions. Multi pass technique was implemented to obtain finer microstructure with enhanced hardness. The fabricated multi-element Mg based alloy exhibited superior hardness of 400 HV in the processed region due to grain refinement and intermetallic phase formation occurred under liquid nitrogen cooling conditions. Jian-Qing Su et al.[68] studied the effects of cooling media (water, methanol & dry ice) and multiple overlapping passes to create bulk UFG structure on aluminum alloys by FSP. The microstructural analysis revealed that the grain size reduced to an average of ~250 nm using multiple overlapping techniques with rapid cooling effect. This process led to non-uniform UFG in the processed region.

Mishra et al.[70] studied the nature of low temperature superplasticity of cast alloy to produce UFG microstructures by FSP. At low temperatures and high strain rates, the material exhibited superplasticity and produced UFG at the stir zone. From the results it was observed that FSP is a solid-state process that reduces porosity with a fine grain structure. During FSP, when the processed region reaches a temperature above 390°C, the material undergoes severe superplasticity and causes microstructural heterogeneity in the stir zone. Mishra et al.[74] investigated the formation of UFG microstructure at low temperature (0.48 T_m) using FSP. At 175°C, a maximum superplasticity of 240% with UFG structure (avg. grain size of 0.7 um) was achieved. Zhao et al. investigated effect of pin profile using columnar and tapered pins- both with and without threads and observed that the tapered pin profile with screw threads produced welds with the minimum defects in aluminium alloy[75]. Mahmoud et al. studied the friction stir processing of SiC reinforced aluminium composite using four tool shapes – circular with/without thread, triangular and square. The square probe resulted in more homogenous distribution of SiC particles than other profiles[76].

2.4. Microstructure

Typical cross section of an FSW/P joint has three different zones: 1) heat affected zone (HAZ), 2) nugget or stir zone and 3) thermo-mechanically affected zone (TMAZ) which is the region between HAZ and nugget, Figure. The stir zone is the central region of the weld where dynamic recrystallization occurs as a result of high temperature and severe plastic deformation, leading to the formation of fine equiaxed grains, Fig.2.1. In FSW/FSP, tool geometry, composition and temperature of the work piece material, vertical pressure, cooling rate and process parameters significantly influence grain size in the nugget zone [77].

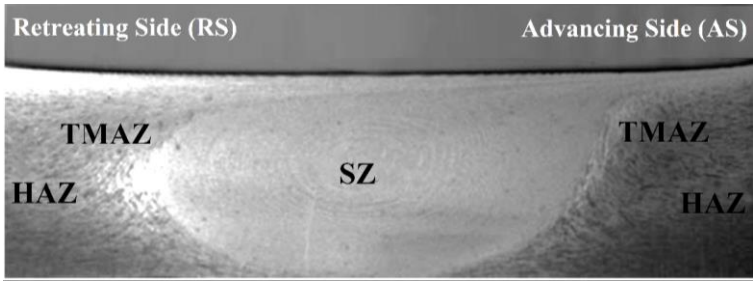

Fig. 2.1. Macrographs of various zones in FSP[10]

Microstructures of the material in this region usually contain a banded structure called "onion rings", (refer Fig. 2.1). The spacing between these bands equals the distance the tool moves forward during each single rotation [78,79]. The variation in the microstructure is

attributed to: 1) grain size, 2) particles or precipitates distribution [80], 3) crystallographic texture [81], 4) dislocation density [82], and 5) intermixing pattern within weld joint [83]. Krishnan et al.[79] demonstrated that these variations occur when the material gets heated by friction and the advancement of the tool extrudes the material around to the retreating side resulting in formation of the bands. In TMAZ, grains are heated and plastically deformed but not completely recrystallized; therefore, they are not as fine and equiaxed as stir zone grains. Finally, HAZ is only affected by temperature and not by mechanical work. Therefore, the main change in HAZ microstructure is coarse grain structure or precipitates [84].

2.5. Material flow in FSW/FSP

The formation of a defect free weld depends on material flow during FSW. On the other hand, in FSP, the material flow determines the development of microstructural features and in the special case of composite fabrication the material flow in the stir zone determines the particle distribution. Thus, in the recent years there have been various techniques to study the material flow such as tracking of tracer particles post welding by microscopy [85,86], microstructural analysis of dissimilar alloy joints, in-situ observation using X-ray transmission systems [87], simulation by numerical modeling [88–90], and using analog materials like colored plasticine [91]. However, this aspect is still not fully understood and has been the subject of numerous articles [92]. The deformed material during FSW/FSP has three types of flow transport: 1) intense plastic deformation of tool and friction between the tool and work piece material 2) a downward flow of material in the region close to the tool caused by the use of threaded pin. This results in upward motion at the outer periphery of the mixing region of the stir zone; and 3) material flow along the welding direction due to the movement of the rotating tool. According to the study, it is indicated that majority of the material flow induced by these three types occurs on the retreating side (refer Fig. 2.2) [77].

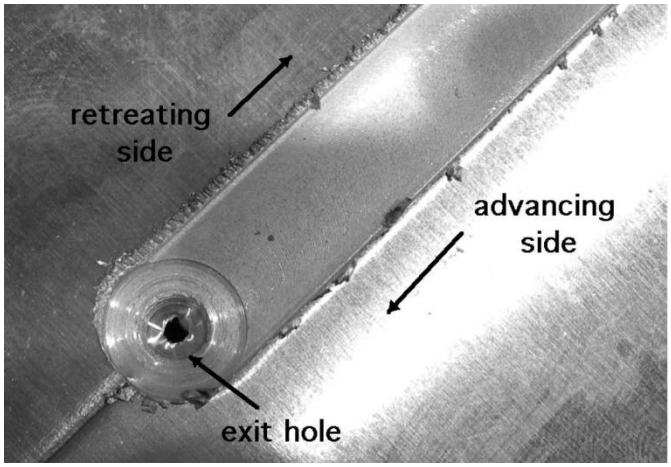

Fig. 2.2. Surface of processing line in FSW[93]

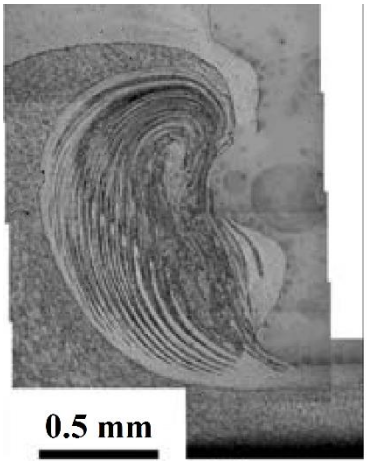

Fig. 2.3. Intermixed region of SZ[94]

When considering FSP for fabrication of composites, this mixing must be taken into account to control the distribution of material. First, the stirring action around the tool pin generates a zone of rotation and mixing. The thickness of the processed zone depends on the material properties, welding parameters and the rate of heat transfer to the tool. Second, as previously stated, the use of threaded pin induces mixing which aids in particle distribution both in vertical and longitudinal directions during composite fabrication by FSP. In general, the amount of mixing increases at higher rotation speeds or lower travel speeds [82]. Su et al.[94] demonstrated that intermixing occurs during friction stir welding of dissimilar Al alloys using a threaded tool (refer Fig.2.3). The threaded tool facilitates vertical plunging action along with additional frictional heating causing flow of the material. This process occurs during each single rotation of the tool and forms intermingled lamella. It is then discharged from the bottom of the threads and travels both outward and upwards following a helical vertical rotational flow. Gerlich et al.[95] have shown that the width of this intermixed region increases with the dwell time in friction stir spot welding, which implies larger intermixed regions may be achieved in friction stir seam welding by decreasing the travel speed.

2.6. Classes of surface composites

FSP was investigated for surface modification and there are various reinforcement methods described in the literature. In this process, metal alloys are reinforced with ceramic particulates, mainly carbide powder (SiC, TiC or WC) in order to increase strength, hardness, and resistance to wear without affecting the inherent material properties. The creation of SMMCs can also be achieved through the use of high energy laser melting techniques [96,97].

In these techniques, the ceramic phases are coated on the surface of the material, either by pre-depositing or injecting simultaneously with the laser beam. During processing, the powder coating is melted together with the surface layer of the substrate, which allows the ceramic particles to mix into the melted material. Unfortunately, the resulting resolidification of the localized melt pool is difficult to control, so the developed microstructure often leads to poor mechanical properties. In comparison, it was found that FSP can be used to create a metal-matrix surface composite with uniformly distributed SiC particles free of defects.

The process also assists particle break up, and produces a fine dispersion of particles within the microstructure, which can double the microhardness of the base material; e.g., from 85 HV to 173 HV, when a 27 vol% of SiC particles was processed into the surface layer. The depth of the composite layer generally varies from 50 μm to 200 μm and the thickness of composite layer depends on the amount of ceramic particulates pre-placed on the surface of the alloy[96]. However, there are several limitations on the processing parameters. First of all, it was found that the transverse speed of 75 mm / min has an influence on the bonding between the surface composite layer and the material substrate. It was observed that with increase in transverse speed, the bonding strength of the composite layer deteriorates and becomes detached from the substrate. On the other hand, the depth of the plunge should be controlled, to prevent pre-placed SiC particles being driven away from the tool. However, it was found that very low plunge depth values lead to ineffective mixing of SiC particles in the alloy.

Shafiei-Zarghani et al.[98] recently attempted to incorporate nano-sized Al_2O_3 into the surface layer of 6082 Al alloy. After a single FSP pass, the Al grains were refined down to ~ 4.8 um. However, although the nanoparticles were embedded in the Al matrix, they tended to be agglomerated and distributed in the form of clusters. The dispersion of the nano-sized Al_2O_3 particles was improved by multi-pass processing. The grain size was also further reduced to ~ 0.7 um after 4-FSP passes, because of homogenous distribution of Al_2O_3 particles grain growth hindered by the pinning action of the intermetallic particle. As a result, the hardness and wear resistance of the surface composite layer increased threefold compared to the base material.

Research has also shown the potential of using FSP as a bulk processing technique for thicker alloy plates. Microstructure refinement with a larger volume of material volume and depth can be achieved by using friction stir tools with a larger pin size. This is particularly efficient in the production of superplastic materials. Superplasticity is defined as the ability of a solid crystalline material to deform and elongate beyond 200 % of its original length during tensile deformation.

Materials that exhibit this behavior can be easily formed into complex objects. Many aerospace components made of aluminum and titanium alloys are superplastically formed [99]. There are two basic requirements for a crystalline material to exhibit superplasticity. 1) The microstructure must consist of a fine grain structure, (typically < 20 μm grain size). 2) Finely distributed, thermally stable particles must be present in the material in order to pin the grain boundaries and to stabilize the fine-grain structure during the forming. As a result of these requirements, FSP appears to be a promising processing method.

The potential of generating superplasticity via FSP has been investigated with different Al alloys [99,100]. The results of the one-pass processing showed an increase in the uniform elongation of alloys which initially did not exhibit superplasticity at low temperatures (< 0.5 T_m). However, the superplasticity depends on the size of the grains and the stability of the refined microstructure, temperature and strain rate for which maximum elongation could be achieved with different processing parameters and alloys. Liu et al. showed that a 7075 Al alloy processed by FSP can be water-cooled to achieve a UFG structure with an average grain size of 0.8 μm and a maximum ductility of 540 % at 350 ° C [101]. In combination with the optimized conditions, some of the processed alloys were able to deform over 1000%. Numerous studies have been conducted to produce refined larger volume of microstructure using multi-pass processing. These reports provided promising insights in producing homogeneous microstructures with fine grain size [100].

The superplasticity was obtained after multiple pass processing and it was found that the ductility of the alloy was reduced from that of a single pass process. The use of FSP as a property optimization technique has shown its potential in several other metallic alloys as well [93–95] and, in particular, FSP of magnesium alloys is increasingly being investigated. The formability of Mg is poor due to the lack of active slip systems within its hexagonal close packing (HCP) crystallographic structure. Recent researches have shown that the formability of Mg can be improved by refining the grains of the alloy to less than 20 μm [105]. As in the case of superplasticity, this improvement in ductility could be the result of an increase in the activity of non-slip systems and grain boundary sliding that occur in the material with refined microstructure. It was observed that Mg alloys with grain sizes of up to ~3μm exhibit fracture limits similar to those of pure Al. The results showed that the microstructure produced from processing parameters that induced lower peak temperature during processing was finer than the microstructure created from a higher temperature process or from the base material. This suggests that the refined microstructure of Mg alloys after FSP was unstable and sensitive to temperature.

However, the effect of multi-pass processing on the grain size was noted to be negligible. Therefore, it was assumed that the refined microstructure could be maintained until maximum temperature was reached during processing. This is because the peak temperature (77 ºC) decreases with increase in distance from the processed zone. As a result, during multi-pass processing, the temperature exposed to the original processed region will never be higher than that of the previous pass. This phenomenon can also be observed with Al alloys that do not have thermally stable particles in the alloy to stabilize the refined microstructure [105].

FSP can also be used to refine the microstructure of cast Mg alloys. Ma et al. showed that the coarse network-like eutectic β-Mg17A112 phase within A291 Mg alloy, which is otherwise detrimental to the mechanical properties, can be broken up and solutionised during FSP [106]. By refining the microstructure of the cast material and through subsequent post-aging, the yield strength and tensile strength of the alloy were increased from 73 MPa and 111 MPa to 177 MPa and 337 MPa, respectively [107]. The potential of using FSP to improve the mechanical properties of Ni-Al bronze alloys was also explored [108,109]. This material is widely used in marine applications due to its good combination of corrosion resistance, strength, fracture toughness and spark-free behavior [110]. Ni-Al bronze components with thick cross sections are usually cast, and low cooling rates often result in the formation of coarse microstructure, which reduces physical and mechanical properties. However, FSP is capable of achieving localized surface strengthening. Oh-ishi and McNelly extensively investigated FSP of an Ni-Al bronze alloy, with composition Cu-9A1-5Ni-4Fe (wt %).

Mahmouda et al.[111] studied the effect of Al_2O_3 and SiC micro reinforcement particles in Al alloy by FSP. By varying the volume ratios (20/80, 50/50 & 80/20) of Al_2O_3 and SiC in the aluminum alloy, increase in wear resistance and hardness was achieved. However, the combination of 20% Al_2O_3 + 80% SiC exhibited superior wear resistance than other combinations of SiC and Al_2O_3. Some of the researchers studied the effects of multi walled carbon nano tubes (MWCNT) introduced into the aluminum. Multi-pass FSP was used for an even distribution of MWCNT in the matrix material. The microhardness value was observed to be double that of the base alloy due to good dispersion of MWCNT in the matrix. Several studies were done on the effect of different reinforcement particles on microstructural, mechanical and wear properties of metal matrix composites. For example, Cr_2O_3 reinforcement powder was added to the Al alloy, SiC particles into Copper matrix, Gr/Cu and Al/TiC etc.

Several investigations have been done on the fabrication of SCs through FSP by using reinforcement strategies such as sandwich technique, hole filling technique, groove technique etc. Mertens et al.[112] incorporated carbon into the magnesium matrix by sandwich technique

and established its significance in grain refining via the pinning effect. They concluded that the addition of the reinforcement material and the reduction in grain size resulted in a 15% to 25% increase in yield strength. Madhusudan Reddy et al.[113] modified the surface of Mg alloy by filling the holes with SiC and B_4C powder and reported that the performance of surface composites using B_4C particles was found to be superior when compared to SiC particles. Srivastava et al.[114] produced aluminium-based surface composites by embedding Si_3N_4 particles using friction stir processing (FSP). They concluded that maximum hardness and tensile strength values were 125 HRB and 576 MPa respectively, for a single pass processed composite. However, an increase in pass number results in maximum wear loss and thermal expansion (for third pass). The effects of different process parameters such as multi-pass FSP, traveling speed, rotational speed, etc. on SCs properties were explored. But, the influence of various reinforcement approaches was not discussed. The method of incorporating reinforcement particles in the metal matrix plays a significant role in dispersion of reinforcing particles in width and depth direction of the reinforcement layer which affects the properties of the surface gradient [115].

Hangai et al.[116] utilized FSP for manufacturing functionally graded aluminum (FG/Al) foams with varying pore structures and concluded that Mg composition gradually changed in the bonding region. Gandra et al.[117] developed aluminum-based functionally graded MMC by incorporating ceramic particles with different median sizes in the surface layer of aluminum and showed that sufficient particle dispersion takes place when the particles are compacted in a groove located under the probe. Mishra et al.[96] used a novel method of surface modification process to create a surface composite (Al/SiC) through FSP. They reported that particles reinforced with 27 vol.% of SiC particles exhibit a hardness of around HV 173 which is almost double the hardness of parent alloy (5083-Al). Miranda et al.[115] adopted the FSP technique by employing a consumable tool with prefilled ceramic particles to produce Al-based FGM. The investigation proved that FSP with a consumable tool approach leads to the formation of a thin composite layer with low time consumption and tool wear. Moradi Faradonbeh et al.[118] performed a study on friction stir welding (FSW) of Al−B_4C composite with 4 different pin geometries and established that FSW parameters have a significant effect on the fragmentation and distribution of reinforcing particles in the weld center. Paidar et al.[119] conducted FSW to AA5182 by employing tungsten carbide (WC) as a reinforcement particle and concluded that mechanical properties (hardness and tensile) and wear resistance increased due to the addition of WC particles, causing substantial grain growth in the nugget zone.

Pol et al.[120] developed an effective technique for improving ballistic resistance by incorporating particles of TiB_2 and B_4C in different mass fractions into the surface of AA7005 using FSP. They concluded that the enhancement of ballistic resistance is ascribed to the availability of hard reinforcing particles in the surface composite and matrix tough core. Sharma et al.[121] fabricated Al−B_4C mono and Al−(B_4C+MoS_2) surface hybrid composites in AA6061 with the help of multi-pass FSP and reported that mono surface composite enhanced the hardness where the hybrid surface composite exhibited enhanced wear resistance. Paidar et al.[122] produced composite via FSP with a 10-cycle accumulative roll bonding. The researchers observed that by increasing the number of passes (1−8) the homogeneity of B_4C in the Al matrix improved the microstructure, mechanical properties, wear and fracture behavior. Gangil et al.[123] investigated the FSW of hybrid composites produced by FSP on Al−Zn−Mg−Cu alloy (AA7050-T7451). The findings indicated that when compared to composites prepared by FSP, composites welded by FSW showed an increase in microhardness because of better and homogeneous reinforcement particle distribution.

Jain et al. [124] investigated the effect of multi-pass FSP on the mechanical and micro-structural properties of AA1050/TiO_2 surface composite. The results revealed that surface composites processed by the second pass exhibit better wear resistance and hardness caused by acceptable distribution of particles when compared with as-received aluminum. Singh et al.[125] applied FSP to produce FGM with a combination of different matrix materials which are 6063-Al and 8011-Al alloys reinforced with Al_2O_3 and rice husk ash (RHA). The results revealed that tensile strength of hybrid functionally graded material composite increased till it touched 29.54% vis-a-vis 6063-Al alloy as base material and 42.5% in the case of 8011-Al alloy. The surface hardness of the FGM composite was enhanced by 72.5% and 97.11% with regard to base material 6063-Al and 8011-Al alloy, respectively. Barati et al.[126] used two surface processing methods, i.e., FSP and modified friction stir vibration-assisted processing (FSVP) to fabricate surface composite of Al6061/SiO_2. The mechanical, corrosive and wear properties of surface composite prepared by FSVP were superior to those prepared by FSP due to the formation of small grains and more homogenous distribution of the strengthening particles as vibration was applied. The use of a dome-shaped pin with different weight fraction of SiC within grooves of varying width was also studied using FSP to manufacture FGMs. The results suggested that an optimized FGM, with maximum wear resistance and tensile strength, was obtained for a composite which contained 10 wt% of SiC. Also, the tensile strength and wear resistance were reduced for the composite which contained 13 wt% SiC [127]. This was due to the clustering of reinforcement particles with a high mass fraction of SiC.

2.7. Chapter Summary

FSP is a promising metalworking technique with interesting capabilities, as it enables local customization of mechanical properties through microstructural modification. Although several authors have demonstrated that it is possible to produce metal matrix composites through FSP, there has been no documented evidence of a continuous or gradual distribution of composition or mechanical properties with varying tool pin and hole distance.

FGMs are new advanced materials that are highly attractive for a wide range of engineering applications because they allow different functional services to be designed within a part. Although this concept is in the early stages of development, it has attracted the interest of scientific community, leading to various investigations and technological applications. However, the technologies used to produce FGMs are very expensive and labour intensive, restricting the use of these materials to highly selective engineering applications.

Chapter-3

Experimental Methods and Characterization Techniques

3.1. Introduction

This chapter discusses the experimental setup and equipment used in the present research work. The details of the equipment along with the specifications used for the preparation, microstructural characterization, and estimation of mechanical properties are presented. The chapter explains the experimental setup for the fabrication of functionally graded (FG) samples using friction stir processing (FSP). The details of various devices, equipment, and methodologies used to evaluate various characteristics are also supplied. The process parameters are selected based on the previous literature while trial experiments were conducted to identify the ranges to conduct the experiments. The experiments were well planned and conducted to observe the characteristics such as particle distribution, grain size, microhardness, etc. Tools with different pin lengths and newly designed hybrid tool over a predefined length as per the developed process model. was used to form the compositional gradient (Al/SiC) structure.

3.2. Selection of workpiece and tool materials

6082-Al alloy rolled plates of 200 mm length, 146 mm width and 6mm in thickness were employed as base material (matrix) for this study**.** Due to space limitations in the backing plate, the width of plate was fixed as 146 mm and thickness of the plate was decided based on the tool pin length. The chemical composition of the alloy is shown in Table 3.1 and physical properties are mentioned in Table 3.2. 6082-Al has specific strength which enables the preferred grade alloy for structural applications, particularly in aircraft interiors. Despite different applications in engineering and exceptional properties, 6082-Al alloy has low wear resistance, low stiffness and low yield strength. To make up for such drawbacks, reinforcement is essential, where in hard ceramic particles are incorporated in soft aluminium matrix that enhance Young's modulus, yield strength and wear resistance.

Silicon carbide (SiC_p) with an average particle size of 27.5 µm was used as reinforcement particle. The SEM micrographs of SiC particles are shown in Fig.3.1. Silicon carbide (SiC) ranks as one of the most widely used reinforcements in aluminium metal matrix composites (AMMCs). It has low density and melting temperature of 3.20 g/cm^3 and 2700°C. A common hurdle encountered while forming Al/SiC composites using conventionally employed composite fabrication techniques is the significant difference in thermal expansion of coefficients (CTE) between two constituent components (Al and SiC) resulting in solidification issues. As a solid-state processing, FSP tackles the issues.

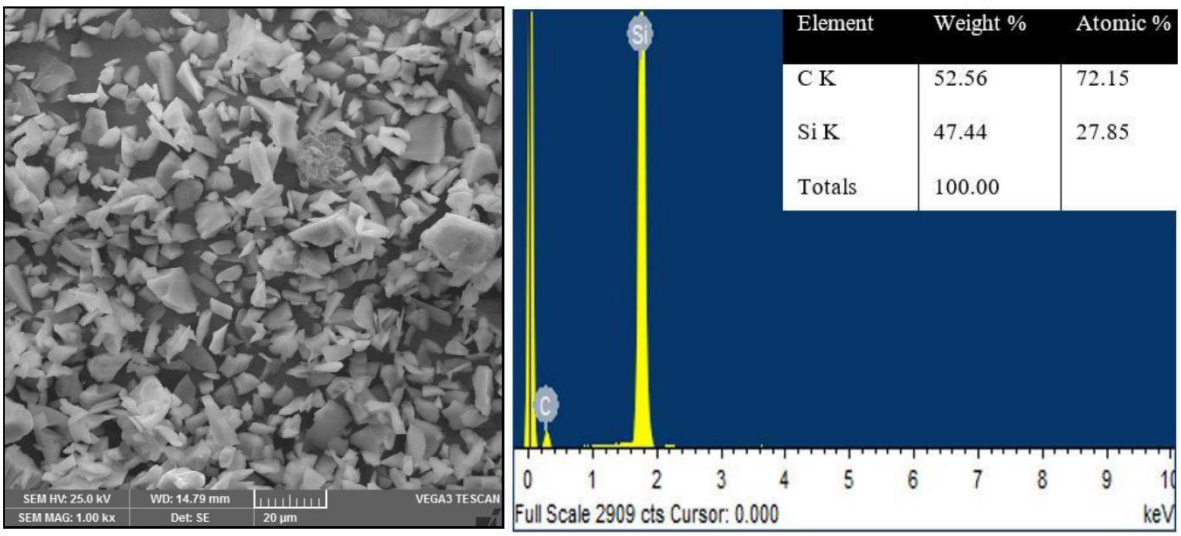

Fig. 3.1 SEM image of as-received SiC particles

FSP is a thermo-mechanical deformation process where the tool temperature approaches the work-piece to solidus temperature. Production of defect free stir zone (SZ) requires the proper selection of tool material. In this experiment, AISI H13 tool steel is selected as tool material. This is because of resistance to elevated temperature, wear resistance, shock resistance, machinability, availability and low cost. The typical chemical composition of H13 tool steel is presented in Table 3.3.

Table 3.1 Chemical composition of 6082-T6 aluminium alloy (wt. %)

Mg	Mn	Fe	Si	Cu	Cr	Al
0.82	0.61	0.29	0.82	0.1	0.23	Bal

Table 3.2 Physical properties of 6082-T6 aluminium alloy

Physical property	**Material (AA6082-T6)**
Microhardness (Hv)	96
Ultimate tensile strength	306
Yield strength (MPa)	236
Elongation (%)	13

Table 3.3. Chemical composition of AISI H13 Tool steel (Wt. %).

C	Mn	P	S	Si	Cr	V	Mo
0.42	0.28	0.015	0.003	1.00	5.20	1.05	1.45

3.3 Selection of tool profiles

The geometric features of tools are shown in Fig.3.2, with different pin lengths of 5.2, 3.2 and 1.7 mm for Tool A, Tool B and Tool C respectively. All the tools have the shoulder diameter equal to 24 mm. Each pin is conical in shape, has a threaded profile, with top and bottom ended diameters of 6 and 8 mm, respectively. Based on literature survey the ratio of shoulder diameter (D)/d (tool pin diameter) was used as 3:1 to achieve desired properties. The shoulder diameter was 24 mm and the tool pin diameter was 8 mm which is 3 times the diameter of shoulder.

To overcome the shortcomings of a conventional tool, an attempt was made to create an Al/SiC compositional gradient with a newly designed hybrid tool over a predefined length as per the developed process model. The novel HYB tool was fabricated and compared with CON tool to develop an Al/SiC gradient composite. Two different tools, conventional (CON) and hybrid (HYB), illustrated in Fig.3.3, were used for investigating the effect of tools on the microstructure and mechanical properties of the FG samples that were processed. The CON tool had a tapered threaded pin profile, with diameters of 6 mm at the top and 8 mm at the bottom. The HYB tool consisted of partly tapered threaded pin and square cross-section. The tool shoulder diameter for both the tools was 24 mm.

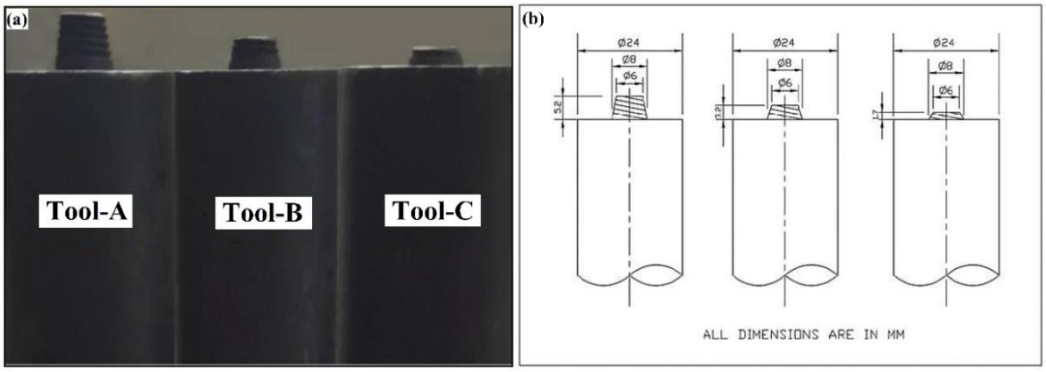

Fig. 3.2 (a) Tool geometries of the FSP tools and (b) dimensions of the FSP tools

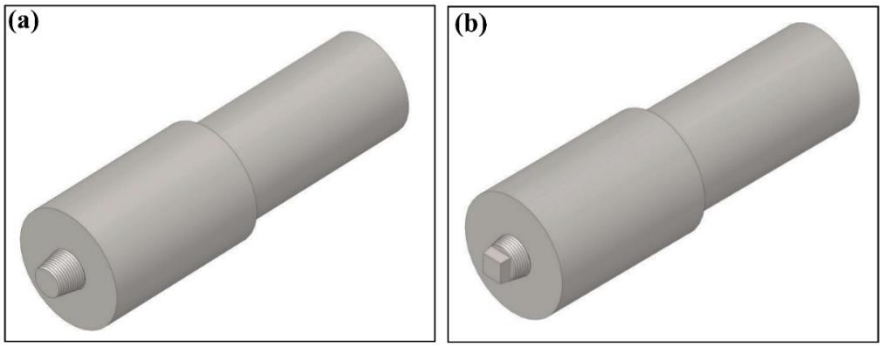

Fig. 3.3 FSP tools with different pin profiles (a) Conventional tool (CON) (b) Hybrid tool (HYB)

3.4. FSW machine details

FSP experiments were carried out using a three-axis numerically controlled friction stir welding machine (NCFSW-3T). The FSW machine is capable of maximum axial load of up to 3 tons. The basic components of FSW machine are spindle motor, servo motor, table with fixture, force and position controller, lubrication system, data acquisition and analysis software. The FSW machine is shown in Fig. 3.4. The specifications of the FSW machine are shown in Table 3.4.

The machine consists of rigid framework with a built-in guide, worktable and traveling head assembly with XYZ axis movement. The titling angle can be manually adjusted between 0 and 5 degrees. Dwell time and plunging speed can be controlled. The direction of rotation of the tool was clock wise, so that pin with left-handed threads could drive the flow of material against the surface of the worktable and forge it under pressure.

This equipment enables the FSP cycle to be controlled by either tool force control or tool vertical position:

- Upward tool position control - the vertical position of the tool remains constant during the cycle, considering the penetration of the tool defined in welding settings menu.
- Upward tool force control – the vertical position of the tool may differ as the force of the tool specified in the welding parameters remains unchanged.

To obtain the appropriate thermomechanical conditions for processing, depth of penetration of the tool, dwell time and tool plunge can be varied by position / force tool control. The tool plunge raises the temperature of the plate causing the material to soften and in addition, deeper penetration is required to attain the vertical force required to initiate the cycle. A dwell time controlled by tool position is more appropriate because plunging of tool corresponds to proper depth at the start of processing and the force of plunge will be closer to applied force during processing. After dwell time, it is preferable to utilize tool force control to ensure process parameter consistency in all trails.

A data acquisition system deployed can track and record process parameters like torque, force, tool location (X, Y, Z) and velocity in real time.

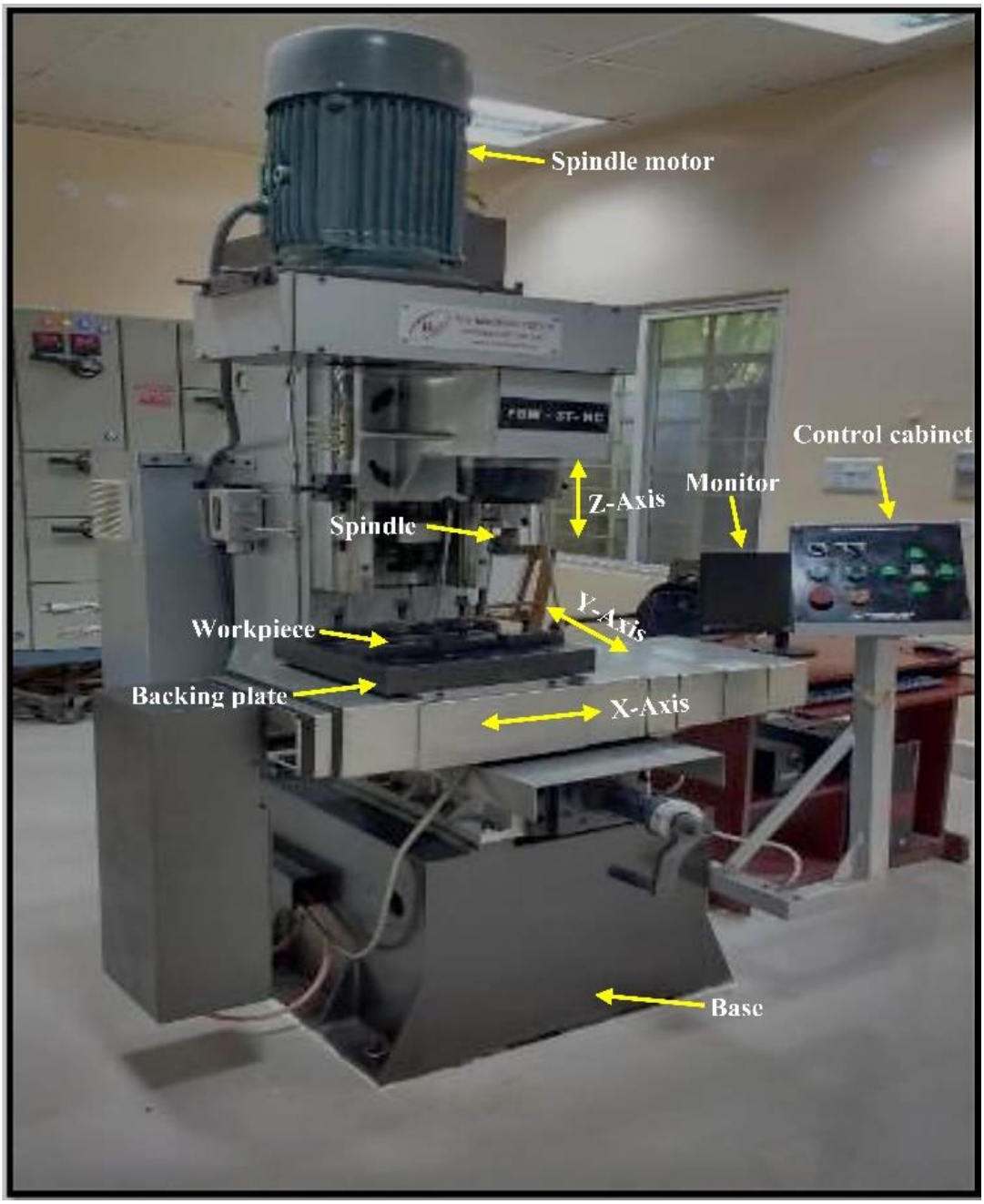

Fig. 3.4. Friction stir welding machine

Table 3.4. Specifications of Friction Stir Welding Machine

Make	R.V. Machine Tools
Machine size	1350(L) X 1750(W) X 2290(H)
Spindle Taper	ISO 40
Spindle Drive	Induction Motor 11kW, 3Phase
Spindle Speed	3000 RPM (Max)
Head Tilting angle	± 5°
Table with threaded holes	500 x 400mm
Z-axis thrust force	50KN (max)
X-axis thrust	25KN
Z-axis travel	300 mm
Y-axis travel (manual) (Optional: Servo)	100mm
Feed Force	3000kgf
Table to spindle nose (min/max)	100mm/400mm
Controller	PC based 2 mode Control Force & Position
Data Acquisition & Analysis-Software	Input & output data Spindle rpm, Torque axis force and velocity against time and distance
Power Rating	32 KVA
Wieldable Material	Steel/Copper/Aluminum

3.5 Methodology

- Conduct preliminary test to obtain defect-free state (combination of rotational speed and traveling speed) by using the appropriate tool geometry.
- Conduct the experiments with an average composition of 6 vol.% of SiC
- Determine the novel reinforcement approaches to attain microstructural gradient/gradation along the thickness direction
- Implement and experiment with novel reinforcement approaches (multi-step friction stir processing (FSP) and develop a mathematical model for positioning holes)
- Analyze the mechanism of the process responsible for improved mechanical properties of functionally graded (FG) samples

3.6. Experimental setup

The fabrication of functionally graded samples (FG) by FSP is schematically illustrated in Fig.3.5. and comprises the following steps. At first, a groove was made on 6082-Al plate with a width and depth of 1.5 mm and 5 mm respectively, using wire cut EDM compacted with 6 vol. % of SiC particles. After filling with SiC particles, a pin-less tool was used to seal the top surface of the groove, to prevent the sputtering of reinforcement particles during processing. Once the groove was sealed, the samples (6082-Al plate) were subjected to different pass numbers from one to three with Tool-A. To form an FG composite, the processed zone was again grooved with a width and depth of 0.5 mm and 3 mm respectively. Subsequently, it was filled with 8 vol. % (cumulative) of SiC particles and sealed. Following this, the sample was again processed with Tool-B and grooved once again with the width and depth of 0.6 mm and 1.5 mm respectively. It was packed with 10 vol. % (cumulative) of SiC particles and sealed. As a final step in the processing, the sample was processed with Tool-C.

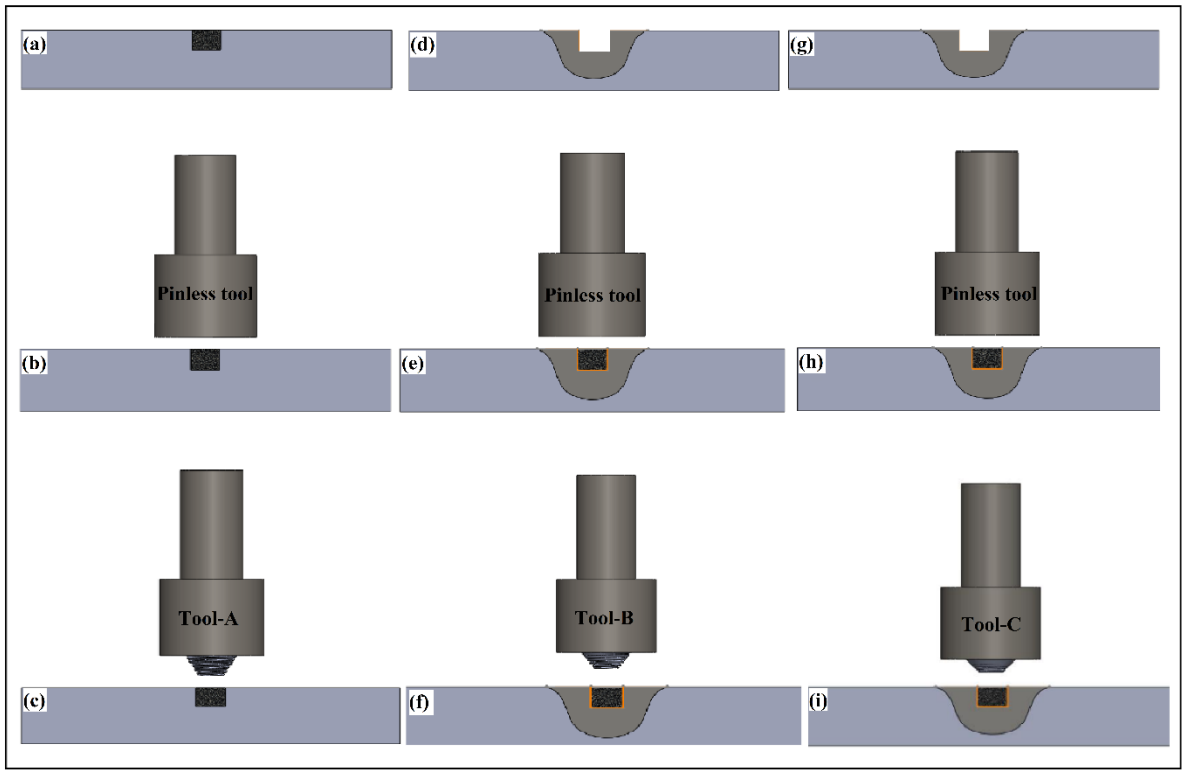

Fig. 3.5. A schematic representation of the fabrication process of FG composite via. FSP (a) Groove filled with SiC particles, (b) Sealing of groove using a pinless tool, (c) Processing of composite zone-1 using Tool-A, (d) Secondary groove filled with SiC particles, (e) Sealing of secondary groove using a pinless tool, (f) Processing of composite zone-2 using Tool-B, (g) Filling of SiC particles in a tertiary groove, (h) Tertiary groove sealed using a pinless tool, (i) Processing of composite zone-3 using Tool-C

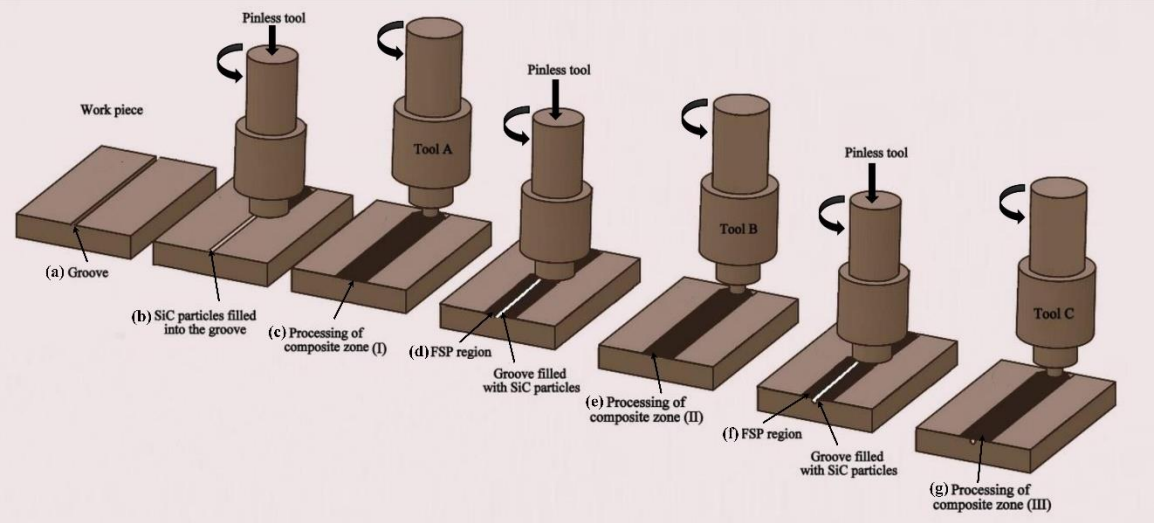

Fig. 3.6. A schematic representation of the processing of FG composite via. FSP

3.7. Characterization techniques

3.7.1. Metallography study

3.7.1.1. Sample preparation

In order to evaluate the microstructural features and mechanical properties (mainly wear behavior and microhardness) of the FG samples, the fabricated samples were sectioned normally to the processing direction as per ASTM standards using Electrical discharge machine (EDM). To study the microstructural characterization, the processed samples were polished with different grades of SiC abrasive papers as shown in Table 3.5. Later, the samples were polished using double disc (8" Double Disc Polisher) polishing machine (shown in Fig. 3.7 and listed in Table 3.6) with velvet cloth and aluminum oxide slurry to attain a mirror finish. Finally, etching was done with Keller's reagent at room temperature till the preferred contrast was attained.

Table 3.5 Different grades of abrasives for microscopic study

Sl. No	Abrasive (Grit SiC paper)	Time (sec)
1	200	90
2	400	90
3	600	90
4	800	90
5	1000	120
6	2000	120
7	3000	120
8	4000	120

Fig. 3.7. Disc polishing machine

Table 3.6 Technical specification of Disc polishing machine

Sl. No	Details	Specification
1	Variable speed	50-1000 rpm
2	High torque motor	0.5 HP
3	Drive speed	Variable
4	Water jet with control valve	Flexible
5	Aluminium disc 8” diameter	2 Nos
6	Spring	1 No
7	Stainless steel holding ring (Press type)	1 No
8	Size	710 x 660 x 310 mm

3.7.2. Three-Dimensional Optical Microscope

The microstructural features of FG samples were examined by 3D light microscopy as depicted in Fig. 3.7 Model: HUVITZ LUSIS HC-30MU. The complete specifications are listed in Table 3.7. The Z-axis autofocus helps the simple acquisition of 2-D images with samples of varying focal depths of the processed surface. It helps to study the distribution of the reinforcement particles into the base material at lower magnifications with effective results through Panasis software.

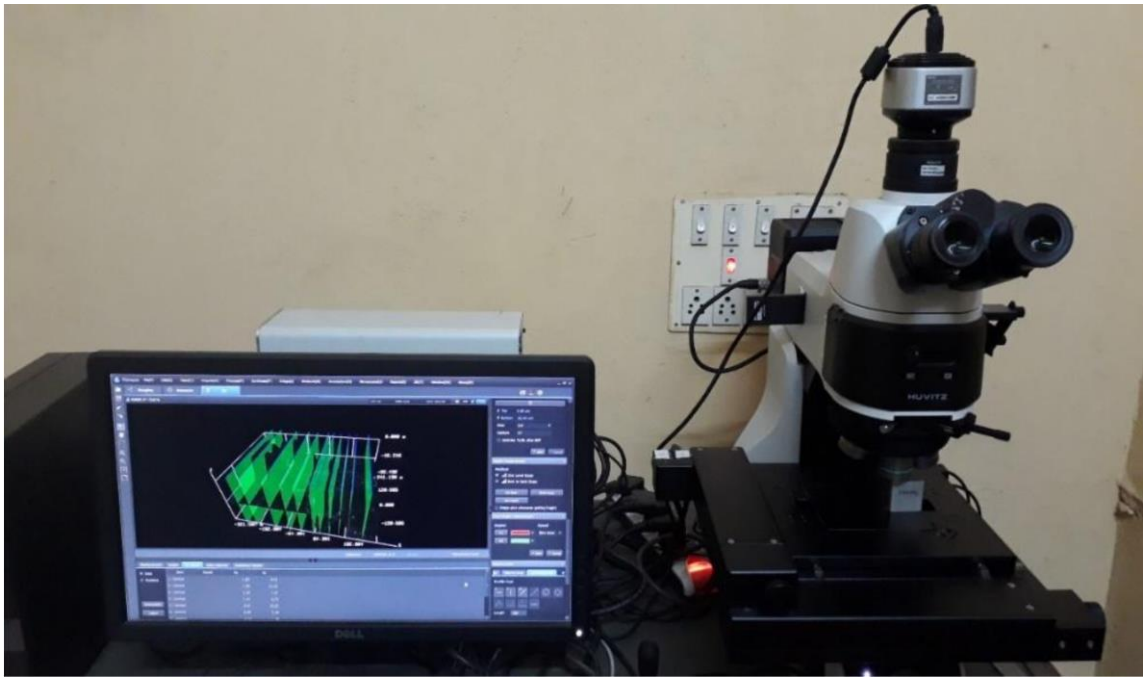

Fig. 3.8. Optical type 3-D microscope

Table 3.7 Specifications 3-D optical microscope

Z-axis module Specifications	
Stroke Distance	30mm
Resolution	0.01µm
Repeatability	0.5µm
Maximum Speed	1.4mm/sec
Weight	5kg
Dimensions	Width:240mm; Depth: 157mm; Height: 202.5mm
Load capacity	15kg
Microscope Specifications	
Eyepiece	10x Wide Field, Diopter Adjustable
Observation Tube	Trinocular Erect
Mountable Objective Lens	Plan Fluor EPI 5X, 10X, 20X, 50X and 100X
Accuracy and repeatability	Accuracy of magnification ±15 - ±20µm, repeatability of magnification±10 - ±15µm
Lamp Halogen	12V, 100W halogen lamp
Camera	Image sensor, 3 megapixels
Illumination	Reflected bright field/dark field/ polarized

Filter	Neutral Density Filter, Differential Interference contrast filter
Focusing Unit	Stroke 30-45 mm, Resolution 0.01 – 0.05µm, maximum sample height 15-25mm
3D Imaging and measurement	Panasis professional

3.7.3. Scanning electron microscope (SEM) & Electron backscatter Diffraction (EBSD)

Detailed microstructural analysis, failure analysis, corrosion analysis and surface morphologies of worn-out FG samples were carried out using scanning electron microscopy (SEM), as shown in Fig 3.8. SEM is a type of electron microscope that produces images of a sample by scanning it with a focused beam of electrons. The electrons interact with atoms in the sample, producing various signals that contain information about the sample's surface topography and composition. SEM is a completely computer-controlled unit with a conventional tungsten-heated cathode intended for high and low vacuum operations. It is sophisticated, user-friendly software for controlling the microscope and capturing the image using windows platform and has superior optical properties, offers good clarity of flicker-free digital image, fine processing, and excellent measurements, has images stored in standard formats, provides an automatic arrangement of the electron microscope and several other automated processes and these among the specific features of the equipment. The technical specifications of SEM are given in Table 3.8.

Electron Backscatter Diffraction (EBSD) is a technique that uses SEM to provide crystallographic characteristics about a sample's microstructure. The EBSD analysis was conducted using (Oxford EBSD instruments) shown in Fig. 3.19. The samples for EBSD analysis were sectioned from SZ and electro-polished in perchlorate alcoholic solution for 25 sec at a temperature of -10^0 C. At the center of SZ, EBSD analysis such as angle misorientation and grain evolution were conducted.

Fig. 3.9. Scanning Electron Microscopy

Fig. 3.10. Electron Backscatter Diffraction

Table 3.8 Technical specifications of SEM

Make/Model	Tescan, VEGA 3 LMU
Electron Gun	Tungsten heated cathode
Resolution	3nm at 30kv / 2nm at 30 kb
Magnification	2x – 1,000,000x
Maximum field of view	24mm at WD30 mm
Accelerating Voltage	200V to 30kV
Probe current	1pA to 2µA
Scanning Speed	From 2ns to 10ms per pixel adjustable continuously
Chamber suspension	Pneumatic
Specimen Stage	Compucentric, fully motorized

3.7.4. Energy dispersive spectroscopy (EDS)

Energy dispersive spectroscopy (EDS) is an analytical technique that is used for the chemical composition or elemental analysis of a material. EDS is also known as Energy Dispersive X-ray spectroscopy (EDXA). The EDS measurements were carried out using SEM equipped with EDS system. It is an analytical technique used for the elemental analysis or chemical characterization of a sample. It relies on the interaction of some source of X-ray excitation and a sample. Its characterization capabilities are due in large part to the fundamental principle that each element has a unique atomic structure allowing a unique set of peaks on its electromagnetic emission spectrum. The confirmation about the elemental composition of a specimen can be overlaid on top of the magnified image of the specimen by using a process known as X-ray mapping. The EDS was operated at an accelerating voltage of 20 kV and the measurements were performed at a step size of 20 to 100 µm. An EDS coupled with SEM, as shown in Fig. 3.10 was used in the present study.

Sub-grain size measurement

Line intercept method was employed for measurement of grain size. For the measurement of grain size ASTM E 112 standard was used.

Fig. 3.11. SEM equipped with EDX

3.7.5 X-ray diffraction (XRD)

PANalytical's X-ray diffractometers was used to study the phase formation of fabricated sample. A detailed specification of PANalytical's X-ray diffraction is given in Table 3.9 and schematic diagram of machine is shown in Fig. 3.11.

Fig. 3.12. X-Ray diffractometer

Table 3.9 Specifications of X-Ray diffractometer

Sl.No.	Details	Specifications
1	Make	PANalytical
2	Model	X'Pert pro
3	Diffraction type	DY 1850
4	Tube anode	Cu
5	Ration Alpha 1:2	0.5000
6	Divergence slit	Prog. Div. Slit.
7	Receiving slit	Prog. Rec. Slit
8	Generator voltage (kV)	40
9	Tube current (mA)	45
10	Detector	X'celerator
11	Data angle range ($^0 2\theta$)	20-120
12	Scan type	Continuous

3.8. Mechanical testing

3.8.1. Microhardness test

Hardness is defined as the resistance of the material to indentation. For conducting the microhardness test, the samples were prepared as shown in Fig. 3.13. According to the law of proportional resistance, the indentation surface is proportional to the force applied. In order to characterize the FSPed surface, hardness test was performed by using Vickers digital microhardness tester (Make: Chennai Metco Pvt. Ltd, Chennai, Model: ECONOMET VH-1 with monitor that includes CCD Camera, adapter) as shown in Fig. 3.12 and technical specifications mentioned in Table 3.10. In this method, an indenter of a straight diamond pyramid with an angle between opposite faces of 136°, is applied under a specific load onto the surface of the material to be tested for a set time interval. The microhardness measurement direction (X-Y) of samples fabricated with different pin lengths and newly designed hybrid tool over a predefined length as per the developed process model is shown in Figs. 3.13. The

use of 10X and 40X lens allows one to obtain a wider field of measurement. The hardness tester is equipped with digital microscope for observing the microstructure of specimens and hardness value which can be visualized directly on the LCD screen. It is used for all types of metals including steels, super alloys, ceramic based and coatings etc. For microhardness studies, usually, the range of load is taken to be 5g to 1000g and the dwell time is considered in the range 10 to 15sec.

Fig. 3.13. Vickers microhardness tester

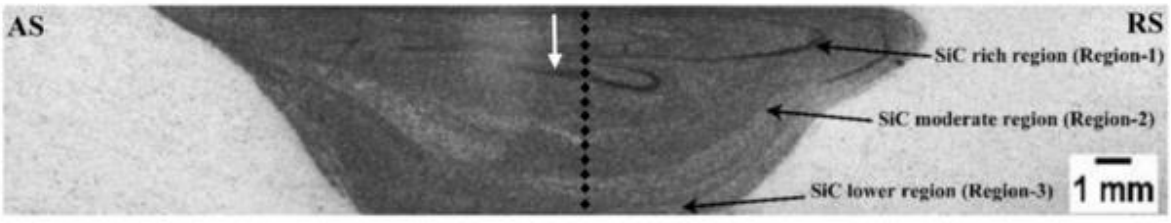

Fig. 3.13. Microhardness measurement in transverse direction

Table 3.10 Specifications of microhardness tester

Sl.No.	Details	Specifications
1	Objective lens	10X and 40X
2	Testing force	10 gf to 1000 gf
3	Loading control	Automatic (Loading dwell and unloading)
4	Dwell time of the test force	0 to 60 sec
5	Resolution	0.0625 microns
6	Hardness measuring range	8-2900 HV
7	Data output	LCD screen display, Inside printer
8	Accuracy	EN-ISO6507, Instrument throat :95 mm
9	X-Y testing table	Dimension: 100 x 100 mm, Max mobile 25 x 25mm
10	Indenter	Diamond
11	Power supply	10V/230V, 60/50 Hz
12	Overall dimensions	405 x 290 x 480 mm

3.8.2. Tensile test

Tensile test samples were prepared from the fabricated FG samples using Wire cut EDM machine. The samples were prepared according to ASTM-E8 standards from the processed specimen, transverse to the processing line. The dimensions of tensile specimen geometry are shown in Fig.3.14. The tensile tests were carried out at 0.1 mm/min constant cross head speed. Before starting the experiment, all the gauge lengths of the specimens were measured and recorded. The tensile strength was determined using Instron 300 LX universal testing machine (UTM) shown in Fig. 3.15. The UTM is highly versatile and different tests can be performed on it by changing the die set on the hydraulic actuator. Hydraulic wedge grippers were used for the tensile tests. The grippers have control for adjusting the griping force on the specimen and the grippers are equipped with rough surface to hold the specimens without slipping. The UTM machine is equipped with a data acquisition system that aids in the recording and saving of data obtained during the test process. The data from the acquisition system can be accessed and processed to give final results and graphs to estimate the behavior of the metal under various loads. The specifications of the UTM are given in Table 3.11.

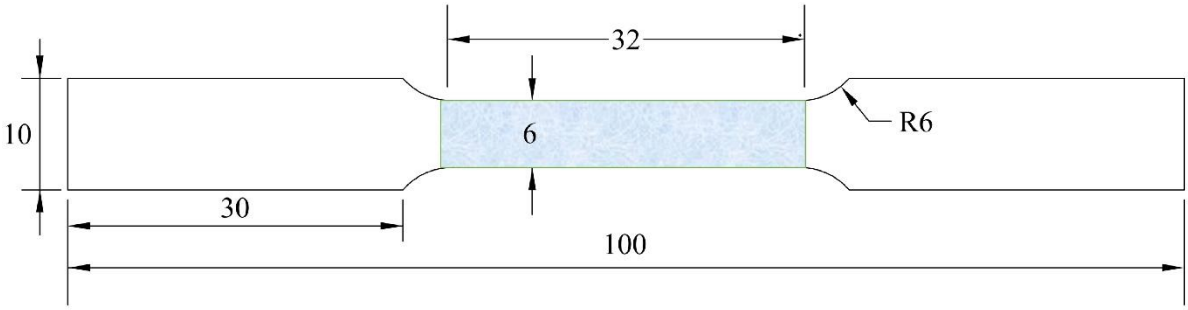

ALL DIMENSIONS ARE IN MM

Fig. 3.15. Specimen dimensions for the tensile test (ASTM-E8)

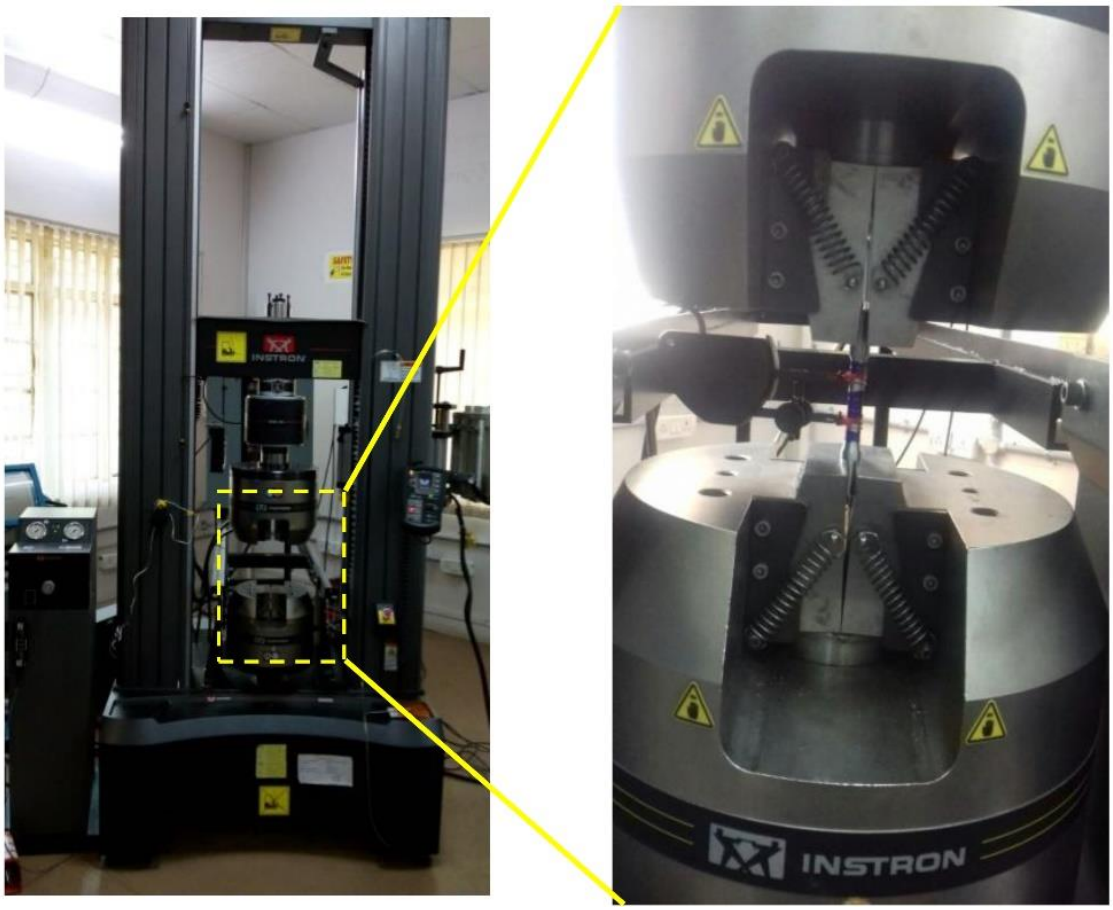

Fig. 3.16. Instron 300 LX universal testing machine (UTM)

Table.3.11 Technical specifications of UTM (Instron 300 LX)

Sl.No.	Details	Specifications
1	Model	Instron 300 LX
2	Capacity	20 kN
3	No. of columns	2
4	Max. speed (mm/min)	500
5	Min. speed (mm/min)	0.01
6	Max. force at full speed (kN)	20
7	Max. return speed (mm/min)	1000
7	Position control (mm)	0.5
8	Total crosshead travel (mm)	1130
9	Max. power required (VA)	1000
10	Dimensions (l x b x h) (mm)	760 x 600 x 2000

3.8.3. Wear test

Wear test was performed on a pin-on-disc (POD) equipment (refer Fig. 3.16) as per ASTM G99–04 standard by volume loss method. The test specimens of 10 mm diameter were sectioned from the stir zone (SZ). EN31 steel (with surface roughness (R_a) of 0.1 μm and hardness (HRC) of 62) was used as a counterpart. The tests were carried out at ambient temperature (30–35 °C). In each trial, sand paper with grit size of 80 (Ø50 mm) was fixed on the wear track to serve as abrasion medium. The samples having a contact area of 78.5 mm^2 were maintained for each sample. The abrasion wear test parameters are listed in Table 3.12. The wear test was run with no lubrication under a constant load value of 15 N and sliding distance value of 75 m. All test specimens were thoroughly cleaned with acetone prior to and subsequent to the wear test. Each individual trial was repeated three times to calculate weight loss and the average rate of wear was then taken. An accurate analytical weighing balance of 0.0001 g resolution was used to measure the initial and final weights of samples. After wear test, the surface morphologies of worn-out specimens were characterized by SEM.

Wear rate was calculated by:

$$W_v = \frac{\Delta V}{S}$$

where W_v is volumetric wear in $mm^3.m^{-1}$, ΔV is the volume loss in mm^3, and S is the sliding distance in m.

Table 3.12 Summary of abrasive wear test conditions

Parameter	**Value**
Applied force (N)	15
Counter-body	EN31
Pin diameter (mm)	10
Sliding velocity (m/s)	0.5
Sliding distance (m)	75
Track diameter (mm)	50
Time (mins)	10
Temperature (^{o} C)	Room temperature
Test environment	Air

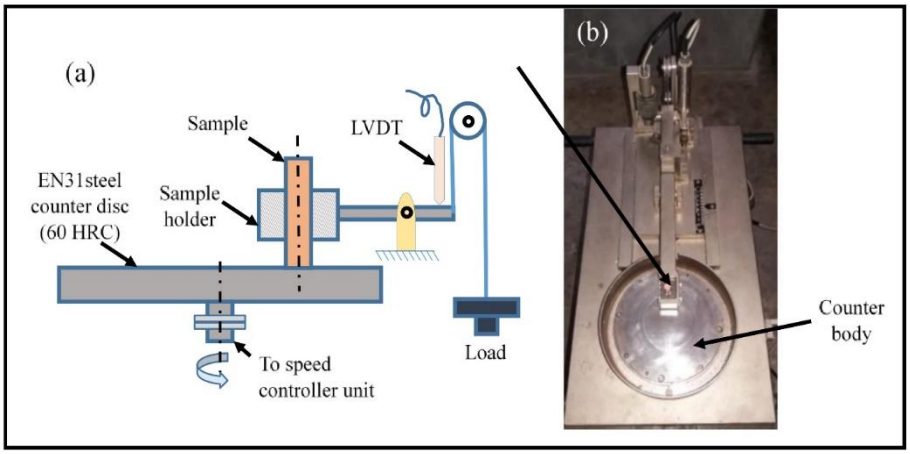

Fig. 3.17. Pin-on-disc wear test setup (a) Schematic representation and (b) Photograph of sliding wear tester.

3.8.4. Corrosion

To study corrosivity of the sample, corrosion tests were carried out in a 3.5 % NaCl electrolytic solution at ambient temperature using PARSTAT 4000 Potentiostat/Galvanostat electrochemical workstation/analyzer (refer Fig.3.17). Polishing of working electrodes (FG samples) was done using emery papers of up to 2000 grit size and the samples were thoroughly washed with distilled water. The 3-electrode system consisted of an FG sample as working electrode, a counter (auxiliary) electrode and a reference electrode of platinum wire and a saturated calomel electrode (SCE), respectively. Open circuit potential (OCP) versus SCE was monitored for 10 min before polarization. The range of potential difference maintained was

between -0.5 and 0.5 V at a scan rate of 0.166×10^{-3} mV/S. The surface area of 0.26 cm^2 was exposed to a corrosive environment (3.5 % NaCl electrolytic solution). All electrochemical experiments were conducted at least two times for repeatability. Finally, the corroded surface area of FG samples was achieved using SEM.

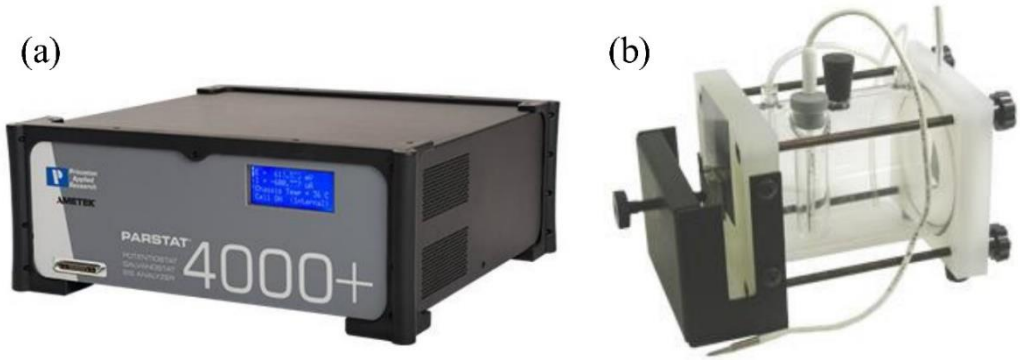

Fig. 3.18. The photograph of the corrosion test setup. (a) Corrosion work station and (b) corrosion test cell.

3.9.Perform the experiments according to the schedule given below

3.9.1. Determine the operating range of the selected process parameters

Pilot experiments were conducted using one factor-at-a-time approach. The working range of tool rotational speed, and weld speed was explored using taper threaded cylindrical tool of varying pin lengths and hybrid tool. It was observed that better mechanical properties were achieved at a tool speed of 900 rpm and a welding speed of 20 mm/min. The experiments were performed in accordance with the plan presented in Table 3.13.

Table 3.13 FSP process parameters to conduct the experiments

Process parameters	Values
Pin profile	Concave shoulder tapered threaded cylindrical
Rotational speed (rpm)	700, 800, 900
Travelling speed (mm/min)	20,30,40
Axial Force (KN)	5
Pin length (mm)	5.4
Shoulder diameter (mm)	24
Pin diameter (mm)	7
Tilt angle (degree)	1º
Tool material	AISI H13 tool steel

Chapter-4

Characterization of aluminum based functionally graded composites developed via friction stir processing

4.1. Introduction

This chapter reports the preliminary results that were obtained in the optimization of process parameters. The effect of tool rotational speed, traverse speed and reinforcements particle (SiC) on microstructure were studied. Al/SiC Functionally Graded Material (FGM) was developed through a novel multi-step friction stir processing (FSP) method. To create a graded structure over a predefined value, FSP was carried out with three tools, each of different pin lengths and with varying volume fraction of SiC particles. Microstructural features of Functionally Graded (FG) samples were examined using Scanning Electron Microscopy (SEM) and 3D light microscopy. Mechanical properties in terms of wear resistance and microhardness were thoroughly assessed.

4.2. Effect of tool rotational speed and transverse speed on base material

Fabrication of FGM by FSP is mainly affected by process parameters (tool rotational speed and traverse speed) and tool geometry. Detailed investigation was done to understand the effect of process parameters on material flow behavior, defect formation and microstructure formation. Determination of the most effective process parameters for fabrication of FGM as well as their influence on the microstructure, the mechanical and the wear properties was then done.

In order to obtain defect-free combination, AA6082-T6 was initially processed with various combinations of process parameters listed in Table 4.1. The shoulder geometry of 24 mm was selected for processing the base material.

Table 4.1 Different combinations of process parameters

Tool rotational speed (rpm)	Tool transverse speed (mm/min)
700 ,800 and 900	20, 30 and 40

From visual inspection, it was evident that the processed surface area of the base material (refer Fig.4.1)was formed with semi-circular structure with crowns (material flash) on the retreating side (RS) [128]. The processed surface was free from defects and macro-deformations in all the samples. The surface finish of the processed area varies depending on rotational and transverse speed. All the samples were processed with single FSP pass. The appearance of the samples produced was good, showing the properties of an exit hole at the end of the process.

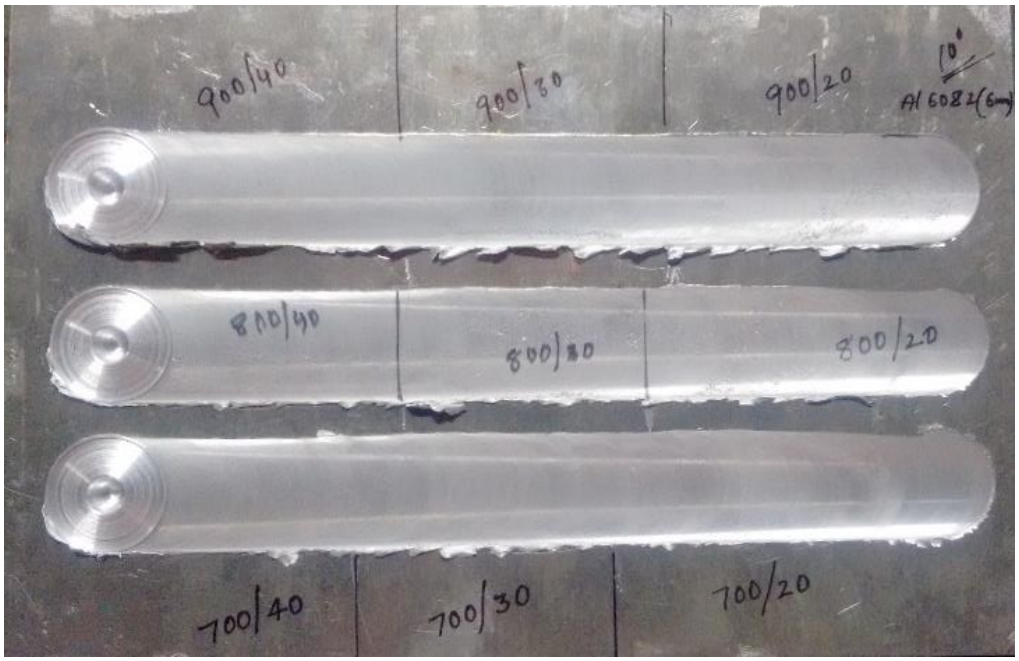

Fig. 4.1. Surface appearance of processed AA6082-T6 sample

In friction stir processing, fabrication of defect-free surface composites mainly depends on the process parameters such as tool rotational speed, traverse speed, etc. The improper combination of the process parameters leads to defective surface composite and also influences the surface quality of the composite.

From Fig. 4.2 an attempt was made to explain the influence of process parameters and tool shoulder geometry on base material without reinforcement. In this research work, the base material was processed by varying the combinations of process parameters. At a constant tool speed of 700 rpm with varying travel speeds of 20, 30 and 40 mm/min, onion rings were formed. It was caused due to incorrect combination of rotational speed and transverse speed. Too high traverse speed and too low rotational speed led to the formation of onion rings. However, throughout this time period, the material flow was not always capable of completing entire rotations. In the processing zone, the material reverses direction and forms several onion rings (At 800 rpm - 40 mm/min).

At 900 rpm with a lower tool traverse speed of 20 mm/min, the deformation in the stir zone was high with reduction in onion rings. From the microstructural studies, it was confirmed that selected process parameter (900 rpm-20 mm/min) was able to produce sufficient heat input with no defects. A higher interaction time of the friction leads to higher plastic deformation, helps to plasticize a large proportion of the material that leads to form fine grains without defects.

	20 mm/min	30 mm/min	40 mm/min
700 rpm			
800 rpm			
900 rpm		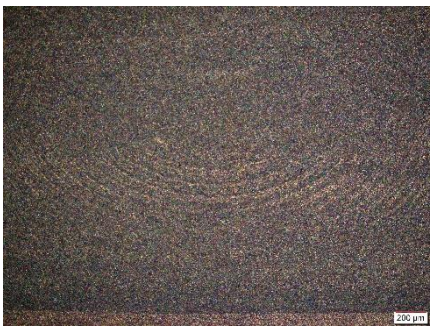	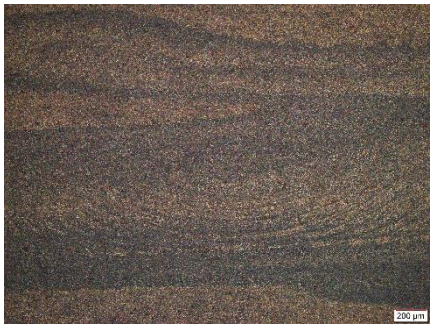

Fig. 4.2. Microstructures of processed AA6082-T6 at different tool rotational and transverse speeds

(a) 700 rpm – 20 mm/min

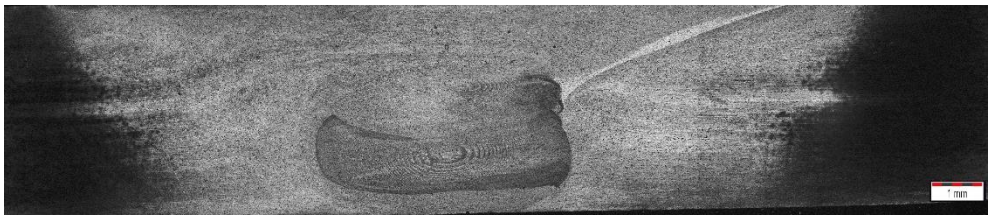

(b) 700 rpm – 30 mm/min

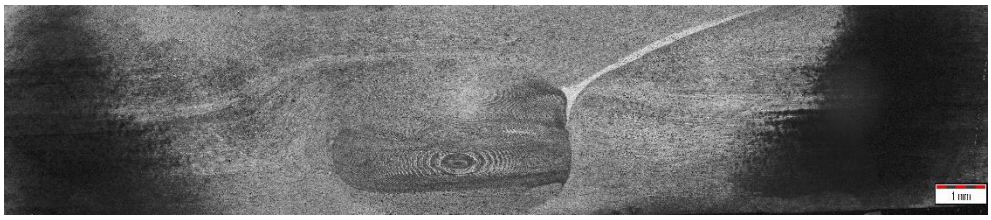

(c) 700 rpm – 40 mm/min

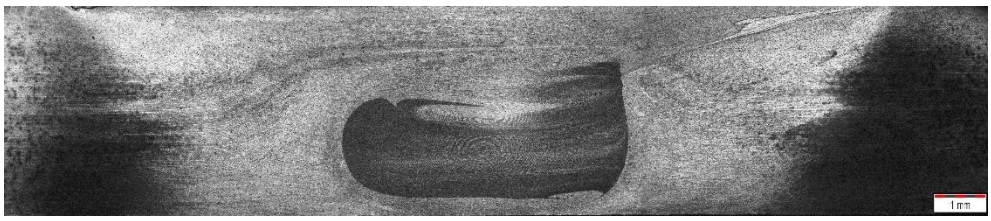

(d) 800 rpm – 20 mm/min

(e) 800 rpm – 30 mm/min

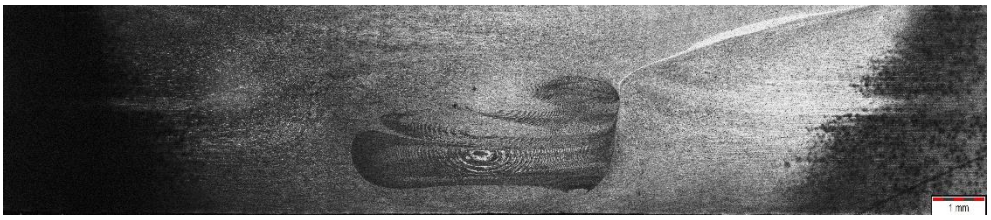

(f) 800 rpm – 40 mm/min

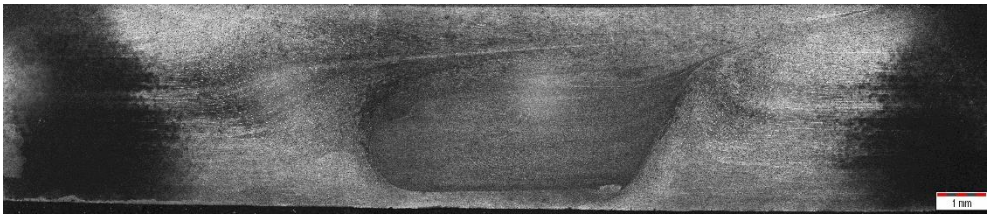

(g) 900 rpm – 20 mm/min

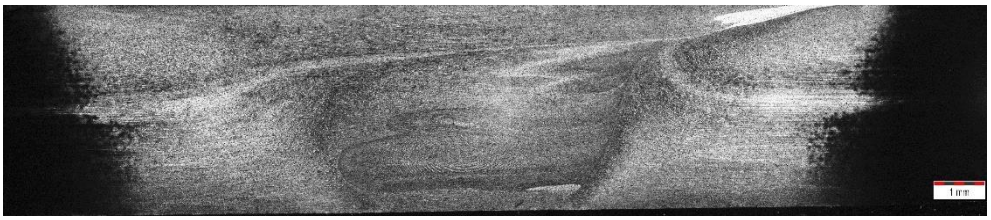

(h) 900 rpm – 30 mm/min

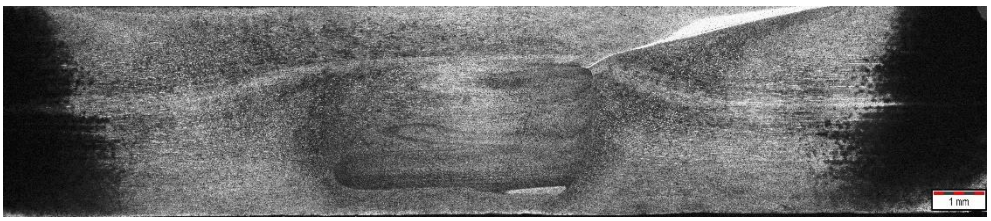

(i) 900 rpm – 40 mm/min

Fig. 4.3. Macrostructure of AA6082-T6 processed at different processing conditions

Symmetrical basin shape can be observed clearly in SZ (area – 14.79 mm^2) at this condition (900-20) due to sufficient flow of material from advancing side to retreating side during processing. Shoulder plunging into workpieces creates high friction and plastic flow in the upper zone, resulting in extensive changes in heat generation, heat distribution, stirred zone shape in the processed cross-section.

The onion rings observed in microstructures has reduced at this condition (900-20) when compared to other parameters. The effect of onion rings on properties has been the subject of research for many years and is not yet clearly understood. The formation of onion rings is a geometric effect due to the fact that cylindrical layers of material are extruded during each rotation of the tool and cutting through the section of material creates apparent onion rings. However, it is believed that these rings may have indirect effects on properties. Under a uniaxial stress field, the uniformity of the ring patterns may have little/no impact on the stress distribution across the weld joint. But any irregularity in the pattern can cause significant changes in the flow of stress and increase the probability of stress concentration. Stress concentrated regions are subjected to premature failure under stress field [129].

The hardness of the processed samples was tested under the same condition (100 gm load with 10s dwell time) and the results were shown in table. Higher microhardness values (106 HV) were obtained at 900 rpm and 20 mm/min condition. Optimum thermal conditions during processing are created when the tool geometry, plunge depth, rotational and transverse speed are optimized. This leads to the formation of a defect-free processed zone (SZ) with better mechanical properties.

Table. 4.2 Area of SZ and VHN at different rotational speed and transverse speed

Rotational speed (rpm) – Transverse speed (mm/min)	**Area of the stir zone (mm^2)**	**Microhardness (VHN)**
700-20	9.61	79
700-30	8.20	83
700-40	10.05	84
800-20	10.22	88
800-30	8.04	86
800-40	7.69	80
900-20	14.79	106
900-30	12.78	99
900-40	13.79	90

After the process parameters for the base material have been determined, the trials for fabrication of surface composite with reinforcement were carried out. The reinforcement strategy followed was the groove method. First, the groove was made on the 6082-Al plate and compacted with 6 vol.% of SiC particles. The sample was subjected to single FSP pass. Figure.4.3. shows uniform distribution of SiC particles in the SZ with combination of few coarse and fine reinforcement particles. This is due to low interaction time between the tool and the workpiece.

Additionally, the rotating tool offers sufficient heat and circumferential movement to disperse the reinforcing particles in the SZ. The dispersion of reinforcement can further be improved by increasing the number of passes. This microstructural analysis confirmed that for up to 6 vol.% of reinforcement, a microstructural gradient along the thickness direction can be produced.

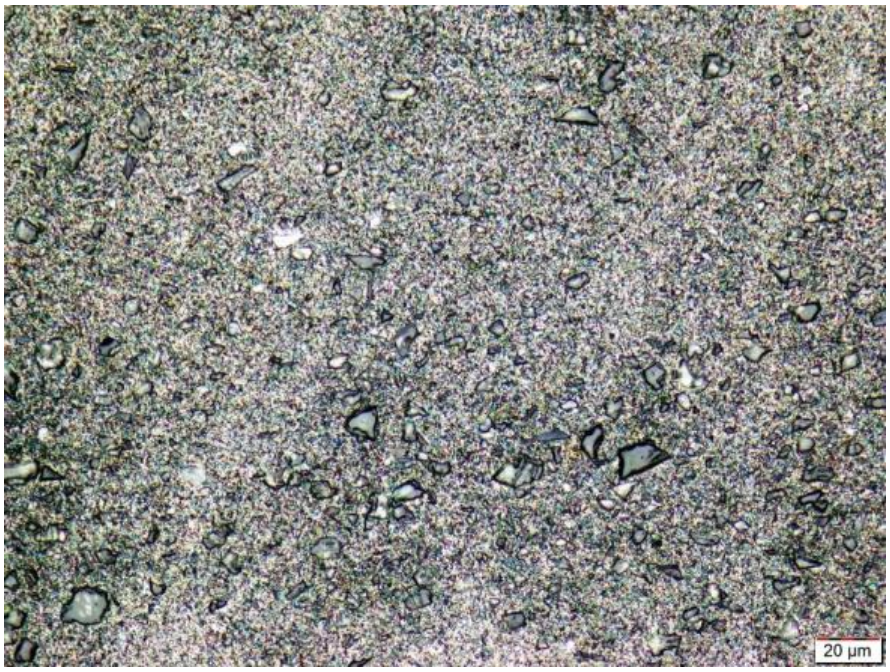

Fig. 4.4. SZ of Al6082-T6/SiC with 6 vol.% of reinforcement

4.3. Fabrication of aluminum based functionally graded composites developed via friction stir processing

4.3.1. SiC particle distribution

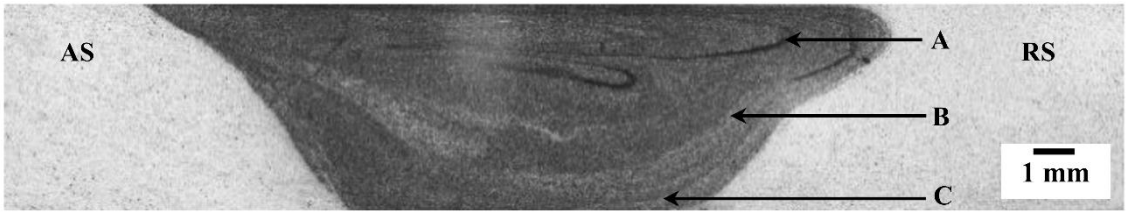

A: SiC rich region (Region-1 processed with Tool-C)**, B:** SiC moderate region (Region-2 processed with Tool-B)**, C:** SiC lower region (Region-3 processed with Tool-A)

Fig. 4.4. Macrograph of cross-sectioned Al/SiC FG composite

Fig. 4.4 illustrates a cross-sectional macrograph of the FG composite in which there is a gradation of the volume fraction of the SiC along the thickness direction. Moreover, it is revealed that good bonding between layers has been attained, and no cracks were observed in the microstructure. A typical network structure has been observed where SiC particles are dispersed throughout the matrix phase. The dispersion of SiC particles is found to be in a gradient manner. The FG sample consists of three regions from top to bottom, (1) Region-1: SiC rich region (10 vol. %), in which 6082-Al serves the purpose of a matrix phase. (2) Region-2: the continuous transition of the FG sample can be found in SiC moderate region with a

decreasing trend from 8 to 6 vol. % and (3) Region-3: Lower region with an average composition of 6 vol. % of SiC. The formation of graded regions from regions 1 to 3 was due to the multiple passes of Tool-A, B and C, respectively.

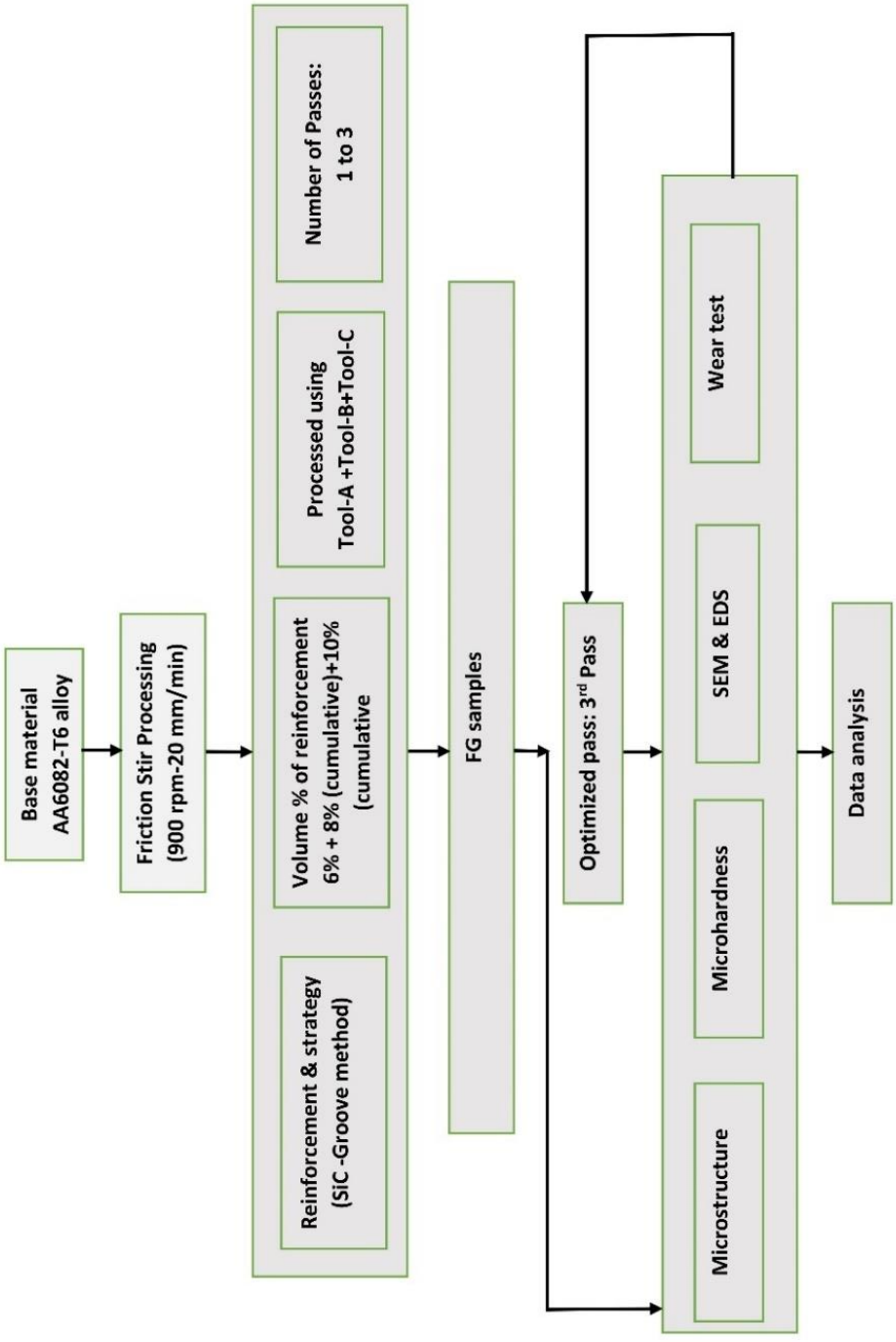

Fig. 4.5. Flow chart of processing steps for producing FG samples with multiple passes

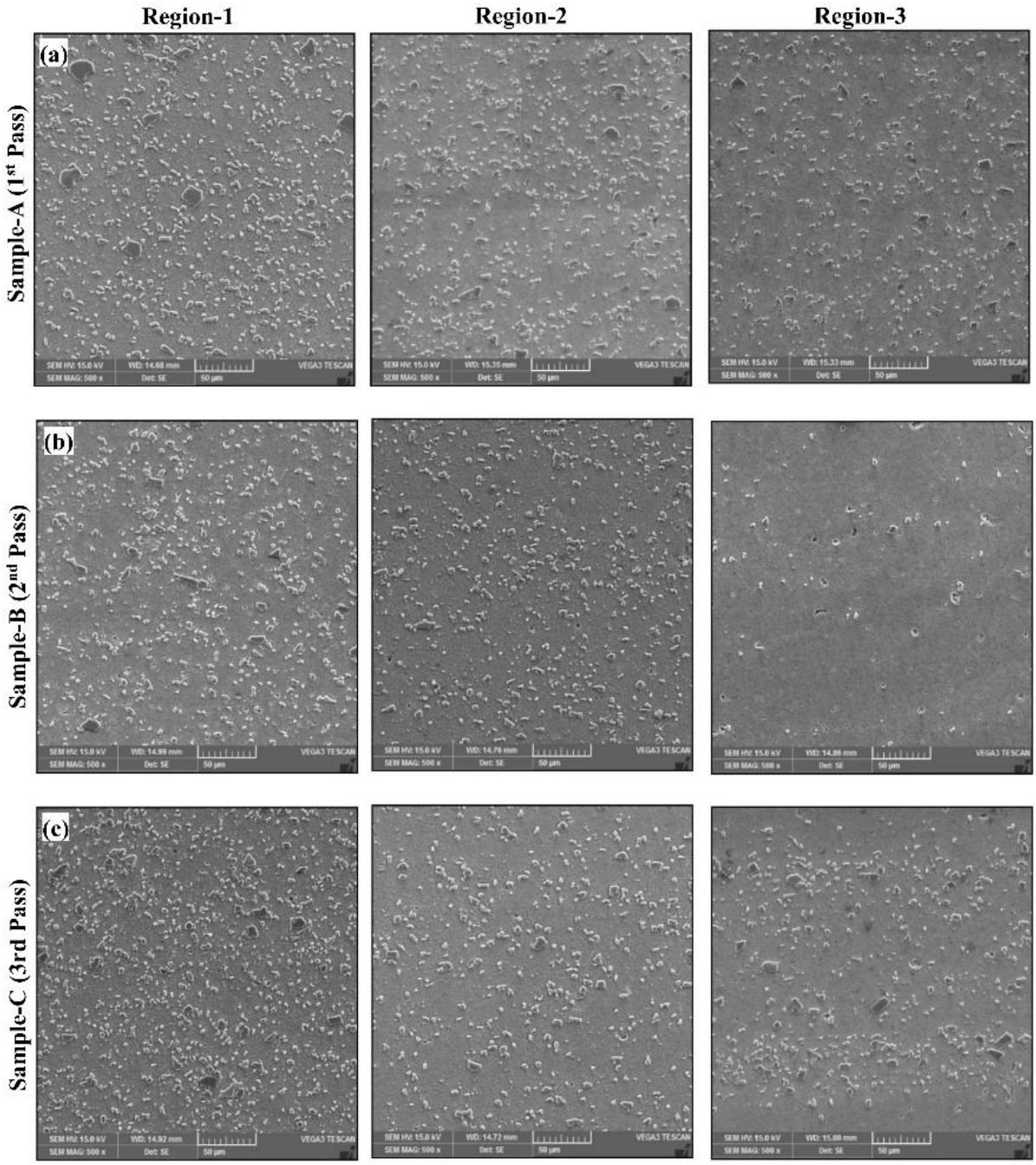

Fig. 4.6. SEM images showing microstructure of the Al/SiC FG composite at different regions fabricated by (a) one FSP pass for sample-A, (b) two FSP pass for sample-B, and (c) three FSP pass for sample-C

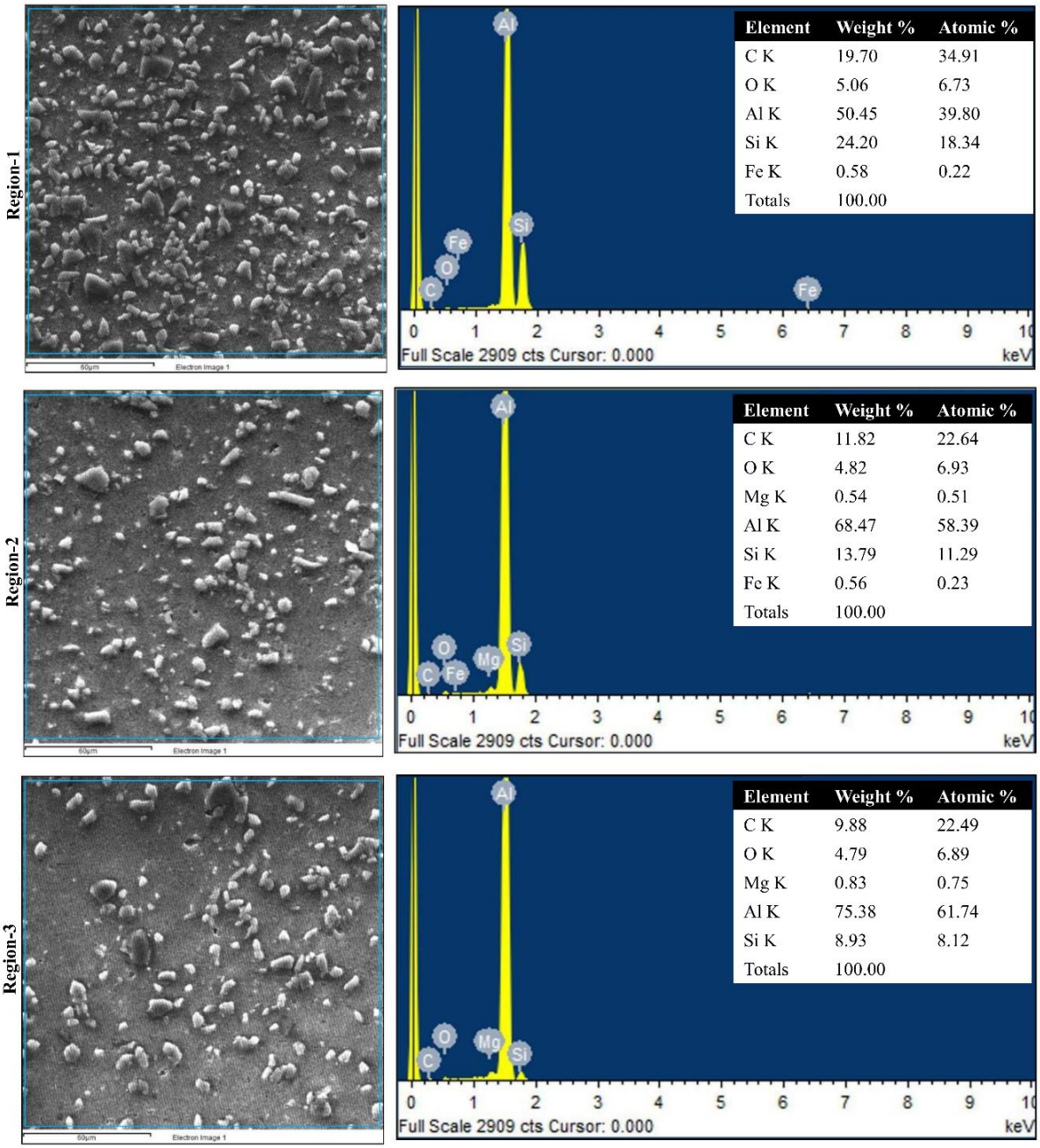

Fig. 4.7. EDAX analysis of sample-C taken from region 1, 2 and 3

Microstructures of FG samples (A, B and C) fabricated with 1 to 3 passes were observed through SEM in different regions. These are depicted in Fig.4.5. It is confirmed that a significant amount of SiC particles exist over matrix in FG composite and the presence of some fine and coarse SiC particles can be observed in the processed region. The EDAX analysis of the fabricated FG composite sample-C (Fig.4.5c) is shown in Fig.4.6. It can be seen that the elements C, O, Al, Si and Fe were detected in all chosen regions of sample-C. In the selected region EDAX, it was found that oxygen wt. % is over 4 which is due to the decomposition of

organic substance (acetone) under electron beam irradiation. When aluminum is exposed to the atmosphere it oxidizes quickly by forming an Al_2O_3 layer on the surface of the aluminum. In addition to the existing phenomenon, it was also observed that the concentration of SiC is gradually decreasing from region-1 to 3.

To understand the distribution of SiC particles, there was a need for finding the percentage change in the concentration in different regions. For this, phase fraction analysis was done according to ASTM E562 using SEM images at different regions of individual FG samples. Leica app suite 4.8 was used [130] to process the SEM images shown in Fig.4.7. When the phase fraction for all three passes was compared, it was observed that pass-3 had a better distribution of SiC particles than pass-1 and 2. From Table 4.2 and Fig. 4.5c it is clear that pass 3 disintegrates the SiC particles finely and this resulted in phase distribution in region-1, 2 and 3, these being 17.03 ± 0.8 vol. %, 12.19 ± 0.2 vol. % and 6.75 ±0.7 vol. % respectively. Similarly, as passes increase, the size of SiC particles decreases, which is discussed in the next section.

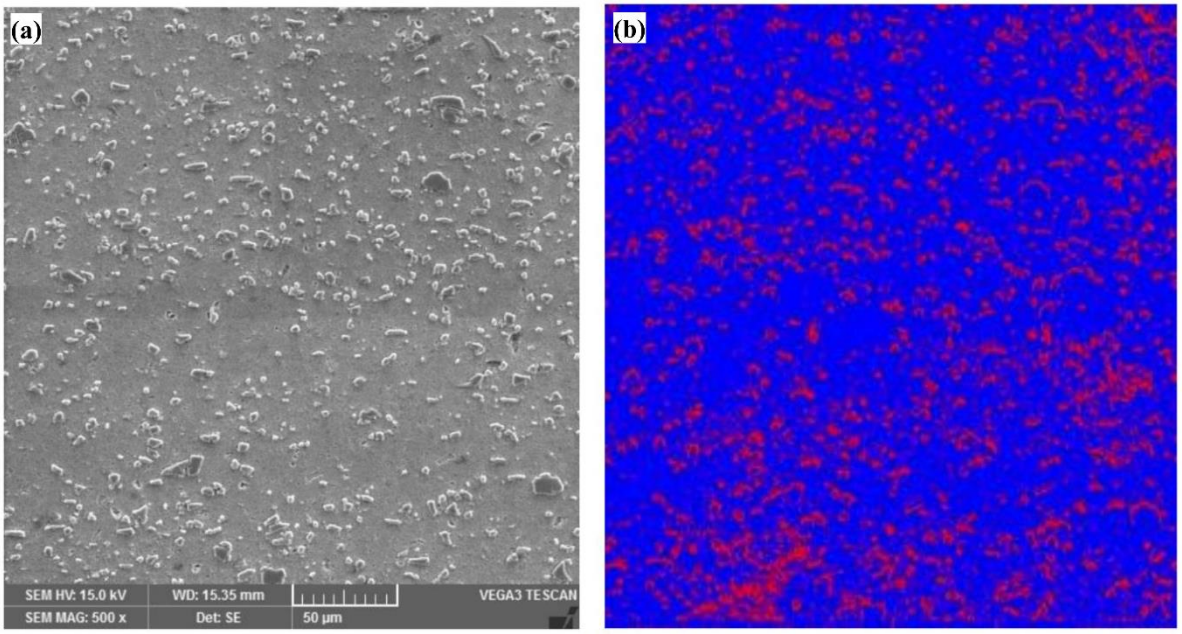

Fig. 4.8. Images during phase fraction analysis (a) Raw image of pass-2 at region-1 (b) Processed image of pass-2 at region-1

Table 4.3 Comparison of phase fraction at different regions with different FSP passes

Passes	Phase fraction summary at different regions					
	Region-1		Region-2		Region-3	
	% Al alloy	% SiC	% Al alloy	% SiC	% Al alloy	% SiC
1	85.97±0.3	14.03±0.3	88.50±0.1	11.50±0.1	90.82±0.4	9.18±0.4
2	87.62±0.6	12.37±0.6	89.37±0.5	10.63±0.5	97.15±0.3	2.85±0.3
3	82.97±0.8	17.03±0.8	87.81±0.2	12.19±0.2	93.25±0.7	6.75±0.7

4.3.2. Microstructure

Fig. 4.8 represents the macrograph of the FG samples in which SiC particles were embedded into the surface of the aluminum alloy. In FSP, the formation of fine and equiaxed grains within the stir zone was due to the occurrence of dynamic recrystallization (DRX) caused by the local pinning effect [131,132]. The intense plastic deformation within the stir zone causes fragmentation. Based on material transport and tool action, the processed area is divided into 3 distinct zones: (1) stir zone (SZ), (2) thermo-mechanically affected zone (TMAZ) and (3) heat-affected zone (HAZ) [133].

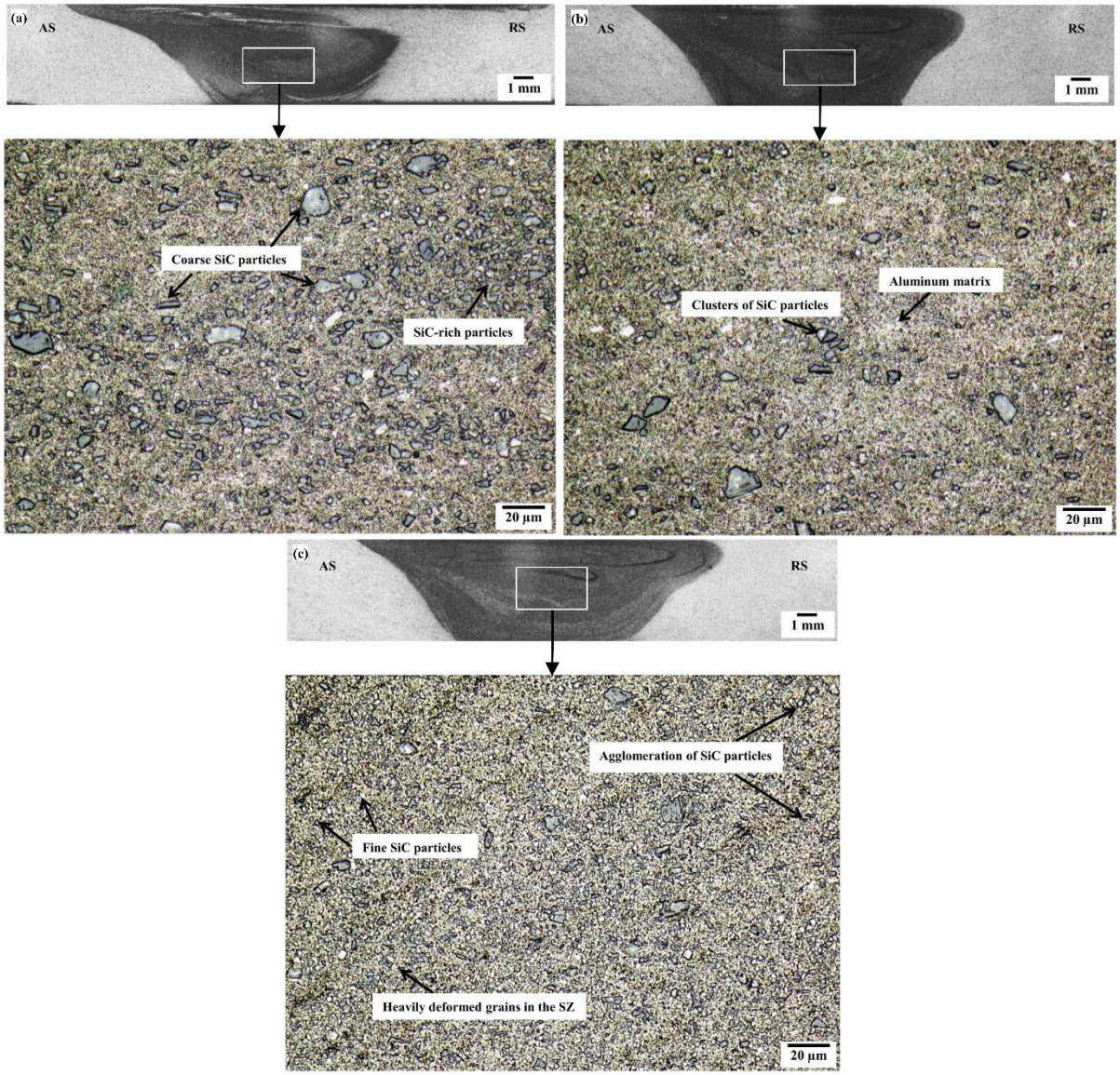

Fig. 4.9. Microstructures of Al/SiC FG composite near the SZ produced by (a) one FSP pass for sample-A, (b) two FSP pass for sample-B, and (c) three FSP pass for sample-C

The SZ shown in Fig.4.8a is of sample-A for 1st pass. It can be seen that the shape of SZ is asymmetric from the center because SiC particles have transported to the advancing side (AS) compared to the retreating side (RS). The plastic deformation zone is inadequate for the forming of SiC particle recirculation flow because there is low interaction time between workpiece and tool [134]. The grains formed have a large area of grain boundaries. The surface composite layer is formed by first-pass showing particle agglomeration on the surface.

However, when the number of FSP passes was increased, particle dispersion was found to be more homogenous and any clusters of SiC particles that were remaining were broken leading to the creation of a higher number of SiC–Al alloy matrix interfaces. During the second pass, the particle dispersion became more uniform (refer Fig.4.8b) when compared to the first pass and the cluster size of SiC reduced while dispersion in upper and lower regions of stir zone was not homogenous, which indicates that stirring action was insufficient in achieving uniform particle dispersion.

To further improve the distribution of particles in the upper and lower region of the stir zone, a third pass was required. Fig.4.8c shows the microstructures of SZ produced with the third pass where micro-clusters of SiC cannot be seen any more in the sample with refined structure and there are no defects. The dispersion of particles is more uniform in the upper and lower regions of the stir zone. In addition to this, symmetric i.e., basin shape of SZ was observed on both AS and RS, representing homogenous as well as uniform deformation within SZ. The wettability of SiC with Al matrix has improved due to decrease in particle size. Pre-treatment of the reinforcements for improving wettability, together with multi-pass FSP, offers another alternative for uniform distribution of the very fine reinforcing particles in the FSP nugget zone [135,136]. These results show that the morphology of the tool and pass number plays an important role in the grain size of SZ.

4.3.3. Effect of number of passes on particle size

Fig. 4.9 presents the effect of pass number on the average particle size of FG samples produced by FSP. The average size of grain in base metal was approximately 34 μm in as-received condition and after processing the grain size reduced to 17 μm. In the FG samples, a fine equiaxed particles was obtained with a size ranging from 5.3 to 10.1 μm.

The primary process of grain refinement was through the occurrence of recrystallization and, subsequently, the grain growth hindered by the pinning action of the intermetallic particle. The particles serve as suitable sites to nucleate new grains through particulate stimulated

nucleation (PSN) during discontinuous dynamic recrystallization and then, the movement of the grain boundary is reduced by Zener pinning mechanism [137,138]. Therefore, two mechanisms contribute to achieving significant grain refinement during FSP.

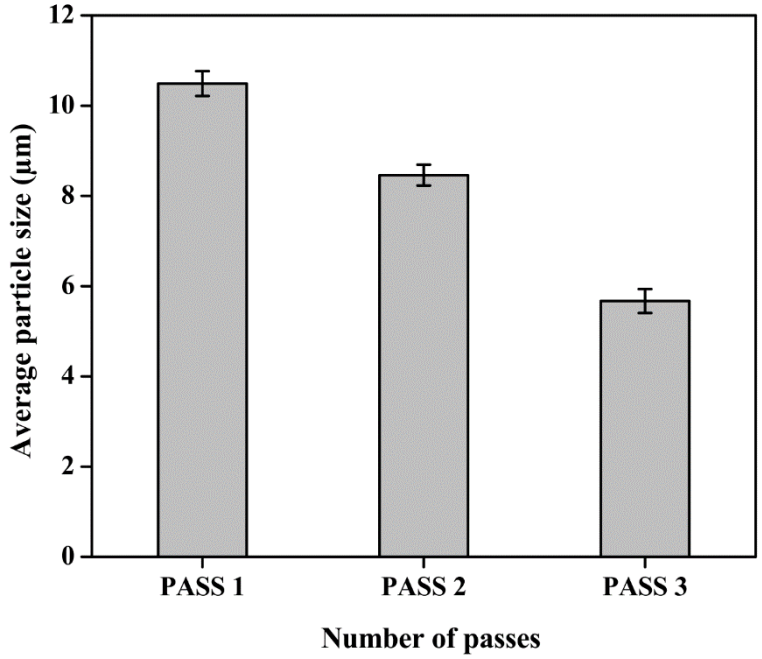

Fig. 4.10. Average particle size of FG composite as function of FSP pass number

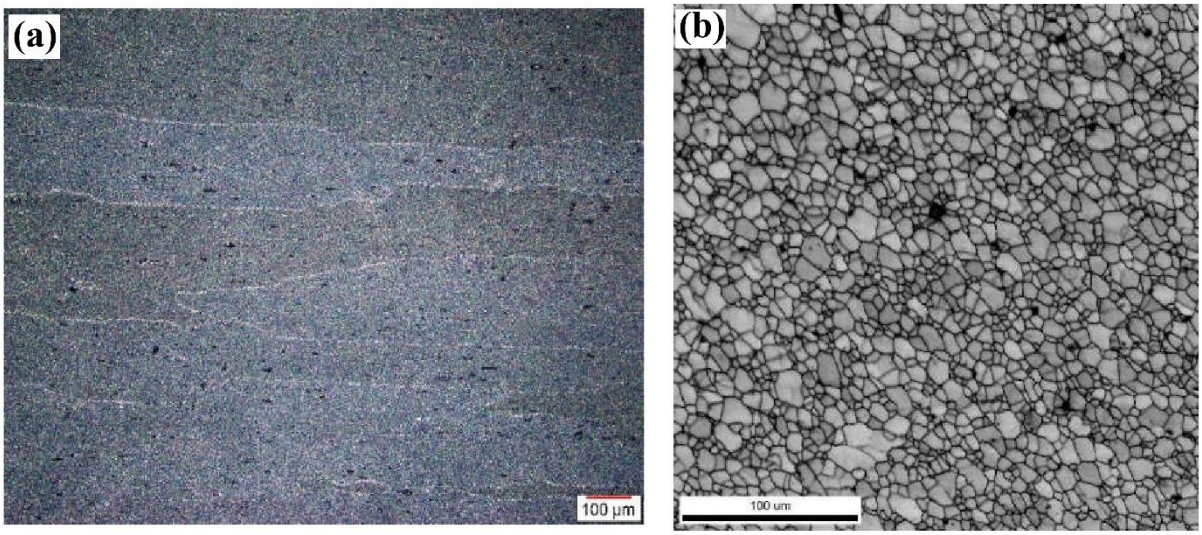

Fig. 4.11 Microstructures of base material (a) before processing (b) after processing

It is noteworthy that, increase in FSP passes results in refinement and homogenous dispersion of reinforcement particles in the stir zone [139]. However, FSP also has a major impact on grain growth due to the accumulation of heat in each FSP pass. It is hypothesized that threaded pins are also responsible in terms of temperature and effective flow of material around the tool [140].

In the first pass, the grains were fragmented to form fine grains with an average size of 10.11 µm and were severely broken by FSP into 8.13 µm (in the second pass). Thereby, in post two passes the grain size was refined to a size 3.5 times smaller than the actual grain size. It is evident that in the first and second passes, insufficient heat input and improper recrystallization caused the formation of coarser grains. However, it is clear that, in the third pass, due to sufficient plastic deformation in the SZ, finer grains can be obtained.

4.3.4. Microhardness

Fig. 4.10 depicts Vickers' hardness data with varied positions for FG samples along the direction of thickness from region-1 to region-3. The average microhardness value of 6082-Al (as-received material) was around 97 HV. The hardness was observed to decrease gradually along the direction of the gradient from the SiC-rich region (region-1) to the SiC lower region (region-3).

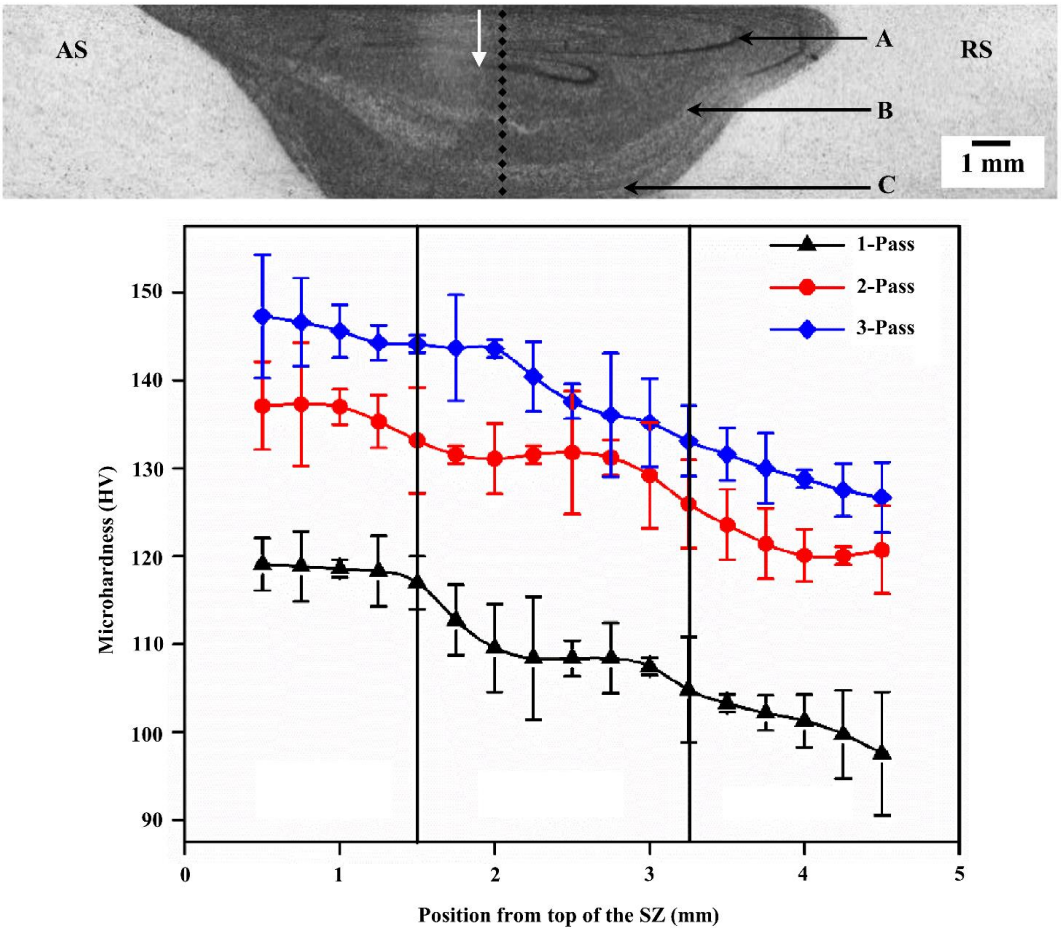

Fig. 4.12. Microhardness profiles of Al/SiC FG composite in transverse section of SZ for various passes **A:** SiC rich region (Region-1)**, B:** SiC moderate region (Region-2)**, C:** SiC lower region (Region-3)

It was interesting to observe that, the hardness values of FG samples increased proportionally with increasing addition of SiC particles. The FG composite surface layer (refer Fig. 10) in region-1 along the longitudinal direction containing 10 vol. % SiC displayed the highest value of microhardness of approximately 147 HV. This was found to be 1.5 times higher than that of as-received material (97 HV). In region-2 the microhardness of the FG composite surface layer contains 8 vol. % SiC was 137 HV, which was lower than region-1. The hardness values of 6 vol. % SiC in region-3 drastically reduced to 119 HV due to high inter-particle spacing, non-uniform dispersion of SiC particles and stirring of large grains.

The number of passes played a significant role in the micro-hardness results. It was found that the micro-hardness values were affected by the number of passes and improved by 13% (for pass-1), 15% (for pass-2), and 17% (for pass-3), respectively when compared to as-received material. In the first pass, the hardness value measured at the stir zone had increased from 97 HV to 119 HV because of induced development of strain and pinning effect of SiC particles. A further increase in the value of micro-hardness for the second pass was observed in the SZ of FG sample 137 HV because of a reduction in the size of the particles, leading to the distribution of particles and thus enhancing the hardness values. The third pass showed a higher hardness value of 147 HV because of the fine and uniform dispersion of SiC particles in the matrix. The micro-hardness results corroborated the microstructural observation in the SZ.

The improvement in the hardness can be attributed to grain size refinement which was caused due to dynamic recrystallization along with Orowan strengthening effect [141]. Due to the difference in thermal expansion coefficients between 6082-Al (matrix) and SiC (reinforcement), the dislocation density improved, causing an increase in the hardness. Therefore, hardness improvement on Al/SiC FG samples was caused by the number of passes, microstructural refinement and dispersion of SiC particles.

4.3.5. Wear analysis

The wear tracks of FG samples observed on the surface after dry sliding tests were analyzed using SEM as shown in Fig. 4.11. Fig. 4.12 indicates the graphical plots of the average wear rate with respect to the number of passes. The SiC particles are usually present over the surface and protect the matrix from functional contact with the counter body surface. Therefore, the interaction between the surfaces is mainly between the protruding SiC particles and the counter body surface, leading to a low wear rate. As mentioned in earlier section, the variables

which enhance the properties of FG composite decrease the wear rate. According to Archard's wear equation, the material hardness is inversely correlated to the wear rate i.e. wear rate decreases with an increase in hardness [142].

Fig. 4.11a presents the morphology of the worn-out surface of FG samples with one pass. In the initial wear stage, a small amount of material erodes from FG sample-A and accumulates on the counter surface. The wear mode here seems to be adhesive. On observing the worn surface, it was found to be non-uniform with grooves blended at the edges. The reason behind the formation of blended grooves was the presence of reinforcing particles. This, therefore, indicates the phenomena of abrasion. From the above results, it is clear that the wear mechanism on FG composite is an amalgamation of abrasive and adhesive wear modes.

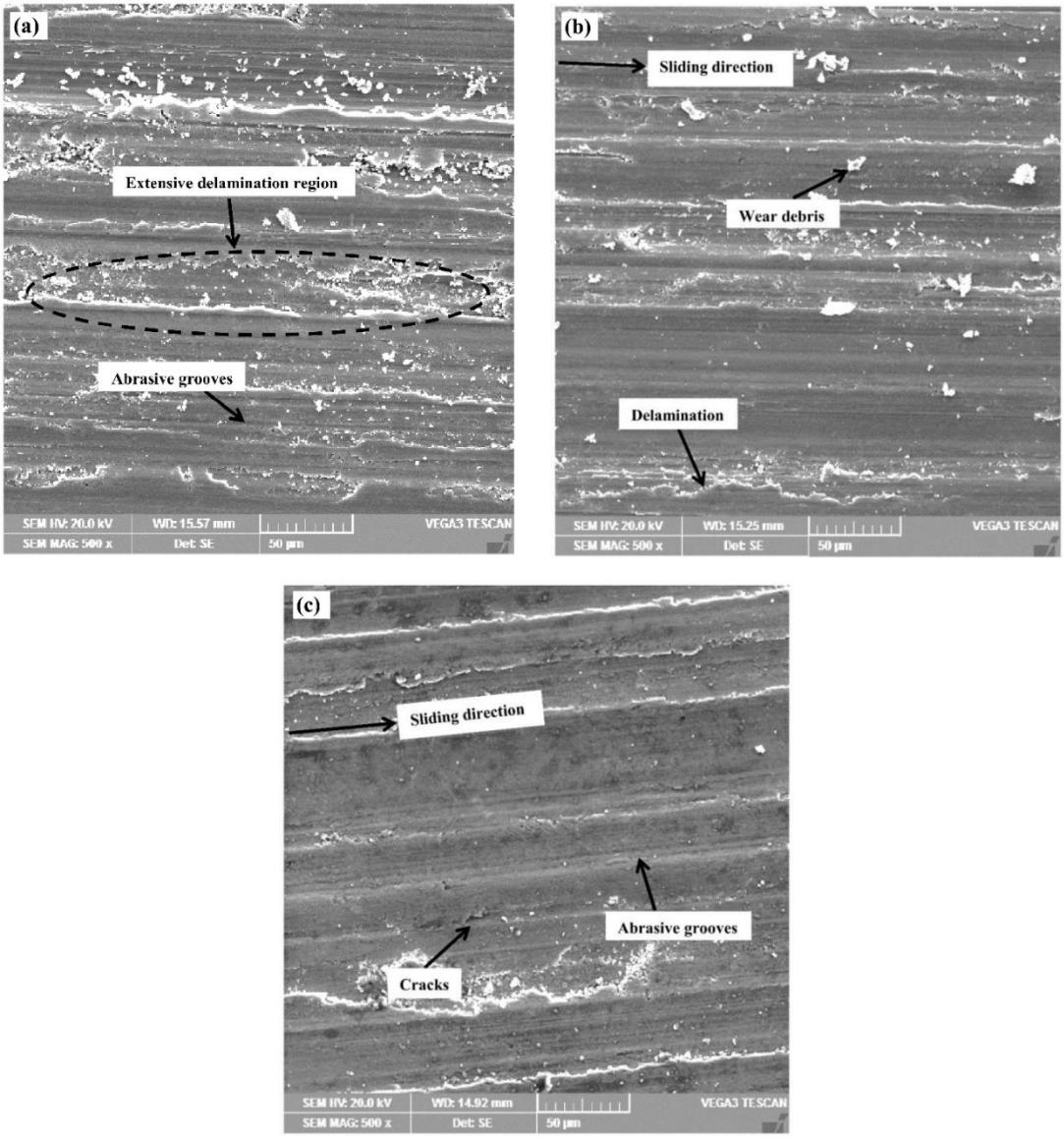

Fig. 4.13. SEM images of worn-out surface of Al/SiC FG composite layer fabricated by (a) one, (b) two, and (c) three FSP passes

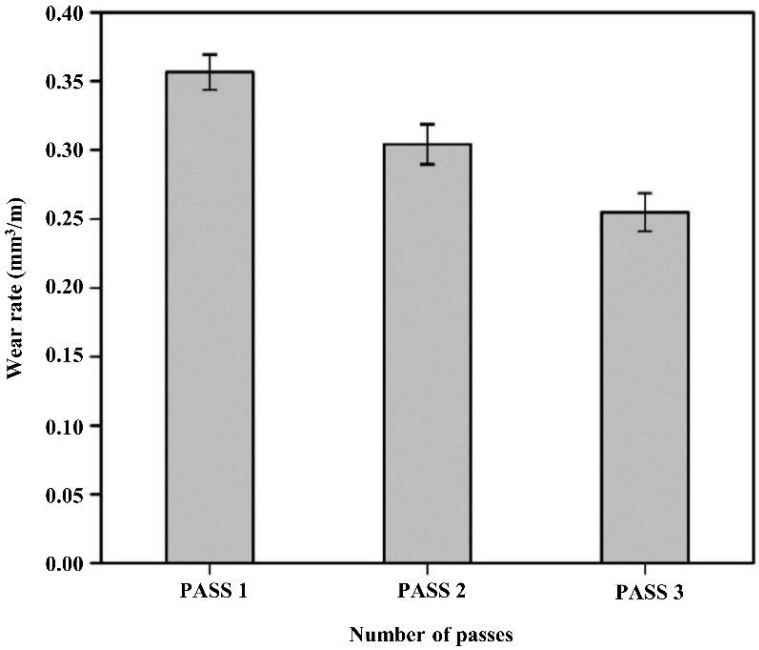

Fig. 4.14. Correlation between wear rate and FSP pass number for Al/SiC FG composite.

As shown in Fig. 4.11b, the width of wear track in the FG sample-B (two-pass) decreased compared to FG sample-A (one pass). It is evident that the wear rate in sample-B is lower than in sample-A. The wear track reveals that there are minor pits on the surface, mainly because of the local extraction of ceramic particles. The worn surface exhibits irregular delamination wear leading to a subsurface crack that grows progressively and eventually shears onto a surface forming a thin layer.

FG sample-C (third pass) with fine grooves and small delamination (refer Fig. 4.11c) recorded low wear rate compared to that of FG samples A and B. Table 4.3 shows the wear properties of FG samples at different pass numbers. A thorough evaluation of the microstructure of the worn surfaces can suggest that wear resistance of FG sample-C improved due to increase in hardness, homogenized distribution of SiC particles in the matrix and strong integration between matrix (aluminum alloy) and reinforcement particles (SiC).

Table 4.4 Wear properties of FG samples at different passes

Sample	No. of Passes	Wear rate (mm^3/m)			
		Trial-1	Trial-2	Trial-3	Average
A	1	0.3543	0.3345	0.3482	0.3456
B	2	0.3011	0.3201	0.2915	0.3042
C	3	0.2676	0.2532	0.2454	0.2554

4.4. Chapter summary

FSP was carried out with different pin lengths and different volume fractions of SiC particles. The resulted processed layer has a finer grain structure and a homogeneous precipitate distribution. The homogeneity of SiC particles through three FSP passes is achieved. This characteristic is related to the vigorous stirring action that the tool exerts on the particles. The increase in pass number affects the hardness of Al/SiC composite layer. The improved wear resistance was achieved by the addition of hard ceramics particles (SiC). The wear mechanism is a combination of abrasive and adhesive wear mode.

Chapter-5

Improvement of mechanical and corrosion properties of Al/SiC functionally graded material using a novel hybrid tool in friction stir processing

5.1. Introduction

In the present chapter, Al-SiC functionally graded materials (FGM) were produced via. friction stir processing (FSP) through a novel approach. The new approach involved a mathematical model for positioning holes in such a manner that the composition of the reinforcement (SiC) varied from maximum to minimum over a given length. The measurement of the reinforcement particle was determined by ratio between the volume of the hole and volume of the grid. The holes are drilled with a diameter of 2 mm on the plate according to developed mathematical model. These holes are filled with SiC reinforcement particles and sealed with pinless tool to avoid sputtering. Two tools with different pin profiles: conventional tool (CON) and hybrid tool (HYB), were employed for the process. The CON tool consisted of threads with zero flats while the HYB tool was a combination of threaded part and square (four flats) cross-section. The impact of pin profiles on the dispersion of SiC particles in the stir zone (SZ) of the processed specimens was studied.

5.2. Development of process model

Initially, a model was formulated to obtain maximum composition (K_{max}), followed by a gradual decrease along the direction of the tool and a minimum composition (K_{min}) at the end of FSP. The measurement of reinforcement particle composition (K_i) was determined by considering a hole (i) in the rectangular grid with a length of Z, in order to show the ratio between the volume of the hole and the volume of the grid, as depicted in Fig.5.1 where δl_i is grid length, D_p is the diameter of the tool pin and D is drilled hole diameter.

$$K_i = \frac{\pi \times D^2 \times L_p \times 100}{12 \times \delta l_i \times D_p \times L_p} \quad (1)$$

where L_p is the length of the pin that is equivalent to the depth of the hole. For a linear variation of volume fraction:

$$K_i = b - m \times l_i \quad (2)$$

Where $b = K_{max}$ and $m = \frac{K_{max} - K_{min}}{Z}$

Eq. (1) can be expressed as

$K_i = \frac{U}{\delta l_i}$ (3)

Where $U = \frac{\pi \times D^2 \times 100}{12 \times D_p}$

Equating Eq. (1) with Eq. (2) we get:

$\frac{U}{\delta l_i} = K_{max} - m \times l_i$ (4)

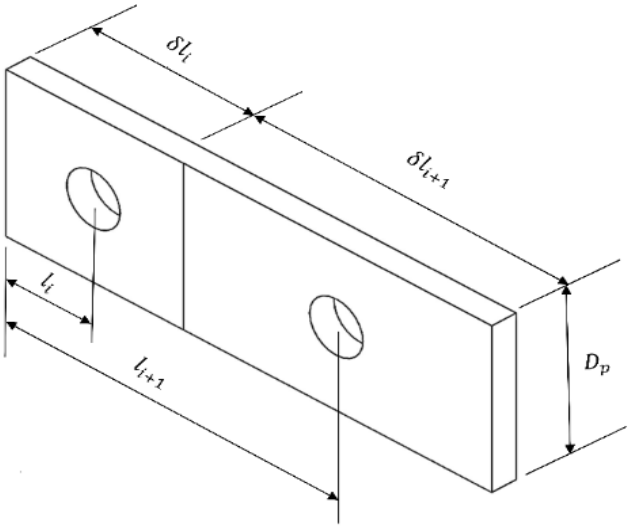

Fig. 5.1. Locating the hole for FG sample processing

From Fig.1

$l_{i+1} - l_i = \frac{\delta l_i}{2} + \frac{\delta l_{i+1}}{2}$ (5)

Substituting Eq. (2) in Eq. (5):

$K_i - K_{i+1} = \frac{m}{2} \times (\delta l_i + \delta l_{i+1})$ (6)

Using Eq. (3) in Eq. (6) and simplifying

$\delta {l_{i+1}}^2 + \delta l_{i+1} \times \left(\delta l_i - \frac{2U}{\delta l_i m}\right) + \frac{2U}{m} = 0$ (7)

Solving Eq. (7) for

$\delta l_{i+1} = \frac{\left(\frac{2U}{\delta l_i m} - \delta l_i\right) \pm \sqrt{\left(\left(\frac{2U}{\delta l_i m} - \delta l_i\right)^2 - \frac{8U}{m}\right)}}{2}$ (8)

Table 5.1 Length of the grid for different composition

Hole no. (i)	δl_i (mm)	K_i
1	2.18	8
2	2.24	7.7787
3	2.31	7.5509
4	2.38	7.3082
5	2.46	7.0655
6	2.55	6.8142
7	2.65	6.5533
8	2.77	6.2816
9	2.90	5.9976
10	3.05	5.6994
11	3.23	5.3847
12	3.44	5.0504
13	3.71	4.6923
14	4.04	4.3044
15	4.41	3.8776
16	5.12	3.3970
17	6.13	2.8341

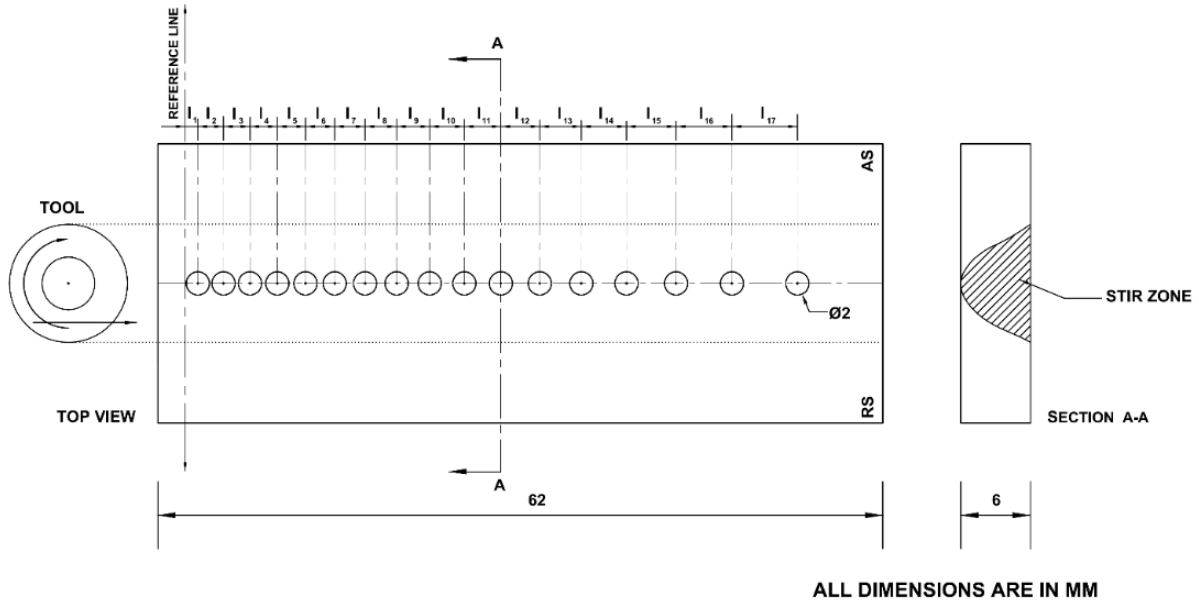

Fig. 5.2. Schematic diagram of holes illustrating minimum (K_{min}) to maximum composition (K_{max}) variation

The initial length of the grid was calculated for a fraction of known volume K_1 so that the corresponding lengths of the grid and position of the hole could be determined using Eq. (8) and (5) respectively. Fig.5.2 shows the schematic diagram of holes representing the change in composition from K_{min} to K_{max}. The FG samples were extracted from l_1 to l_{11} for examining mechanical properties. To prevent the overlap of holes, the volume of percentage was taken

from 3% (K_{min}) to 9% (K_{max}) for a length of Z= 60 mm (2 mm allowance for the reference line) respectively. As a result, the size of the grid varies, such that the proportion of reinforcement particles changes linearly.

5.3. Surface appearance and microstructure evaluation

Tool geometry as well as rotational and traveling speeds are important variables that play a vital role in improving the surface quality of processed samples. The visual appearance of FG samples processed using two different tools (i.e., CON and HYB) is illustrated in Fig.5.3. The surface of the processed region appeared to be free of defects such as cracks and scalloping. The FG sample fabricated by CON tool resulted in an uneven formation of ripples on the surface, which may be due to low shearing action and high frictional heating. On the other hand, the ripples were evenly spaced on the surface of the FG sample produced by HYB tool. This was due to the initial stage of plunging where the noncircular shaped pin profile enabled faster penetration into the surface plate. This was possible because of shearing action of the material induced by the edges and, also threads that caused more rotational transport of material [143]. It can be concluded that the formation of ripples on the surface was a function of traveling speed and tool profile.

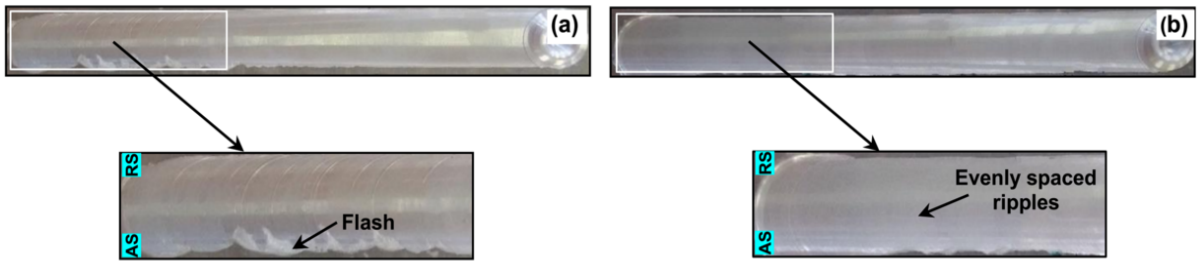

Fig. 5.3. Surface appearance of processed FG samples for (a) Conventional tool (b) Hybrid tool; **AS**: Advancing Side; **RS**: Retreating Side

The effect of pin profiles on the macro cross-section of the processed SZ is depicted in Fig.5.4. The FG sample fabricated by CON tool exhibited asymmetrical basin morphology in SZ (refer to Fig.5.4a). The SiC particles observed in the top, middle and bottom regions showed non-homogeneous distribution with particle agglomeration and coarser grains. The particles resulted in the formation of macro bands in upper and middle portion of the SZ, with the zones between these bands free from particles. The macro bands are the result of inadequate stirring action resulting in asymmetrical basin morphology.

Fig.5.4b illustrates a sample fabricated by HYB tool, which had preferential particle distribution of SiC particles with a change in concentration observed along the depth. The SZ exhibited symmetrical basin shape while the width of the SZ formed by HYB tool was larger than that of the CON tool. Due to the contact between the circumference and face edges of HYB tool pin with the base metal, a significant amount of heat was generated resulting in both friction and plastic deformation of the workpiece. Therefore, a large volume of plasticized material flowed around the tool pin surface, and in addition, the size of SZ formed with HYB tool pin was observed to be relatively larger than the SZ caused by CON tool pin. The distribution of SiC particles was classified into equiaxed and fine grain structures in all regions of SZ. Uniform deformation took place on both AS and RS of the FG sample processed with respect to HYB tool.

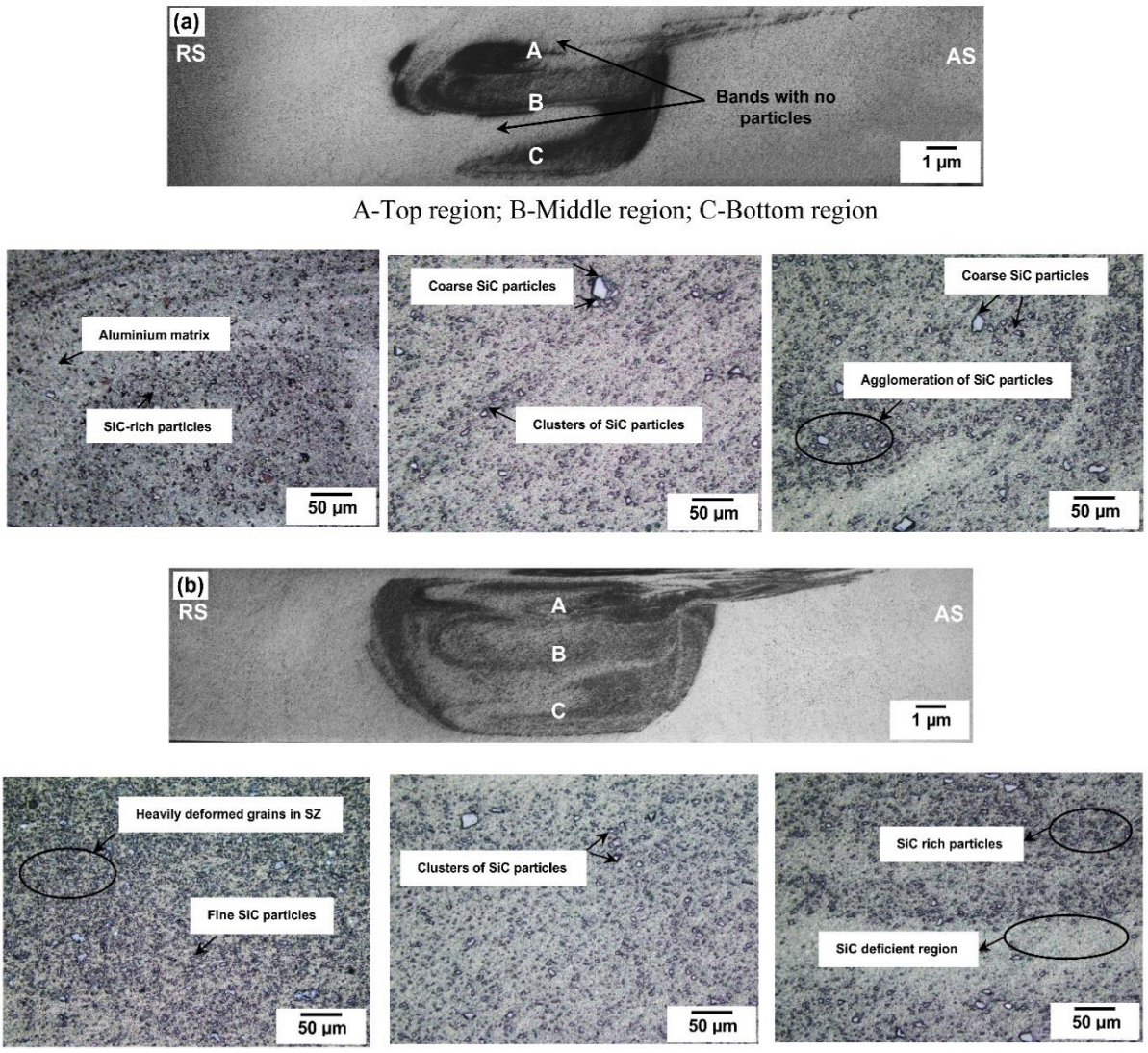

Fig. 5.4. Macrostructures of FG samples for (a) CON tool (b) HYB tool from top to bottom regions

A transition zone was observed between the top and middle region of SZ. In other words, the concentration of SiC changed drastically from top to middle region. The bottom region had a low volume fraction of SiC particles with a combination of coarse and fine grains. The homogeneity observed was due to the high rate of heat input and vigorous stirring action impelled by HYB tool. This indicated the combined effect of high frictional heat and pulsating action during processing [144]. The HYB pin profile had threads and 4 flat edges. Because of the edges in the flat surface of HYB pin profile tool, the material circulated in batches when the tool moved forward along the processed line.

In addition, due to the large contact surface of the threaded portion of the hybrid tool with the workpiece, high frictional heat was produced which in turn led to increased plastic deformation and enhanced the stirring of material [145]. In summary, the macro and microstructural analysis showed that the optimal balance of vertical transport and rotational transport of material was achieved with HYB tool.

5.4. XRD and SEM-EDAX analysis

Bragg's law gives relationship between distance of atomic planes in crystals and the angle of incidence at which those planes produce the most intense reflections of electromagnetic radiation. The equation of Bragg's law: $n\lambda = 2d \sin\theta$; where 'n' is an integer, 'd' is the distance, and 'λ' is the wavelength. It is used for determining wavelength and lattice spacings of crystals. XRD peaks are produced by constructive interference of a monochromatic X-ray beam scattered at certain angles from each set of lattice planes in a sample. The peak intensities are determined by the atomic positions within the lattice planes [146].

The XRD patterns obtained for BM and processed FG samples are shown in Fig.5.5. The scans were taken in 2θ range from 20° to 90°. The diffraction patterns of 2θ for Al showed peaks at 38.38, 44.61,78.01 and 82.20° which could be attributed to crystalline planes at (111), (002), (113), (222) respectively. The peaks recurred in the processed FG samples at the same spot. The presence of low-intensity Mg_2Si peaks in both FG and BM was detected. In addition to BM peaks, minor peaks of SiC were also observed in FG samples at 2θ = 44.76, 49.31, 57.59, 65.17, 72.30, 85.88 and 89.20° which could be tracked to the crystal planes (012), (112), (022), (013), (222), (004) and (014) respectively.

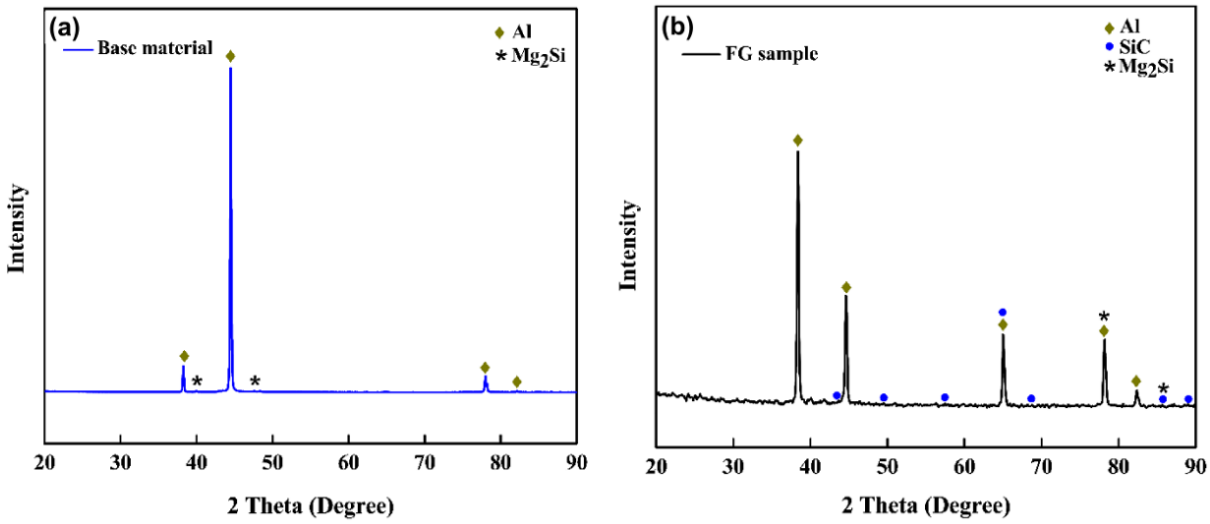

Fig. 5.5. XRD patterns of (a) BM and (b) FG sample fabricated with HYB tool

The XRD pattern of FG samples indicated that SiC particles were embedded into the matrix. It was further evident that no other complex intermetallic phases were detected in XRD after processing. The absence of other phases indicates that during processing, Mg_2Si precipitates remained stable and did not disintegrate into any other compound through transformation (as the FG samples peaks did not show any shifting of XRD peaks with SiC reinforcement). It can be concluded that no chemical change (chemical reaction) occurred between the SiC reinforcement and Al during FSP. This gives FSP an advantage over other processing methods such as powder metallurgy, laser beam and thermal spraying routes. In such processes, an increase in temperature above the melting point may result in the formation of various chemical compounds through the reaction of reinforcing particles, thereby adversely affecting the properties of the desired composite [147].

Fig.5.6 shows the SEM images of FG samples in different regions processed with CON and HYB tools. For the samples processed by CON tool, SiC particles clustered because of low plasticity and a restricted amount of material flow. The amount of heat produced between the workpiece and tool shoulder was inadequate to cause substantial flow of material around the pin. The samples produced using HYB tool showed gradient distribution of SiC particles with an absence of agglomeration in comparison with CON tool, where dispersion of SiC particles decreased in FG samples with a reduction in SiC concentration in the direction of thickness. In all regions of FG samples processed with HYB tool, coarse particles of SiC turned out to be fine particles due to strong interaction between the tool and the workpiece.

To figure out the dispersion of SiC particles it was required to calculate change in vol.% of different regions. This was accomplished by conducting phase volume fraction analysis with

SEM photomicrographs from different regions of an FG sample. Leica app suite 4.8 was employed for processing SEM photomicrographs illustrated in Fig.5.7. By comparing phase fractions of all the FG samples (processed with CON and HYB tool), it was discovered that FG sample processed with HYB tool had a uniform distribution of SiC particles compared to CON tool. From Table.5.1 it is evident that FG sample-HYB tool finely broke down SiC particles, with phase distribution of SiC on top, middle and bottom being 17.33±0.1, 13.23±0.2 and 7.64±0.3 vol.% respectively.

The peaks of Al, Si, C, Fe, O and Mg were confirmed by EDAX analysis, as illustrated in Fig.5.8. It also validates the distribution of SiC reinforcing particles within the matrix (aluminum). The formation of Mg_2Si intermetallic compound was verified and the findings matched XRD results. It was observed that SiC exists in the form of particles as well as layers. The densities of aluminum and SiC particles varied considerably. Due to the variations in densities, SiC particles tended to float on the surface

.

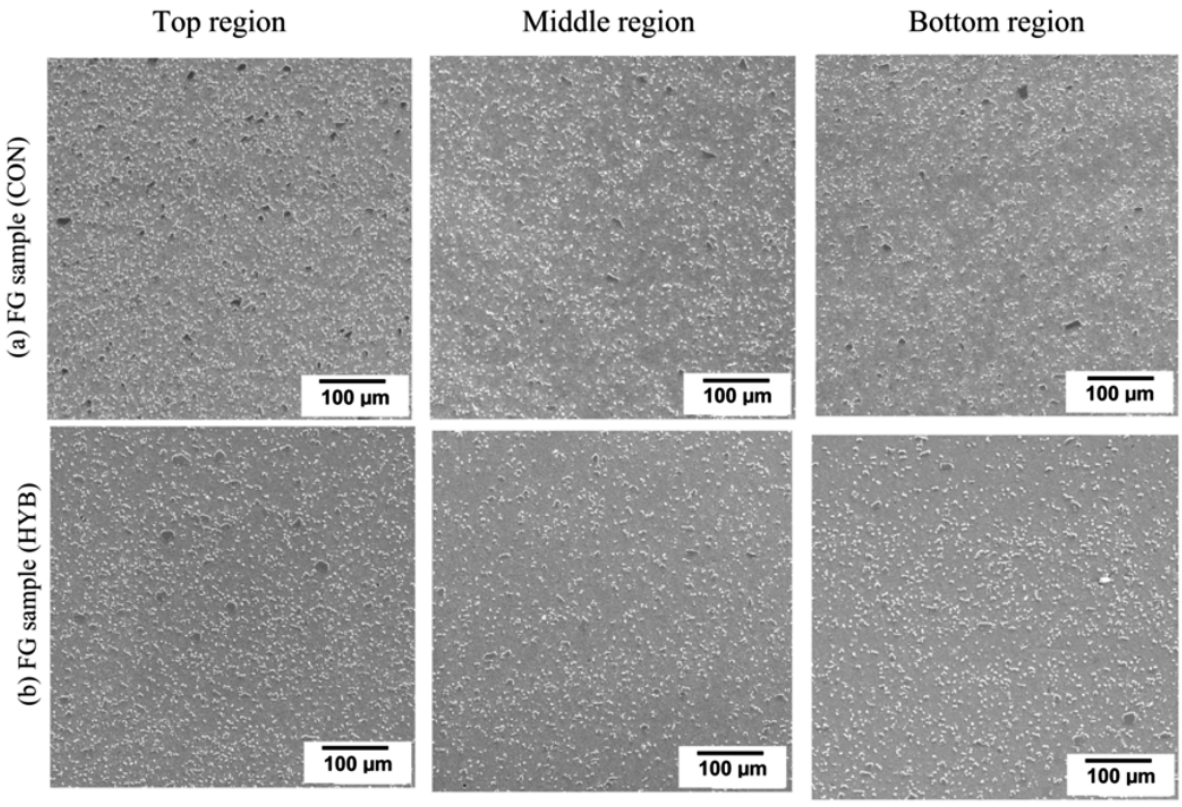

Fig. 5.6. SEM micrographs of FG samples processed with (a) CON tool (b) HYB tool at the top, middle and bottom regions

Table 5.2. Comparative determination of phase fraction in various regions of FG samples processed with different tools

Sample	Phase fraction summary at different regions					
	Top		Middle		Bottom	
	% Al alloy	% SiC	% Al alloy	% SiC	% Al alloy	% SiC
FG sample	86.64±0.4	13.36±0.4	88.53±0.1	11.47±0.2	90.79±0.4	9.21±0.1
FG sample	82.67±0.2	17.33±0.1	86.77±0.3	13.23±0.2	93.36±0.2	6.64±0.3

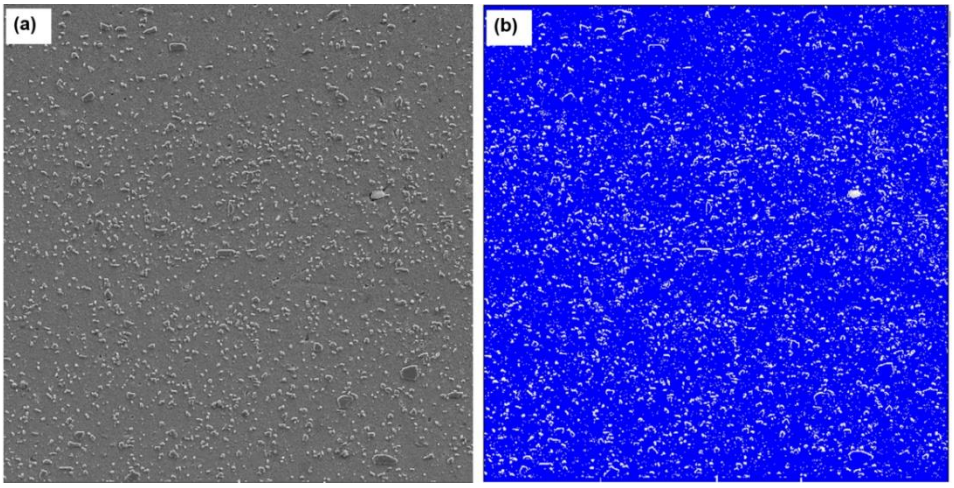

Fig. 5.7. Images taken while analysing phase fraction of FG sample (HYB) (a) Raw image in middle region (b) Processed image in middle region

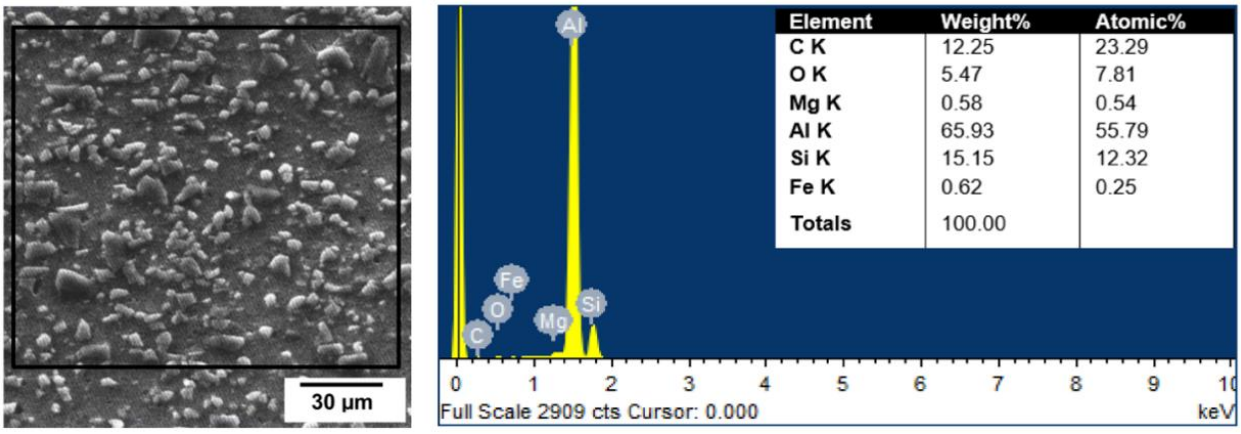

Fig. 5.8. Elemental composition of FG sample fabricated by HYB tool

5.5. Microhardness

Fig.5.9 depicts the microhardness distribution graph of FG samples fabricated with CON and HYB tools. The hardness was measured at the centre of the stir zone along the transverse section. The average measurement of hardness was taken from the maximum composition

(K_{max}) to the minimum composition (K_{min}) side. It is important to note that the hardness of FG samples decreased proportionally with a reduction in the volume fraction of SiC particles.

The average hardness of BM was observed to be 96 HV and it increased up to 140 HV. This phenomenon may be due to tool feature used during processing, grain size refinement or Orowan mechanism [148,149]. It was evident that the FG sample fabricated with HYB tool exhibited high microhardness values compared to CON tool. For HYB tool at the top region of SZ, the hardness value was observed to be 140 HV which is 1.2 times higher than the values obtained using CON tool. The higher hardness in the top region can be attributed to effective grain refinement and vigorous stirring of the tool. In the middle region, the hardness values were 129 HV which was slightly less than at the top region. Also, at the bottom region of the SZ, the hardness had gradually decreased to 119 HV which could be due to the presence of coarse grains, increase in interparticle spacing and non-uniform dispersion of particles.

The tool profile also played an influential role in determining microhardness. In HYB tool, in combination with vertical movement along the thread material and pulsating stir of flowing material and because of threads and flat faces, the total microhardness improved. The material flowed down to the end of the threaded part of the tool and was vigorously deformed through the flat edges of the square section of the tool owing to faster rate of heat generation. The dislocation density increased due to the coefficient of thermal expansion between matrix (6082-Al) and reinforcement (SiC) resulting in an increase in hardness [32, 33]. There was an absence of pulsating action in CON tool that led to inadequate stirring action and poor material flow required to produce finer grains in the SZ region. Therefore, the hardness of FG samples was influenced by tool profile which directly promoted efficient mixing of the material.

The increase in hardness values was attributed to fine grain fragmentation because of the presence of compressive strains in SZ and dynamic recrystallization by FSP. It was also apparent that in the center of the processed region (SZ), the reinforcing particles held the position of grain boundaries and were referred to as geometrically necessary dislocations (GNDs). The difference between the elastic modulus and thermal expansion coefficient resulted in the formation of GND. GNDs served as a barrier to the dislocation movement and contributed to increasing strength of the FG composite [152]. Thus, GNDs may have contributed to higher elastic modulus and hardness with reinforcements. In addition, the existence of SiC helped to enhance the hardness.

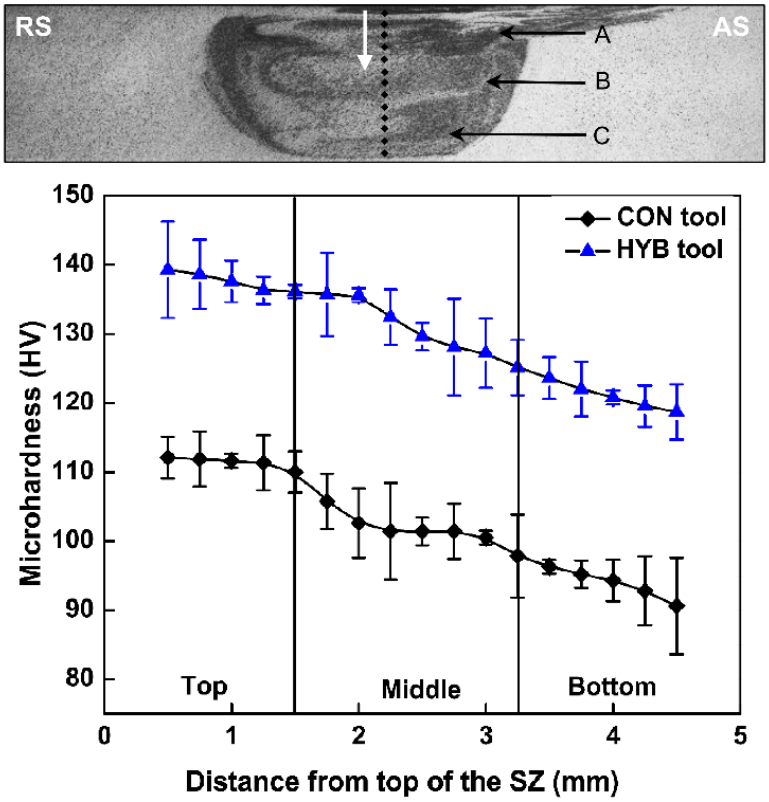

Fig. 5.9. Microhardness profiles of FG samples measured on a cross-section of SZ produced with different tools: A-Top region, B-Middle region, C-Bottom region

5.6. Wear analysis

The wear patterns corresponding to FG samples processed with CON and HYB tools are shown in Fig.5.10. The surface features were detected by SEM. The reinforcement particles (SiC) were generally present on the surface and shielded the matrix (Al alloy) from functional contact with the counterbody surface. As a result, the interaction between contacting surfaces was principally between the adhering SiC particles and counterbody surface, leading to inferior wear. Archard's law of wear provides the relation between wear rate ($mm^3.m^{-1}$) and hardness ($N.mm^{-2}$) of metallic materials i.e., higher hardness value of FG composite results in lower wear rate. This indicated that the increase in hardness value of FG composite increases the sliding wear resistance [142].

It can be seen from the table 5.2 that the average rate of the FG sample processed with HYB tool (0.25 $mm^3.m^{-1}$) was lower than that for the FG sample with CON tool (0.30 $mm^3.m^{-1}$). The HYB tool has preferential particle distribution of SiC particles due to pin profile the material is circulated in batches during processing that led to wear resistance. The CON tool resulted in formation of non-uniform distribution with coarser particles because of low shearing

action. The hardness has an influential role in improvement of wear rate of FG samples fabricated with HYB tool which directly promoted efficient mixing of the material.

The SEM images of worn surface of the sample processed with CON tool are presented in Fig.5.10(a). During the initial stage of wear, a finite amount of material was worn from the FG sample and collected on the counterbody surface. Frictional heat was generated during the sliding wear, inducing the material to plasticize. The plasticised FG sample was initially sticky to the counterbody surface and subsequently cleared as sliding action progressed. The wear mechanism here appears to be adhesive. The worn surface examined was revealed to be non-uniform with a significant sign of blended grooves on the edges. The formation of blended grooves was due to the existence of SiC particles. This indicates abrasion phenomenon. The above results clearly showed that the wear mechanism of the FG composite was a combination of adhesive and abrasive wear modes.

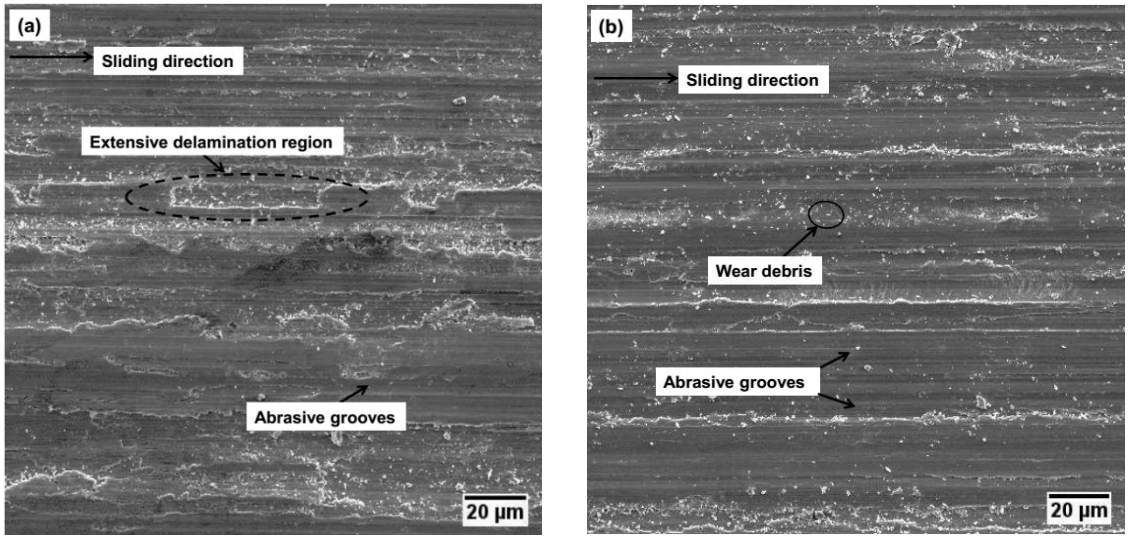

Fig. 5.10. Wear patterns of FG samples fabricated with (a) CON tool (b) HYB tool

Table 5.3 Average wear rates of FG samples processed with CON and HYB tools

Sample	Wear rate ($mm^3.m^{-1}$)			
	Trial-1	**Trial-2**	**Trial-3**	**Average**
FG sample (CON)	0.3353	0.3447	0.3256	0.3352
FG sample (HYB)	0.2632	0.2576	0.2554	0.2587

As detailed in Fig.5.10(b), the wear track width of the FG sample (HYB tool) decreased in comparison with FG sample (CON tool). The worn surfaces of FG sample (HYB) showed

flat surface and were clearly distinct from that of FG sample (CON). The average wear rates of FG samples obtained by processing with CON and HYB tools are illustrated in Table 5.2. It was clear that the average rate of wear in FG sample processed with HYB tool was lower than that for FG sample with CON tool. The worn surface area which showed features of parallel grooves, was a clear sign of abrasion wear mechanism. The worn surfaces were enveloped by wear debris that did not adhere because of the hard nature. The mode of wear had shifted from adhesion to abrasion. Craters were not observed on the worn surface owing to homogenized dispersion of reinforcing ceramic particles (SiC) in aluminium alloy (matrix). This mode of wear transfer was prominent for attaining a substantial improvement in the wear resistance of FG samples (HYB). A thorough assessment of the microstructural characterization of worn surfaces indicated that wear resistance of FG sample had enhanced because of uniform dispersion of reinforcing ceramic particles in the matrix with significant increase in hardness and strong interfacial bonding of reinforcing ceramic particles in the matrix.

5.7. Tensile properties

Different factors such as grain size, material flow, defects and reinforcement materials impact the tensile properties of processed samples. The tensile strength (UTS) of non-heat-treatable alloys is proportional to the size of the grain, i.e., when the size of the grain reduces, the values of UTS increase. However, for heat-treatable alloys like 6082-Al, UTS values are affected by Mg_2Si precipitates. The FG samples exhibit lower yield strength (YS) and UTS than BM due to precipitate coarsening in the heat-affected zone (HAZ). However, due to fine equiaxed grains in SZ, the elongation (EL) in the FG samples increased compared to BM. The inclusion of SiC particles in the SZ had a significant influence on tensile properties and also considerable effect on the hardness of SZ. The tensile properties of FG samples fabricated with CON and HYB tools are tabulated in Table 5.3. It can be observed that the FG sample (HYB) showed maximum tensile strength in comparison with FG sample processed with CON tool. The increase in tensile strength values of FG composite was attributed to a decrease in the size of the grain through Hall-Petch relation [153]. There was a decrease in the values of YS of FG samples compared to BM (i.e., 153 MPa for FG sample-CON tool and 190 MPa for FG sample-HYB tool). The product value of UTS and EL was maximum for the FG sample processed with HYB tool compared to BM.

Fig.5.11 depicts the stress-strain plots of the BM and FG samples. At least three samples of each condition were tested to ensure reproducibility of the tensile test. There was significant

non-linear behaviour for FG samples fabricated in both the tools before maximal stress was reached. Stress drop occurs because at the layer with high SiC mass fraction will fracture. Therefore, a drop in stress–strain curve will be observed. But, because of FG interface, stress will decrease gradually after stress drop. Also, a sudden drop in stress was noticed at the point of maximum stress, which led to the initiation of a crack in FG samples. The failure occurred between SZ and thermomechanical affected zone (TMAZ) on the RS for the samples fabricated via HYB tool and this was on account of the difference between the grains formed near SZ/TMAZ interface. The SZ was composed of fine equiaxed grains formed due to dynamic recrystallization, while TMAZ was composed of coarse elongated recovered grains. As a result, cracks were probably initiated in the interface region and were prone to tensile failure. For the CON tool, the failure occurred at the AS of the SZ owing to a decrease in thermal softening effect produced in TMAZ. This caused coarsening in the matrix precipitates, accumulation of dislocation networks and weak interaction between matrix (6082-Al) and reinforcement (SiC). Among the two FG samples produced, the FG sample processed with HYB tool showed an overall improvement of 6.03 % in UTS, 24.18 % in YS and 25% in EL with respect to the FG sample processed with CON tool. The Youngs Modulus of FG samples were analysed. The values are 61.58 GPa for base material, 29.62 GPa for FG sample (CON tool) and 53.91 for FG sample (HYB tool) respectively.

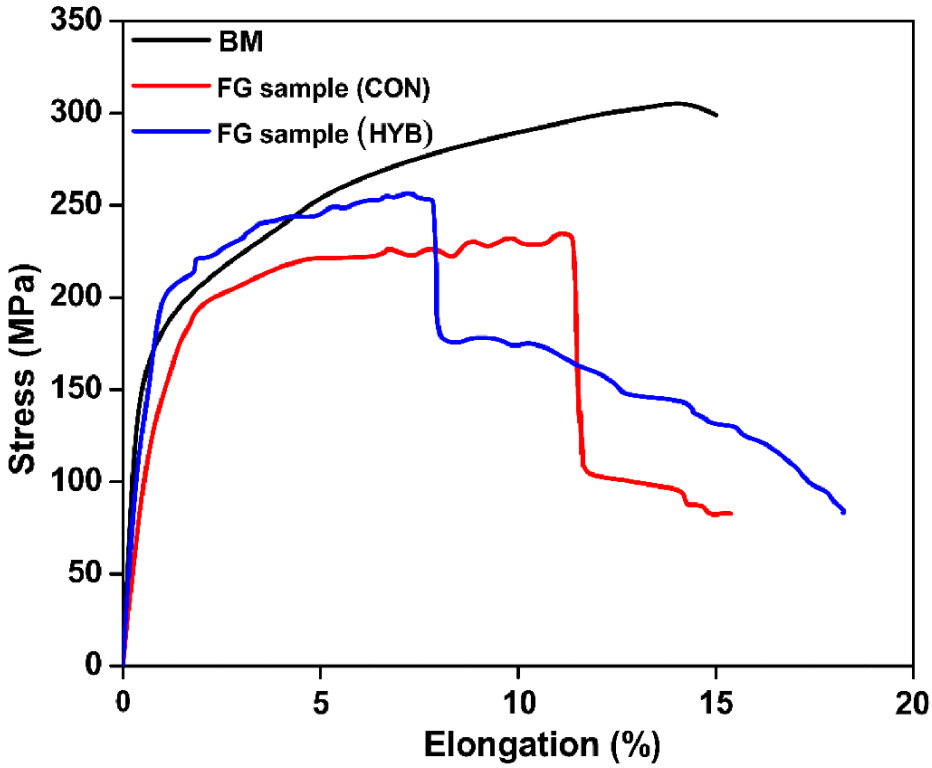

Fig. 5.11. Stress-strain plots of BM and FG samples

Table 5.4 Tensile properties of BM and FG samples

Sample	YS (MPa)	UTS (MPa)	EL (%)	UTS × EL (MPa%)
BM	236 ± 11	306 ± 07	13 ± 0.1	3978 ± 30
FG sample (CON)	153 ± 03	232 ± 05	16 ± 0.2	3712 ± 25
FG sample (HYB)	190 ± 06	246 ± 04	20 ± 0.5	4920 ± 35

The morphology of the fractured surfaces is illustrated in Fig.5.12. The BM showed deep and large dimples (~12 µm) on the fractured surface (refer Fig.5.12(a)) as a result of plastic deformation during testing. The fractured surface of the sample processed with CON tool exhibited high dimple density blended by varying shape and size of voids (~8 µm) which indicated that failure was related to ductile shear fracture detailed in Fig 5.12(b). In the case of the sample processed with HYB tool, the fracture surface as shown in Fig.5.12(c) had a high density of fine equiaxed dimples (~ 6 µm) with enhanced ductility, which was due to significant grain refinement and material flow. The existence of reinforcing particles in the wall and core of the dimples indicated that the clustered and weakened particles provided a suitable position for void growth/nucleation. However, the presence of reinforcing particles in the fracture region showed better interfacial bonding between the matrix and the reinforcement, thereby, effectively allowing load transfer between the soft matrix and the hard reinforcement.

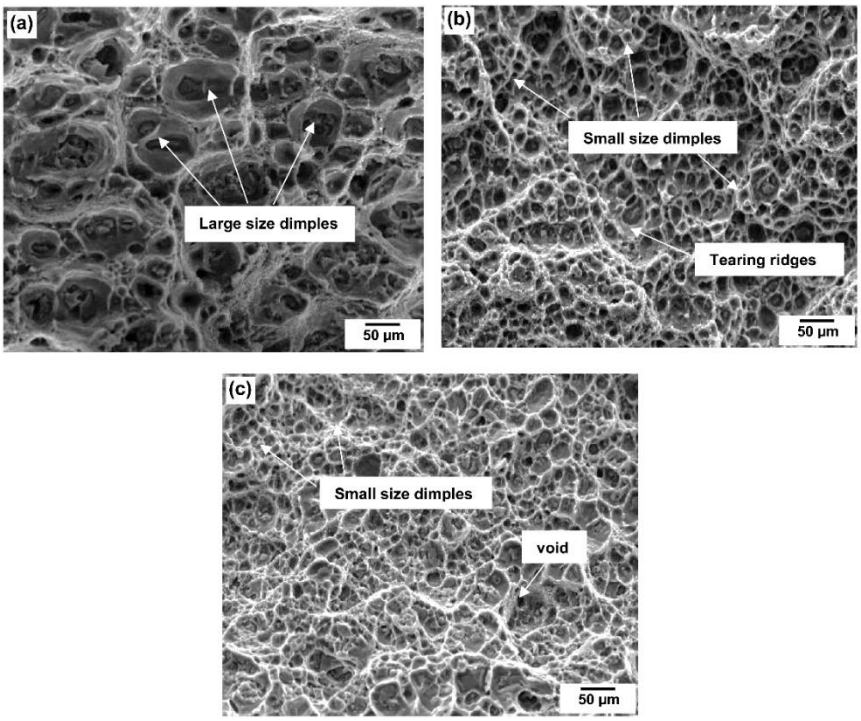

Fig. 5.12. SEM fracture micrographs of (a) BM (b) FG sample fabricated with CON tool and (c) FG sample fabricated with HYB tool

5.8. Corrosion analysis

Polarization tests were used to investigate the effect of the tool on corrosion behaviour of BM and FG samples in 3.5 wt% of NaCl solution. The Tafel curves of various samples are depicted in Fig.5.13. Curve (1) corresponds to the Tafel curve of BM alloy and the remaining two curves (2,3) correspond to the Tafel curve of FG samples fabricated with CON and HYB tool respectively.

The corrosion potential (E_{corr}) for each sample was determined using Tafel plots in Fig.5.13 and is listed in Table 5.4. The following conclusions may be reached from data in Table 4.7. In comparison with FG samples, BM had a more negative E_{corr} value and after FSP with HYB tool, the corrosion resistance of FG sample was found to be enhanced. This was mainly owing to intense plastic deformation and dynamic recrystallization phenomena in the process of FSP leading to microstructural homogenization. The homogenization of microstructure reduced the growth of galvanic corrosion, resulting in increased corrosion resistance [154]. Additionally, the corrosion resistance of FG samples was enhanced by the addition of SiC particles. The behaviour was due to the development of a weak galvanic couple between conductive matrix and nonconductive reinforcement (SiC), which impeded current flow and thus improved corrosion resistance [155].

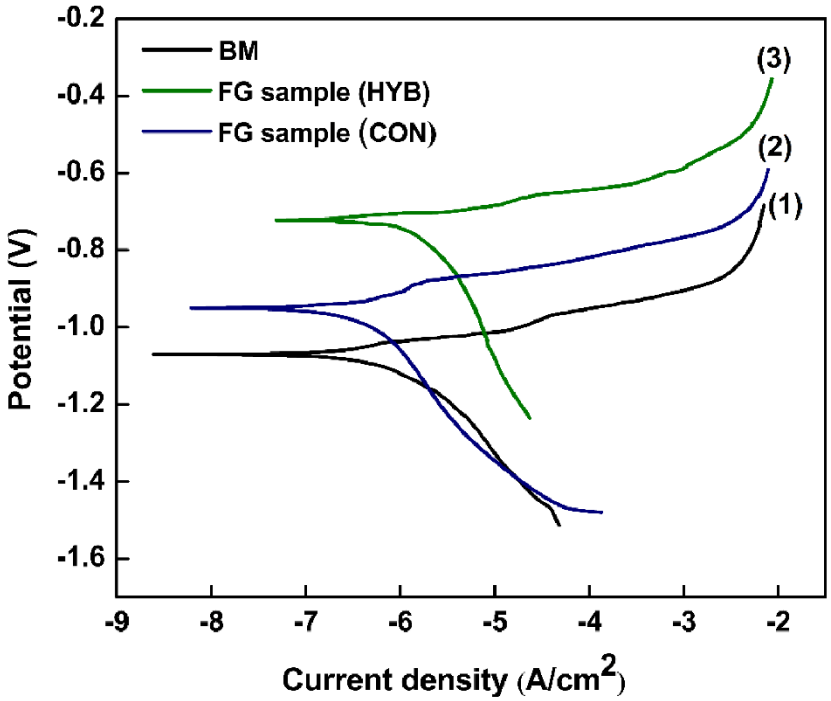

Fig. 5.13. Tafel plot depicting the corrosion behaviour of BM and FG samples

Fig.5.14 depicts the corrosion morphology on the top surface of the BM and FG samples processed with HYB and CON tool. The BM surface exhibited more localized corrosion on the

surface compared to FG samples. Fig.5.14(a) displays the corroded areas with severe pitting cavities on the surface of BM which was due to the activity of chloride ions. The sample processed with CON tool (refer to Fig.5.14(b)) was less resistant to corrosion than FG sample with HYB tool due to an increase in pits as well as wt % of SiC. The surface was exposed by the protrusion of large particles through the passive layer. The surface that was covered acted as cathode. Because of this, there was formation of a local galvanic couple between the uncovered surface and the covered surface, ultimately leading to an increase in the corrosion of the uncovered part of the surface [156].

Table 5.5 Corrosion potentials of BM and FG samples

Sample	BM	FG sample (CON)	FG sample (HYB)
E_{corr} (mV)	-1070	-950	-721

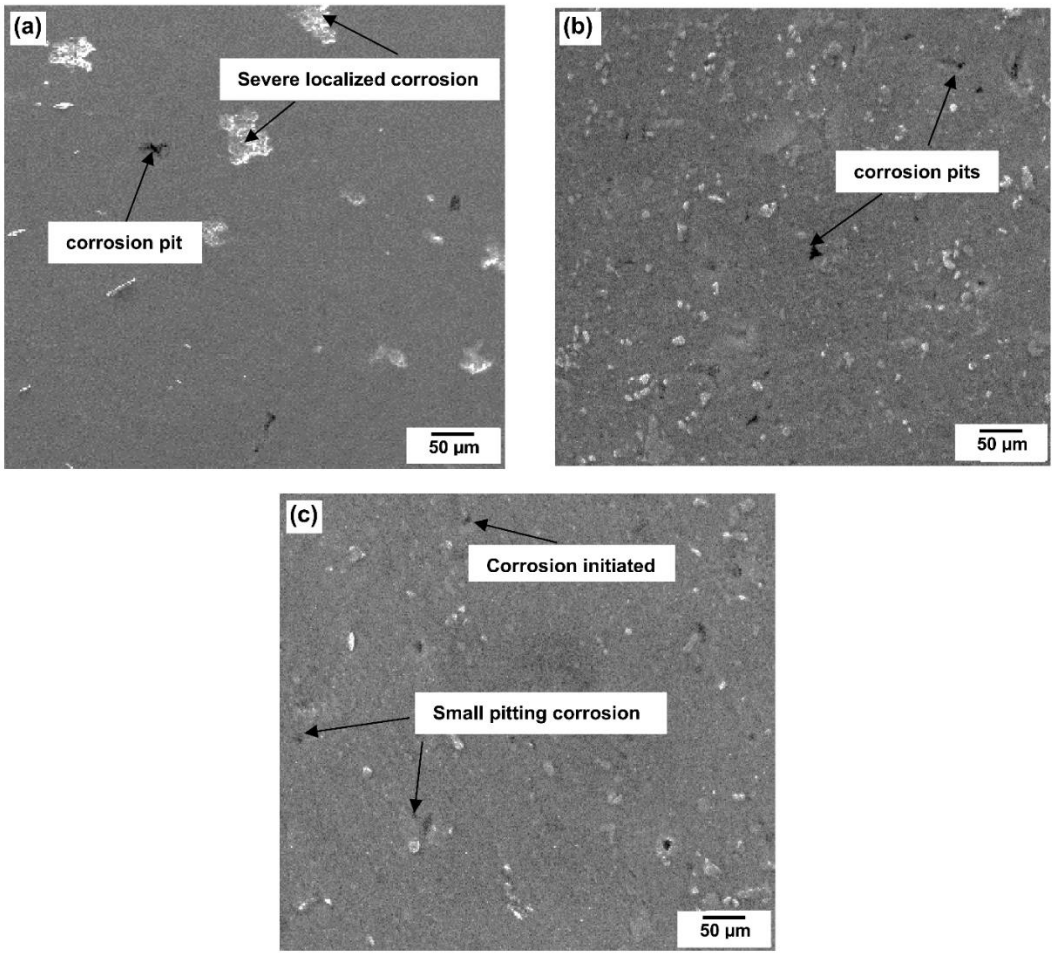

Fig. 5.14. SEM micrographs of corroded surfaces of (a) BM (b) FG sample fabricated with CON tool (c) FG sample fabricated with HYB tool

The FG sample fabricated with HYB tool showed superior corrosion resistance among the samples examined (refer to Fig 5.14 (c)). It was because of the selective dissolution of reinforcement particle-matrix interface that the localized corrosion protection of FG samples produced utilizing HYB tool was better than that achieved through BM and CON tool FG samples. This led to the formation of a crevice region formed by the coalescence of pits and voids around the particle. The crevice region in return acted as an anode and shielded the matrix material cathodically, thereby retarding further formation and propagation of pits.

5.9. EBSD analysis

EBSD analysis of FG samples processed using CON and HYB tools supported the presence of dynamic recrystallization. Fig.5.15 represents the grain boundary misorientation maps (GBM) and inverse pole figures (IPF) of FG samples at the centre of SZ produced with CON and HYB tools. After processing, both the samples showed elongated grain morphology which correlated with optical microstructural results. It was clear that the size of the grain had decreased with a change of tool profile (i.e., HYB tool which was a combination of threads and flat faces). Fig.5.16 shows the histograms for distribution of misorientation angle processed FG samples by different tools. With variation in tool geometry from CON to HYB tool, low angle misorientation fractions decreased from 0.5 to 0.32. This indicated dynamic recrystallization (DRX), owing to reduction in grain size and this influenced the mechanical properties (such as hardness and tensile strength). DRX phenomena is highly dependent on the amalgamation of temperature and strain in preference to the original grain size. The grain size in SZ depended on the amount of heat input generated by the tool, tool geometry and ratio of rotational speed to transverse speed of the tool. Due to change in tool direction, the average grain size of higher angle misorientation was around 6 µm and 4 µm for CON tool and HYB tool respectively. The change in tool direction partially recovered reinforcing particles that had moved from RS to AS in the earlier pass and as a result, they became more accessible in SZ. This increased the material flow and led to frictional heating. The results of EBSD such as low angle grain boundaries (LAGBs), high angle grain boundaries (HAGBs) and grain size of FG samples are listed in Table 5.5. LAGBs are marked by a green line for a misorientation of less than 15° while the misorientations greater than 15° are HAGBs marked by blue line.

The average size of the grains in SZ for FG samples fabricated with CON and HYB tools was 4.8 µm and 2.7 µm respectively. The reduction in grain size of FG samples (HYB) was because of the design of the tool (which is a combination of threads and flat faces) that enables

efficient use of deformation heat i.e., the ratio of static volume (pin volume) to dynamic volume (swept volume) impacted the degree of deformation in the material around the pin [157]. In the case of CON tool which consists of threads, the heat generation was entirely through friction between the adjacent material and tool; therefore, it took much time to produce heat and heat conduction in the unaffected material.

Table 5.6 Comparison of grain size and a fraction of grain boundaries of FG samples with CON and HYB tool

Sample	**Grain size (µm)**	**Fraction of grain boundaries (%)**	
		LAGBs	**HAGBs**
FG sample - CON	4.8	64	36
FG sample - HYB	2.7	49	51

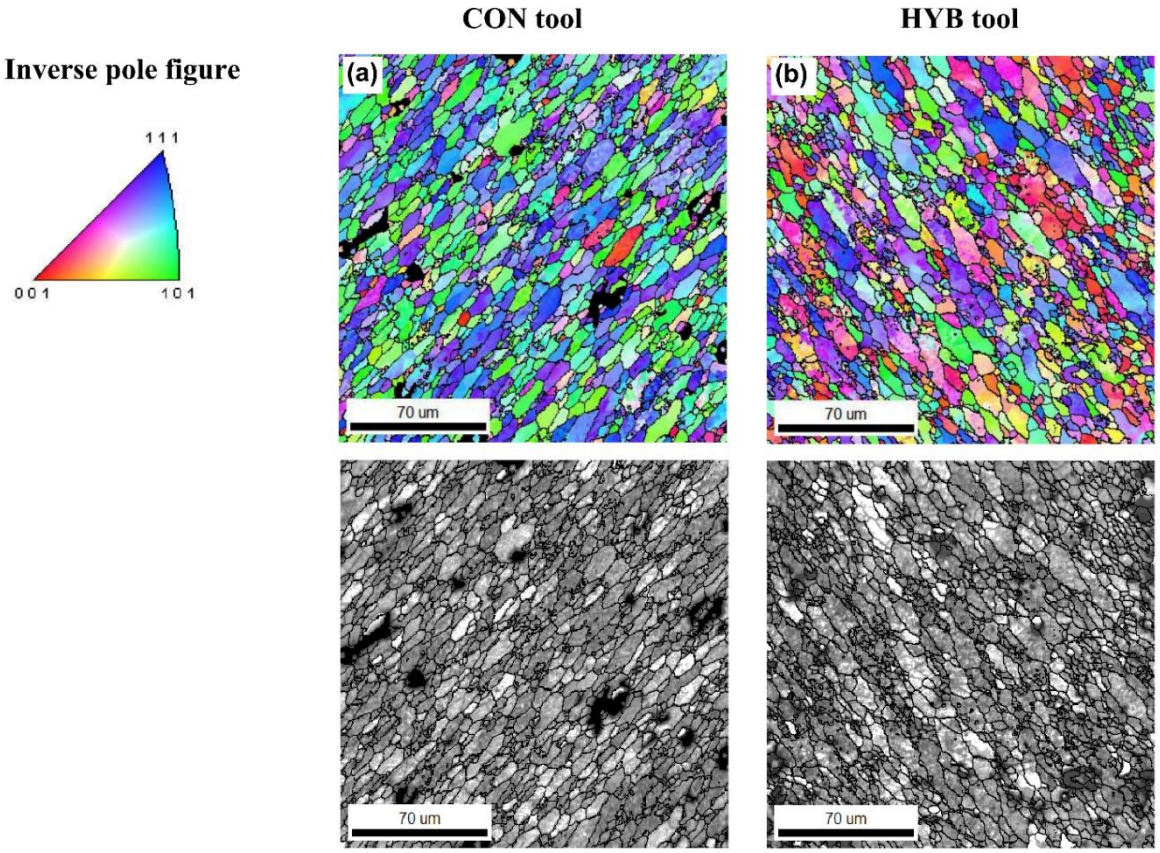

Fig. 5.15. EBSD images of FG samples fabricated with (a) CON tool (b) HYB tool

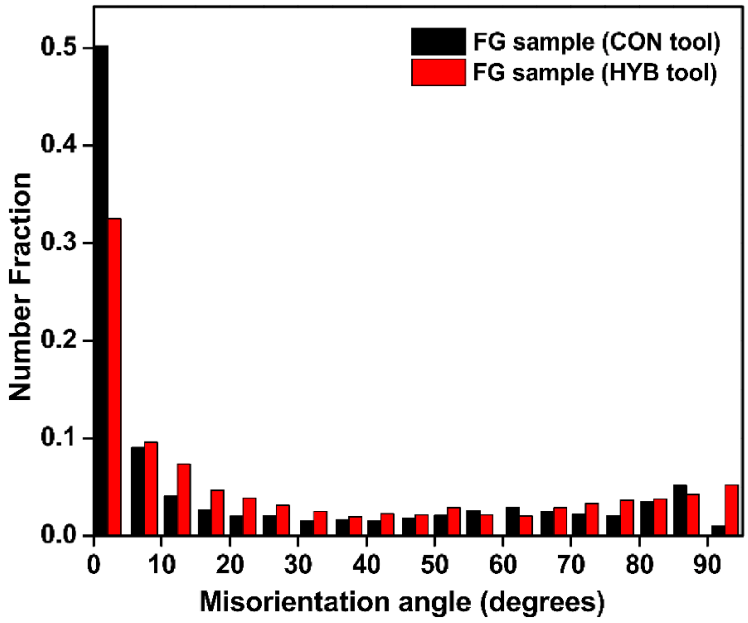

Fig. 5.16. Misorientation angle distribution in the FG samples fabricated with CON and HYB tool

5.10. Chapter summary

Reinforcement strategy was used as a mathematical model to control the volume of a given structure. This method provided an effective way to produce a customized Al/SiC graded structure. The microhardness increased while the tensile strength gradually decreased due to variations in the volume fraction of SiC. Gradual variation in the microstructure and grain size refinement also had an effect on the microhardness and tensile strength of Al/SiC FGMs. The addition of threads and flats to pin profiles (hybrid tool) aided material flow by expanding the range of orientation in both vertical and rotating directions. The processed FG samples subjected under tensile loading revealed that the primary cause of failure in both FGMs was SiC particle debonding with matrix deformation. In comparison to the sample fabricated by CON tool, the samples manufactured using HYB tool had the highest corrosion resistance. This could be owing to the presence of SiC particles on the surface, causing a weaker galvanic couple to form between the conductive matrix (BM) and the nonconductive reinforcement (SiC).

Chapter-6

Conclusions

6.1. Overall conclusions

The conclusions can be summarized as follows:

1 Novel Al/SiC functionally graded composites were successfully fabricated through friction stir processing. The number of passes, variation in pin length and % vol. of SiC showed substantial influence on the microstructure, microhardness and wear behavior. It was found that, varying SiC vol. % from 6 to 10 led to a graded structure. Al/SiC functionally graded composites yielded 5.34 µm grain size, 147 Hv microhardness and 0.25 mm^3/m wear rate based on these conditions.

2 The homogeneity in recirculation of SiC particles was found to be directly proportional to the number of FSP passes. Through three FSP passes, a homogenous distribution of SiC particles in aluminum alloy matrix with strong interfacial bonding was obtained.

3 In Al/SiC FG composite layer, it was observed that the grain size was inversely proportional to the FSP pass number. The grain size was reduced from 10.1 (in first pass) to 5.3 µm (in third pass). It is considered that the vigorous stirring action of the tool by SiC particles prevents the grain growth of DRX grains of the matrix.

4 The hardness of Al/SiC functionally graded composite layer increases significantly with an increase in pass number. The maximum microhardness obtained for FG composites is 147 Hv and as-received 6082-Al is 97 Hv, respectively. The increase in hardness of Al/SiC FG composite can also be attributed to grain size refinement. Dynamic recrystallization and Orowan strengthening effect are the factors that affect grain size refinement.

5 The Al/SiC FG composite processed with three FSP pass showed enhanced wear resistance compared to as-received Al, which was considerable due to the addition of hard ceramic particles (SiC) and increased hardness. Wear mechanism on FG composite is a combination of abrasive and adhesive wear modes.

6 The present reinforcement strategy provided an effective means to produce tailor-made Al/SiC FGMs by friction stir processing where the proportion of volume was controlled by a mathematical model that led to graded structure. The Al/SiC FGMs generated 140 Hv microhardness, 2.7 µm grain size, 25 % enhancement in elongation, 0.2587 $mm^3.m^{-1}$ in wear rate and -721 mV in corrosion potential (E_{cr}) based on the above-mentioned process conditions.

7 Due to variation in volume fraction of SiC, the microhardness increased while the tensile strength decreased gradually. The microhardness and tensile strength of Al/SiC FGMs were also affected by gradual variation in the microstructure and grain size refinement.

The Orowan strengthening effect and dynamic recrystallization were factors that affected the grain size refinement.

8 The introduction of threads and flats in pin profile (HYB tool) facilitated the flow of material by increasing the range of orientation both in vertical and rotating directions. Compared to FG samples produced by HYB tool, the samples produced by CON tool had coarser grains accompanied by agglomerated SiC particles.

9 The fractography study on FG samples tested under tensile load revealed that SiC particle debonding with matrix straining was the main cause of failure in both FGMs. Dimple shaped fracture surfaces were observed for all FG samples. However, the existence of SiC particles with uniform distribution led to the formation of smaller dimples (~6 μm).

10 The samples fabricated with HYB tool showed highest corrosion resistance (-721 mV) compared to BM and CON tool. This could be due to the presence of SiC particles at the surface and the formation of a weaker galvanic couple between the conductive matrix (BM) and nonconductive reinforcement (SiC).

6.2. Recommendations for future study

Based on the present research work, observations, analysis, and conclusions, the following may be recommended for future work.

1. The mathematical model may be expanded to parabolic alteration/modification in composition of 1-D FGMs and parabolic and linear alteration/modification in composition of 2-D and 3-D FGMs.
2. The effects of multi-pass FSP can be further studied with various process parameters by varying tool travel/transvers and spindle speed.
3. In the view of intensive wear, the concept of consumable tool could be investigated. Surface coatings produced by shoulder material adhesion or deep reinforcement from continuous pin feed can be possible solutions.
4. Future research may focus on new reinforcement approaches and the impact of process variables on FGMs.
5. The SiC/Al bond achieved by FSP is low, and it is advisable to use reinforcements with better affinity of the basic material. Therefore, a study may be carried out which investigates the role of reinforcements in base metals/ alloys.
6. In order to increase the homogeneity of particle distribution, multi-pass with complete overlapping should be examined.

References

[1] R. Li, Z. Li, Y. Zhu, L. Rong, A comparative study of laser beam welding and laser-MIG hybrid welding of Ti-Al-Zr-Fe titanium alloy, Mater. Sci. Eng. A. 528 (2011) 1138–1142. https://doi.org/10.1016/j.msea.2010.09.084.

[2] Y. Luo, J. Liu, H. Ye, Bubble flow and the formation of cavity defect in weld pool of vacuum electron beam welding, Vacuum. 86 (2011) 11–17. https://doi.org/10.1016/j.vacuum.2011.03.024.

[3] W.. Thomas, E.D. Nicholas, C. James, Friction welding, 5,460,317, 1995. https://doi.org/10.1093/tropej/14.1.3.

[4] W.M. Thomas, E.D. Nicholas, Friction stir welding for the transportation industries, Mater. Des. 18 (1997) 269–273. https://doi.org/10.1016/s0261-3069(97)00062-9.

[5] R. Nandan, T. DebRoy, H.K.D.H. Bhadeshia, Recent advances in friction-stir welding - Process, weldment structure and properties, Prog. Mater. Sci. 53 (2008) 980–1023. https://doi.org/10.1016/j.pmatsci.2008.05.001.

[6] Z.Y. Ma, Friction Stir Processing Technology : A Review, Metall. Mater. Trans. A. (2008). https://doi.org/10.1007/s11661-007-9459-0.

[7] L. Karthikeyan, V.S. Senthilkumar, V. Balasubramanian, S. Natarajan, Mechanical property and microstructural changes during friction stir processing of cast aluminum 2285 alloy, Mater. Des. 30 (2009) 2237–2242. https://doi.org/10.1016/j.matdes.2008.09.006.

[8] A. Meilinger, I. Torok, the Importance of Friction Stir Welding Tool, Prod. Process. Syst. 6 (2013) 25–34.

[9] G. Padmanaban, V. Balasubramanian, Selection of FSW tool pin profile, shoulder diameter and material for joining AZ31B magnesium alloy - An experimental approach, Mater. Des. 30 (2009) 2647–2656. https://doi.org/10.1016/j.matdes.2008.10.021.

[10] R. Mishra, Z.. Ma, Friction stir welding and processing, Mater. Sci. Eng. 50 (2005) 1–78. https://doi.org/10.1016/j.mser.2005.07.001.

[11] W.M. Thomas, K.I. Johnson, C.S. Wiesner, Friction stir welding-recent developments in tool and process technologies, Adv. Eng. Mater. 5 (2003) 485–490. https://doi.org/10.1002/adem.200300355.

[12] H.K. Mohanty, M.M. Mahapatra, P. Kumar, P. Biswas, N.R. Mandal, Effect of tool shoulder and pin probe profiles on friction stirred aluminum welds - a comparative study, J. Mar. Sci. Appl. 11 (2012) 200–207. https://doi.org/10.1007/s11804-012-1123-

4.

[13] R. Rai, A. De, H.K.D.H. Bhadeshia, T. DebRoy, Review: Friction stir welding tools, Sci. Technol. Weld. Join. 16 (2011) 325–342. https://doi.org/10.1179/1362171811Y.0000000023.

[14] O. Lorrain, V. Favier, H. Zahrouni, D. Lawrjaniec, Understanding the material flow path of friction stir welding process using unthreaded tools, J. Mater. Process. Technol. 210 (2010) 603–609. https://doi.org/10.1016/j.jmatprotec.2009.11.005.

[15] D.H. Choi, B.W. Ahn, C.Y. Lee, Y.M. Yeon, K. Song, Effect of pin shapes on joint characteristics of friction stir spot welded AA5J32 sheet, Mater. Trans. 51 (2010) 1028–1032. https://doi.org/10.2320/matertrans.M2009405.

[16] R.Z. Valiev, R.K. Islamgaliev, I. V. Alexandrov, Bulk nanostructured materials from severe plastic deformation, 2000. https://doi.org/10.1016/S0079-6425(99)00007-9.

[17] Y.H. Zhao, X.Z. Liao, Z. Jin, R.Z. Valiev, Y.T. Zhu, Microstructures and mechanical properties of ultrafine grained 7075 Al alloy processed by ECAP and their evolutions during annealing, Acta Mater. 52 (2004) 4589–4599. https://doi.org/10.1016/j.actamat.2004.06.017.

[18] Z.Y. Ma, S.R. Sharma, R.S. Mishra, Effect of multiple-pass friction stir processing on microstructure and tensile properties of a cast aluminum-silicon alloy, Scr. Mater. 54 (2006) 1623–1626. https://doi.org/10.1016/j.scriptamat.2006.01.010.

[19] L.B. Johannes, R.S. Mishra, Multiple passes of friction stir processing for the creation of superplastic 7075 aluminum, Mater. Sci. Eng. A. 464 (2007) 255–260. https://doi.org/10.1016/j.msea.2007.01.141.

[20] B.C. Liechty, B.W. Webb, Flow field characterization of friction stir processing using a particle-grid method, J. Mater. Process. Technol. 208 (2008) 431–443. https://doi.org/10.1016/j.jmatprotec.2008.01.008.

[21] A.P. Gerlich, Critical assessment: friction stir processing, potential, and problems, Mater. Sci. Technol. (United Kingdom). 33 (2017) 1139–1144. https://doi.org/10.1080/02670836.2017.1300420.

[22] N. Merah, M.A. Azeem, H.M. Abubaker, F. Al-Badour, J. Albinmousa, A.A. Sorour, Friction stir processing influence on microstructure, mechanical, and corrosion behavior of steels: A review, Materials (Basel). 14 (2021). https://doi.org/10.3390/ma14175023.

[23] D.H. Bowen, Overview of composite materials technology, (1988).

[24] B. Ralph, H.C. Yuen, W.B. Lee, The processing of metal matrix composites - An overview, J. Mater. Process. Technol. 63 (1997) 339–353.

https://doi.org/10.1016/S0924-0136(96)02645-3.

[25] J.M. Torralba, C.E. Da Costa, F. Velasco, P/M aluminum matrix composites: An overview, J. Mater. Process. Technol. 133 (2003) 203–206. https://doi.org/10.1016/S0924-0136(02)00234-0.

[26] N. Chawla, Metal-matrix composites in ground transportation Metal-Matrix Composites in Ground Transportation, (2016) 1–5. https://doi.org/10.1007/s11837-006-0231-5.

[27] D.K. Koli, G. Agnihotri, R. Purohit, Advanced Aluminium Matrix Composites: The Critical Need of Automotive and Aerospace Engineering Fields, Mater. Today Proc. 2 (2015) 3032–3041. https://doi.org/10.1016/j.matpr.2015.07.290.

[28] M. Dadkhah, M.H. Mosallanejad, L. Iuliano, A. Saboori, A Comprehensive Overview on the Latest Progress in the Additive Manufacturing of Metal Matrix Composites: Potential, Challenges, and Feasible Solutions, Acta Metall. Sin. (English Lett. 34 (2021) 1173–1200. https://doi.org/10.1007/s40195-021-01249-7.

[29] R. Narayanan, C. Saravanan, V. Krishnan, K. Subramanian, Effect of Particulate Reinforced Aluminium Metal Matrix Composite – A Review, Mech. Mech. Eng. 19 (2015) 23–30.

[30] K.S. Kumar, G. Bao, Intermetallic-matrix composites: An overview, Compos. Sci. Technol. 52 (1994) 127–150. https://doi.org/10.1016/0266-3538(94)90200-3.

[31] N.K. Bhoi, H. Singh, S. Pratap, Developments in the aluminum metal matrix composites reinforced by micro/nano particles – A review, J. Compos. Mater. 54 (2020) 813–833. https://doi.org/10.1177/0021998319865307.

[32] C.M. Friend, Toughness in metal matrix composites, Mater. Sci. Technol. (United Kingdom). 5 (1989) 1–7. https://doi.org/10.1179/mst.1989.5.1.1.

[33] S. V. Prasad, R. Asthana, Aluminum metal-matrix composites for automotive applications: Tribological considerations, Tribol. Lett. 17 (2004) 445–453. https://doi.org/10.1023/B:TRIL.0000044492.91991.f3.

[34] D.K. Jha, T. Kant, R.K. Singh, A critical review of recent research on functionally graded plates, Compos. Struct. 96 (2013) 833–849. https://doi.org/10.1016/j.compstruct.2012.09.001.

[35] D. Gayen, R. Tiwari, D. Chakraborty, Static and dynamic analyses of cracked functionally graded structural components: A review, Compos. Part B Eng. 173 (2019) 106982. https://doi.org/10.1016/j.compositesb.2019.106982.

[36] I.M. El-Galy, B.I. Saleh, M.H. Ahmed, Functionally graded materials classifications and development trends from industrial point of view, SN Appl. Sci. 1 (2019) 1–23.

https://doi.org/10.1007/s42452-019-1413-4.

[37] B.I. Saleh, M.H. Ahmed, Development of Functionally Graded Tubes Based on Pure Al/Al2O3 Metal Matrix Composites Manufactured by Centrifugal Casting for Automotive Applications, Met. Mater. Int. 26 (2019) 1430–1440. https://doi.org/10.1007/s12540-019-00391-3.

[38] J. Aboudi, M.J. Pindera, S.M. Arnold, Higher-order theory for functionally graded materials, Compos. Part B Eng. 30 (1999) 777–832. https://doi.org/10.1016/S1359-8368(99)00053-0.

[39] F. Ghadami, A. Sabour Rouh Aghdam, S. Ghadami, Preparation, characterization and oxidation behavior of CeO2-gradient NiCrAlY coatings applied by HVOF thermal spraying process, Ceram. Int. 46 (2020) 20500–20509. https://doi.org/10.1016/j.ceramint.2020.05.155.

[40] B. Saleh, J. Jiang, A. Ma, D. Song, D. Yang, Effect of Main Parameters on the Mechanical and Wear Behaviour of Functionally Graded Materials by Centrifugal Casting: A Review, Met. Mater. Int. 25 (2019) 1395–1409. https://doi.org/10.1007/s12540-019-00273-8.

[41] X. Zhang, L. Guo, F. Yang, A.A. Volinsky, M. Hostetter, Z. Guo, 3D gel printing of graded TiC-high manganese steel cermet, J. Mater. Sci. 54 (2019) 2122–2132. https://doi.org/10.1007/s10853-018-2945-5.

[42] M.S. Surya, G. Prasanthi, Effect of Silicon Carbide Weight Percentage and Number of Layers on Microstructural and Mechanical Properties of Al7075/SiC Functionally Graded Material, Silicon. (2021). https://doi.org/10.1007/s12633-020-00865-9.

[43] H. Zhou, Z. Wang, B. Wang, Fabrication of WC-Co/(Ti, W)C graded cemented carbide by spark plasma sintering, Int. J. Refract. Met. Hard Mater. 87 (2020) 105141. https://doi.org/10.1016/j.ijrmhm.2019.105141.

[44] C. Zhang, F. Chen, Z. Huang, M. Jia, G. Chen, Y. Ye, Y. Lin, W. Liu, B. Chen, Q. Shen, L. Zhang, E.J. Lavernia, Additive manufacturing of functionally graded materials: A review, Mater. Sci. Eng. A. 764 (2019) 138209. https://doi.org/10.1016/j.msea.2019.138209.

[45] S. Rathee, S. Maheshwari, A.N. Siddiquee, Issues and strategies in composite fabrication via friction stir processing : A review, Mater. Manuf. Process. 33 (2018) 239–261. https://doi.org/10.1080/10426914.2017.1303162.

[46] B. Vasić, U. Ralević, K. Cvetanović Zobenica, M. M. Smiljanić, R. Gajić, M. Spasenović, S. Vollebregt, Low-friction, wear-resistant, and electrically homogeneous

multilayer graphene grown by chemical vapor deposition on molybdenum, Appl. Surf. Sci. 509 (2020). https://doi.org/10.1016/j.apsusc.2019.144792.

[47] C. Contatori, N.I. Domingues, R.L. Barreto, N.B. de Lima, J. Vatavuk, A.A.C. Borges, G.F.C. Almeida, A.A. Couto, Effect of Mg and Cu on microstructure, hardness and wear on functionally graded Al–19Si alloy prepared by centrifugal casting, J. Mater. Res. Technol. 9 (2020) 15862–15873. https://doi.org/10.1016/j.jmrt.2020.11.050.

[48] A. Amherd Hidalgo, R. Frykholm, T. Ebel, F. Pyczak, Powder Metallurgy Strategies to Improve Properties and Processing of Titanium Alloys: A Review, Adv. Eng. Mater. 19 (2017) 1–14. https://doi.org/10.1002/adem.201600743.

[49] G.H. Loh, E. Pei, D. Harrison, M.D. Monzón, An overview of functionally graded additive manufacturing, Addit. Manuf. 23 (2018) 34–44. https://doi.org/10.1016/j.addma.2018.06.023.

[50] F. Khodabakhshi, A.P. Gerlich, Potentials and strategies of solid-state additive friction-stir manufacturing technology: A critical review, J. Manuf. Process. 36 (2018) 77–92. https://doi.org/10.1016/j.jmapro.2018.09.030.

[51] M.S. Węglowski, Friction stir processing – State of the art, Arch. Civ. Mech. Eng. 18 (2018) 114–129. https://doi.org/10.1016/j.acme.2017.06.002.

[52] W. Wang, P. Han, P. Peng, T. Zhang, Q. Liu, S.N. Yuan, L.Y. Huang, H.L. Yu, K. Qiao, K.S. Wang, Friction Stir Processing of Magnesium Alloys: A Review, Acta Metall. Sin. (English Lett. 33 (2020) 43–57. https://doi.org/10.1007/s40195-019-00971-7.

[53] B. Saleh, J. Jiang, R. Fathi, T. Al-hababi, Q. Xu, L. Wang, D. Song, A. Ma, 30 Years of functionally graded materials: An overview of manufacturing methods, Applications and Future Challenges, Compos. Part B Eng. 201 (2020) 108376. https://doi.org/10.1016/j.compositesb.2020.108376.

[54] M. Naebe, K. Shirvanimoghaddam, Functionally graded materials : A review of fabrication and properties, Appl. Mater. Today. 5 (2016) 223–245. https://doi.org/10.1016/j.apmt.2016.10.001.

[55] S. Zherebtsov, I.P. Semenova, H. Garbacz, M. Motyka, Advanced mechanical properties, Elsevier Inc., 2018. https://doi.org/10.1016/B978-0-12-814599-9.00006-7.

[56] A. Sharma, V. Bandari, K. Ito, K. Kohama, R.M. Ramji, H.S. Himasekhar, A new process for design and manufacture of tailor-made functionally graded composites through friction stir additive manufacturing, J. Manuf. Process. 26 (2017) 122–130. https://doi.org/10.1016/j.jmapro.2017.02.007.

[57] C.J. Hsu, C.Y. Chang, P.W. Kao, N.J. Ho, C.P. Chang, Al-Al3Ti nanocomposites

produced in situ by friction stir processing, Acta Mater. 54 (2006) 5241–5249. https://doi.org/10.1016/j.actamat.2006.06.054.

[58] P.J. Haagensen, O.T. Midlin, M.Rane, Fatigue performance of friction stir butt welds in a 6000 series aluminum allo, Comput. Methods Exp. Meas. Surf. Treat. Eff. II. 8 (1995) 589–598. http://www.emeraldinsight.com/doi/10.1108/01439910410512000.

[59] G. Liu, L.E. Murr, C.S. Niou, J.C. McClure, F.R. Vega, Microstructural aspects of the friction-stir welding of 6061-T6 aluminum, Scr. Mater. 37 (1997) 355–361. https://doi.org/10.1016/S1359-6462(97)00093-6.

[60] C.G. Rhodes, M.W. Mahoney, W.H. Bingel, M. Calabrese, Fine-grain evolution in friction-stir processed 7050 aluminum, Scr. Mater. 48 (2003) 1451–1455. https://doi.org/10.1016/S1359-6462(03)00082-4.

[61] K.V. Jata, S.L. Semiatin, Recrystallization during friction stir welding of high strength aluminium alloys, Scr. Mater. 43 (2000) 743–749.

[62] R.A. Prado, L.E. Murr, K.F. Soto, J.C. McClure, Self-optimization in tool wear for friction-stir welding of Al 6061+20% Al2O3 MMC, Mater. Sci. Eng. A. 349 (2003) 156–165. https://doi.org/10.1016/S0921-5093(02)00750-5.

[63] P.S. Pao, S.J. Gill, C.R. Feng, K.K. Sankaran, Corrosion-fatigue crack growth in friction stir welded Al 7050, Scr. Mater. 45 (2001) 605–612. https://doi.org/10.1016/S1359-6462(01)01070-3.

[64] Y.S. Sato, M. Urata, H. Kokawa, K. Ikeda, M. Enomoto, Retention of fine grained microstructure of equal channel angular pressed aluminum alloy 1050 by friction stir welding, Scr. Mater. 45 (2001) 109–114. https://doi.org/10.1016/S1359-6462(01)01000-4.

[65] P.B. Berbon, W.H. Bingel, R.S. Mishra, C.C. Bampton, M.W. Mahoney, Friction stir processing: A tool to homogenize nanocomposite aluminum alloys, Scr. Mater. 44 (2001) 61–66. https://doi.org/10.1016/S1359-6462(00)00578-9.

[66] Y.J. Kwon, I. Shigematsu, N. Saito, Mechanical properties of fine-grained aluminum alloy produced by friction stir process, Scr. Mater. 49 (2003) 785–789. https://doi.org/10.1016/S1359-6462(03)00407-X.

[67] C.H. Chuang, J.C. Huang, P.J. Hsieh, Using friction stir processing to fabricate MgAlZn intermetallic alloys, Scr. Mater. 53 (2005) 1455–1460. https://doi.org/10.1016/j.scriptamat.2005.08.019.

[68] J.Q. Su, T.W. Nelson, C.J. Sterling, Friction stir processing of large-area bulk UFG aluminum alloys, Scr. Mater. 52 (2005) 135–140.

https://doi.org/10.1016/j.scriptamat.2004.09.014.

[69] M.L. Santella, T. Engstrom, D. Storjohann, T.Y. Pan, Effects of friction stir processing on mechanical properties of the cast aluminum alloys A319 and A356, Scr. Mater. 53 (2005) 201–206. https://doi.org/10.1016/j.scriptamat.2005.03.040.

[70] I. Charit, R.S. Mishra, Low temperature superplasticity in a friction-stir-processed ultrafine grained Al-Zn-Mg-Sc alloy, Acta Mater. 53 (2005) 4211–4223. https://doi.org/10.1016/j.actamat.2005.05.021.

[71] Y. Morisada, H. Fujii, T. Nagaoka, M. Fukusumi, MWCNTs/AZ31 surface composites fabricated by friction stir processing, Mater. Sci. Eng. A. 419 (2006) 344–348. https://doi.org/10.1016/j.msea.2006.01.016.

[72] K. Nakata, Y.G. Kim, H. Fujii, T. Tsumura, T. Komazaki, Improvement of mechanical properties of aluminum die casting alloy by multi-pass friction stir processing, Mater. Sci. Eng. A. 437 (2006) 274–280. https://doi.org/10.1016/j.msea.2006.07.150.

[73] D.C. Hofmann, K.S. Vecchio, Submerged friction stir processing (SFSP): An improved method for creating ultra-fine-grained bulk materials, Mater. Sci. Eng. A. 402 (2005) 234–241. https://doi.org/10.1016/j.msea.2005.04.032.

[74] I. Charit, R.S. Mishra, High strain rate superplasticity in a commercial 2024 Al alloy via friction stir processing, Mater. Sci. Eng. A. 359 (2003) 290–296. https://doi.org/10.1016/S0921-5093(03)00367-8.

[75] Y.H. Zhao, S.B. Lin, F.X. Qu, L. Wu, Influence of pin geometry on material flow in friction stir welding process, Mater. Sci. Technol. 22 (2006) 45–50. https://doi.org/10.1179/174328406X78424.

[76] E.R.I. Mahmoud, M. Takahashi, T. Shibayanagi, K. Ikeuchi, Effect of friction stir processing tool probe on fabrication of SiC particle reinforced composite on aluminium surface, Sci. Technol. Weld. Join. 14 (2009) 413–425. https://doi.org/10.1179/136217109X406974.

[77] R. Nandan, G.G. Roy, T. Debroy, Numerical simulation of three dimensional heat transfer and plastic flow during friction stir welding, Metall. Mater. Trans. A Phys. Metall. Mater. Sci. 37 (2006) 1247–1259. https://doi.org/10.1007/s11661-006-1076-9.

[78] M.A. Sutton, B. Yang, A.P. Reynolds, R. Taylor, Microstructural studies of friction stir welds in 2024-T3 aluminum, Mater. Sci. Eng. A. 323 (2002) 160–166. https://doi.org/10.1016/S0921-5093(01)01358-2.

[79] K.N. Krishnan, On the formation of onion rings in friction stir welds, Mater. Sci. Eng. A. 327 (2002) 246–251. https://doi.org/10.1016/S0921-5093(01)01474-5.

[80] M.W. Mahoney, C.G. Rhodes, J.G. Flintoff, R.A. Spurling, W.H. Bingel, Properties of friction-stir-welded 7075 T651 aluminum, Metall. Mater. Trans. A Phys. Metall. Mater. Sci. 29 (1998) 1955–1964. https://doi.org/10.1007/s11661-998-0021-5.

[81] J.A. Schneider, A.C. Nunes, Characterization of plastic flow and resulting microtextures in a friction stir weld, Metall. Mater. Trans. B Process Metall. Mater. Process. Sci. 35 (2004) 777–783. https://doi.org/10.1007/s11663-004-0018-4.

[82] P.L. Threadgilll, A.J. Leonard, H.R. Shercliff, P.J. Withers, Friction stir welding of aluminium alloys, Int. Mater. Rev. 54 (2009) 49–93. https://doi.org/10.1179/174328009X411136.

[83] Y.H. Yin, N. Sun, T.H. North, S.S. Hu, Microstructures and mechanical properties in dissimilar AZ91/AZ31 spot welds, Mater. Charact. 61 (2010) 1018–1028. https://doi.org/10.1016/j.matchar.2010.06.016.

[84] A. Gerlich, M. Yamamoto, T.H. North, Local melting and tool slippage during friction stir spot welding of Al-alloys, J. Mater. Sci. 43 (2008) 2–11. https://doi.org/10.1007/s10853-007-1791-7.

[85] T.U. Seidel, A.P. Reynolds, Visualization of the material flow in AA2195 friction-stir welds using a marker insert technique, Metall. Mater. Trans. A Phys. Metall. Mater. Sci. 32 (2001) 2879–2884. https://doi.org/10.1007/s11661-001-1038-1.

[86] L. Fratini, G. Buffa, D. Palmeri, J. Hua, R. Shivpuri, Material flow in FSW of AA7075-T6 butt joints: Numerical simulations and experimental verifications, Sci. Technol. Weld. Join. 11 (2006) 412–421. https://doi.org/10.1179/174329306X113271.

[87] Y. Morisada, H. Fujii, Y. Kawahito, K. Nakata, M. Tanaka, Three-dimensional visualization of material flow during friction stir welding by two pairs of X-ray transmission systems, Scr. Mater. 65 (2011) 1085–1088. https://doi.org/10.1016/j.scriptamat.2011.09.021.

[88] P.A. Colegrove, H.R. Shercliff, Experimental and numerical analysis of aluminium alloy 7075-T7351 friction stir welds, Sci. Technol. Weld. Join. 8 (2003) 360–368. https://doi.org/10.1179/136217103225005534.

[89] A. Bastier, M.H. Maitournam, K. Dang Van, F. Roger, Steady state thermomechanical modelling of friction stir welding, Sci. Technol. Weld. Join. 11 (2006) 278–288. https://doi.org/10.1179/174329306X102093.

[90] S. Xu, X. Deng, A.P. Reynolds, T.U. Seidel, Finite element simulation of material flow in friction stir welding, Sci. Technol. Weld. Join. 6 (2001) 191–193. https://doi.org/10.1179/136217101101538640.

[91] B.C. Liechty, B.W. Webb, The use of plasticine as an analog to explore material flow in friction stir welding, J. Mater. Process. Technol. 184 (2007) 240–250. https://doi.org/10.1016/j.jmatprotec.2006.10.049.

[92] Q. Yang, S. Mironov, Y.S. Sato, K. Okamoto, Material flow during friction stir spot welding, Mater. Sci. Eng. A. 527 (2010) 4389–4398. https://doi.org/10.1016/j.msea.2010.03.082.

[93] S.K. Park, S.T. Hong, J.H. Park, K.Y. Park, Y.J. Kwon, H.J. Son, Effect of material locations on properties of friction stir welding joints of dissimilar aluminium alloys, Sci. Technol. Weld. Join. 15 (2010) 331–336. https://doi.org/10.1179/136217110X12714217309696.

[94] P. Su, A. Gerlich, T.H. North, G.J. Bendzsak, Intermixing in dissimilar friction stir spot welds, Metall. Mater. Trans. A Phys. Metall. Mater. Sci. 38 (2007) 584–595. https://doi.org/10.1007/s11661-006-9067-4.

[95] A. Gerlich, P. Su, M. Yamamoto, T.H. North, Material flow and intermixing during dissimilar friction stir welding, Sci. Technol. Weld. Join. 13 (2008) 254–264. https://doi.org/10.1179/174329308X283910.

[96] R.S. Mishra, Z.Y. Ma, I. Charit, Friction stir processing : a novel technique for fabrication of surface composite, Mater. Sci. Eng. A. 341 (2003) 1–4.

[97] C. HU, T.. BAKER, Laser processing to create in-situ Al-SiC surface metal matrix composites, J. Mater. Sci. 30 (1995) 891–897.

[98] A. Shafiei-Zarghani, S.F. Kashani-Bozorg, A. Zarei-Hanzaki, Microstructures and mechanical properties of Al/Al2O3 surface nano-composite layer produced by friction stir processing, Mater. Sci. Eng. A. 500 (2009) 84–91. https://doi.org/10.1016/j.msea.2008.09.064.

[99] Z.Y. Ma, R.S. Mishra, M.W. Mahoney, Superplastic deformation behaviour of friction stir processed 7075 Al alloy, Acta Mater. 50 (2002) 4419–4430. https://doi.org/10.1016/S1359-6454(02)00278-1.

[100] L.B. Johannes, I. Charit, R.S. Mishra, R. Verma, Enhanced superplasticity through friction stir processing in continuous cast AA5083 aluminum, Mater. Sci. Eng. A. 464 (2007) 351–357. https://doi.org/10.1016/j.msea.2007.02.012.

[101] F.C. Liu, Z.Y. Ma, Low-temperature superplasticity of friction stir processed Al-Zn-Mg-Cu alloy, Scr. Mater. 58 (2008) 667–670. https://doi.org/10.1016/j.scriptamat.2007.11.044.

[102] H.S. Park, T. Kimura, T. Murakami, Y. Nagano, K. Nakata, M. Ushio, Microstructures

and mechanical properties of friction stir welds of 60% Cu-40% Zn copper alloy, Mater. Sci. Eng. A. 371 (2004) 160–169. https://doi.org/10.1016/j.msea.2003.11.030.

[103] D. Zhang, M. Suzuki, K. Maruyama, Microstructural evolution of a heat-resistant magnesium alloy due to friction stir welding, Scr. Mater. 52 (2005) 899–903. https://doi.org/10.1016/j.scriptamat.2005.01.003.

[104] A.P. Reynolds, E. Hood, W. Tang, Texture in friction stir welds of Timetal 21S, Scr. Mater. 52 (2005) 491–494. https://doi.org/10.1016/j.scriptamat.2004.11.009.

[105] Y.S. Sato, A. Sasaki, A. Sugimoto, A. Honda, H. Kokawa, Enhancement of Formability in Magnesium Alloy AZ31B via Friction Stir Processing, Mater. Sci. Forum. 539–543 (2007) 3775–3780. https://doi.org/10.4028/www.scientific.net/msf.539-543.3775.

[106] Z.Y. Ma, A.L. Pilchak, M.C. Juhas, J.C. Williams, Microstructural refinement and property enhancement of cast light alloys via friction stir processing, Scr. Mater. 58 (2008) 361–366. https://doi.org/10.1016/j.scriptamat.2007.09.062.

[107] A.H. Feng, Z.Y. Ma, Enhanced mechanical properties of Mg-Al-Zn cast alloy via friction stir processing, Scr. Mater. 56 (2007) 397–400. https://doi.org/10.1016/j.scriptamat.2006.10.035.

[108] K. Oh-Ishi, T.R. McNelley, Microstructural modification of as-cast NiAl bronze by friction stir processing, Metall. Mater. Trans. A Phys. Metall. Mater. Sci. 35 A (2004) 2951–2961. https://doi.org/10.1007/s11661-004-0242-1.

[109] K. Oh-Ishi, T.R. McNelley, The influence of friction stir processing parameters on microstructure of as-cast NiAl bronze, Metall. Mater. Trans. A Phys. Metall. Mater. Sci. 36 (2005) 1575–1585. https://doi.org/10.1007/s11661-005-0249-2.

[110] J.A. DUMA, Heat Treatments for Optimizing Mechanical and Corrosion Resisting Properties of Nickel-Aluminum Bronzes, Nav. Eng. J. 87 (1975) 45–64. https://doi.org/10.1111/j.1559-3584.1975.tb05527.x.

[111] E.R.I. Mahmoud, M. Takahashi, T. Shibayanagi, K. Ikeuchi, Wear characteristics of surface-hybrid-MMCs layer fabricated on aluminum plate by friction stir processing, Wear. 268 (2010) 1111–1121. https://doi.org/10.1016/j.wear.2010.01.005.

[112] A. Mertens, A. Simar, J. Adrien, E. Maire, H.M. Montrieux, F. Delannay, J. Lecomte-Beckers, Influence of fibre distribution and grain size on the mechanical behaviour of friction stir processed Mg-C composites, Mater. Charact. 107 (2015) 125–133. https://doi.org/10.1016/j.matchar.2015.07.010.

[113] G. Madhusudhan Reddy, A. Sambasiva Rao, K. Srinivasa Rao, Friction stir processing for enhancement of wear resistance of ZM21 magnesium alloy, Trans. Indian Inst. Met.

66 (2013) 13–24. https://doi.org/10.1007/s12666-012-0163-4.

[114] A.K. Srivastava, N.K. Maurya, A.R. Dixit, S.P. Dwivedi, A. Saxena, M. Maurya, Experimental investigations of A359/Si3N4 surface composite produced by multi-pass friction stir processing, Mater. Chem. Phys. 257 (2021) 123717. https://doi.org/10.1016/j.matchemphys.2020.123717.

[115] R.M. Miranda, T.G. Santos, J. Gandra, N. Lopes, R.J.C. Silva, Reinforcement strategies for producing functionally graded materials by friction stir processing in aluminium alloys, J. Mater. Process. Technol. 213 (2013) 1609–1615. https://doi.org/10.1016/j.jmatprotec.2013.03.022.

[116] Y. Hangai, Y. Oba, Fabrication of A1050-A6061 Functionally Graded Aluminum Foam by Friction Stir Processing Route, Metall. Mater. Trans. A. 42 (2011) 3585–3589. https://doi.org/10.1007/s11661-011-0944-0.

[117] J. Gandra, R. Miranda, P. Vilaa, A. Velhinho, J.P. Teixeira, Functionally graded materials produced by friction stir processing, J. Mater. Process. Technol. 211 (2011) 1659–1668. https://doi.org/10.1016/j.jmatprotec.2011.04.016.

[118] A. Moradi Faradonbeh, M. Shamanian, H. Edris, M. Paidar, Y. Bozkurt, Friction Stir Welding of Al-B4C Composite Fabricated by Accumulative Roll Bonding: Evaluation of Microstructure and Mechanical Behavior, J. Mater. Eng. Perform. 27 (2018) 835–846. https://doi.org/10.1007/s11665-018-3131-2.

[119] M. Paidar, A. Asgari, O.O. Ojo, A. Saberi, Mechanical Properties and Wear Behavior of AA5182/WC Nanocomposite Fabricated by Friction Stir Welding at Different Tool Traverse Speeds, J. Mater. Eng. Perform. 27 (2018) 1714–1724. https://doi.org/10.1007/s11665-018-3297-7.

[120] N. Pol, G. Verma, R.P. Pandey, T. Shanmugasundaram, Fabrication of AA7005/TiB2-B4C surface composite by friction stir processing: Evaluation of ballistic behaviour, Def. Technol. 15 (2019) 363–368. https://doi.org/10.1016/j.dt.2018.08.002.

[121] D.K. Sharma, V. Patel, V. Badheka, K. Mehta, G. Upadhyay, Fabrication of Hybrid Surface Composites AA6061/(B4C + MoS2) via Friction Stir Processing, J. Tribol. 141 (2019) 1–10. https://doi.org/10.1115/1.4043067.

[122] M. Paidar, O.O. Ojo, H.R. Ezatpour, A. Heidarzadeh, Influence of multi-pass FSP on the microstructure, mechanical properties and tribological characterization of Al/B 4 C composite fabricated by accumulative roll bonding (ARB), Surf. Coatings Technol. 361 (2019) 159–169. https://doi.org/10.1016/j.surfcoat.2019.01.043.

[123] N. Gangil, S. Maheshwari, A.N. Siddiquee, M.H. Abidi, M.A. El-Meligy, J.A.

Mohammed, Investigation on friction stir welding of hybrid composites fabricated on Al-Zn-Mg-Cu alloy through friction stir processing, J. Mater. Res. Technol. 8 (2019) 3733–3740. https://doi.org/10.1016/j.jmrt.2019.06.033.

[124] V.K.S. Jain, J. Varghese, S. Muthukumaran, Effect of First and Second Passes on Microstructure and Wear Properties of Titanium Dioxide-Reinforced Aluminum Surface Composite via Friction Stir Processing, Arab. J. Sci. Eng. 44 (2019) 949–957. https://doi.org/10.1007/s13369-018-3312-1.

[125] C.V. Singh, P. Pachauri, S.P. Dwivedi, S. Sharma, R.M. Singari, Formation of functionally graded hybrid composite materials with Al2O3 and RHA reinforcements using friction stir process, Aust. J. Mech. Eng. 00 (2019) 1–14. https://doi.org/10.1080/14484846.2019.1679583.

[126] M. Barati, M. Abbasi, M. Abedini, The effects of friction stir processing and friction stir vibration processing on mechanical, wear and corrosion characteristics of Al6061/SiO2 surface composite, J. Manuf. Process. 45 (2019) 491–497. https://doi.org/10.1016/j.jmapro.2019.07.034.

[127] M. Saadatmand, J.A. Mohandesi, Comparison between wear resistance of functionally graded and homogenous Al-SiC nanocomposite produced by friction stir processing (FSP), J. Mater. Eng. Perform. 23 (2014) 736–742. https://doi.org/10.1007/s11665-013-0839-x.

[128] K. Colligan, Material flow behavior during friction stir welding of aluminum, Weld. J. (Miami, Fla). 78 (1999) 229-s.

[129] G.R. Cui, Z.Y. Ma, S.X. Li, The origin of non-uniform microstructure and its effects on the mechanical properties of a friction stir processed Al-Mg alloy, Acta Mater. 57 (2009) 5718–5729. https://doi.org/10.1016/j.actamat.2009.07.065.

[130] Leica Application Suite | Products | Leica Microsystems, (n.d.). https://www.leica-microsystems.com/products/microscope-software/p/leica-application-suite/downloads/ (accessed April 18, 2020).

[131] M. Paidar, M.L. Sarab, Friction stir spot welding of 2024-T3 aluminum alloy with SiC nanoparticles, J. Mech. Sci. Technol. 30 (2016) 365–370. https://doi.org/10.1007/s12206-015-1241-4.

[132] M. BARMOUZ, M.K. BESHARATI GIVI, J. SEYFI, On the role of processing parameters in producing Cu/SiC metal matrix composites via friction stir processing: Investigating microstructure, microhardness, wear and tensile behavior, Mater. Charact. 62 (2011) 108–117. https://doi.org/10.1016/j.matchar.2010.11.005.

[133] S. RATHEE, S. MAHESHWARI, A.N. SIDDIQUEE, M. SRIVASTAVA, Investigating the Effects of SiC Particle Sizes on Microstructural and Mechanical Properties of AA5059/SiC Surface Composites During Multi-Pass FSP, Silicon. 11 (2019) 797–805. https://doi.org/10.1007/s12633-018-9958-1.

[134] A. ABDOLAHZADEH, H. OMIDVAR, M.A. SAFARKHANIAN, M. BAHRAMI, Studying microstructure and mechanical properties of SiC-incorporated AZ31 joints fabricated through FSW: the effects of rotational and traveling speeds, Int. J. Adv. Manuf. Technol. 75 (2014) 1189–1196. https://doi.org/10.1007/s00170-014-6205-9.

[135] H.S. Arora, H. Singh, B.K. Dhindaw, Composite fabrication using friction stir processing - A review, Int. J. Adv. Manuf. Technol. 61 (2012) 1043–1055. https://doi.org/10.1007/s00170-011-3758-8.

[136] U. Rokkala, S. Bontha, M.R. Ramesh, V.K. Balla, A. Srinivasan, S. V. Kailas, Tailoring surface characteristics of bioabsorbable Mg-Zn-Dy alloy using friction stir processing for improved wettability and degradation behavior, J. Mater. Res. Technol. 12 (2021) 1530–1542. https://doi.org/10.1016/j.jmrt.2021.03.057.

[137] S.M. ARAB, S. KARIMI, S.A.J. JAHROMI, S. JAVADPOUR, S.M. ZEBARJAD, Fabrication of novel fiber reinforced aluminum composites by friction stir processing, Mater. Sci. Eng. A. 632 (2015) 50–57. https://doi.org/10.1016/j.msea.2015.02.032.

[138] K. ELANGOVAN, V. BALASUBRAMANIAN, M. VALLIAPPAN, Effect of tool pin profile and tool rotational speed on mechanical properties of friction stir welded AA6061 aluminium alloy, Mater. Manuf. Process. 23 (2008) 251–260. https://doi.org/10.1080/10426910701860723.

[139] H. EFTEKHARINIA, A.A. AMADEH, A. KHODABANDEH, M. PAIDAR, Microstructure and wear behavior of AA6061/SiC surface composite fabricated via friction stir processing with different pins and passes, Rare Met. (2016) 1–7. https://doi.org/10.1007/s12598-016-0691-x.

[140] R. SATHISKUMAR, N. MURUGAN, I. DINAHARAN, S.J. VIJAY, Role of friction stir processing parameters on microstructure and microhardness of boron carbide particulate reinforced copper surface composites, Sadhana - Acad. Proc. Eng. Sci. 38 (2013) 1433–1450. https://doi.org/10.1007/s12046-013-0184-7.

[141] Y.S. SATO, S.H.C. PARK, H. KOKAWA, Microstructural factors governing hardness in friction-stir welds of solid-solution-hardened Al alloys, Metall. Mater. Trans. A Phys. Metall. Mater. Sci. 32 (2001) 3033–3042. https://doi.org/10.1007/s11661-001-0178-7.

[142] J.F. Archard, Contact and Rubbing of Flat Surfaces, J. Appl. Phys. 24 (1953) 981–988.

https://doi.org/10.1063/1.1721448.

[143] K. Elangovan, V. Balasubramanian, Influences of tool pin profile and tool shoulder diameter on the formation of friction stir processing zone in AA6061 aluminium alloy, Mater. Des. 29 (2008) 362–373. https://doi.org/10.1016/j.matdes.2007.01.030.

[144] M. Reza-E-Rabby, W. Tang, A.P. Reynolds, Effects of thread interruptions on tool pins in friction stir welding of AA6061, Sci. Technol. Weld. Join. 23 (2018) 114–124. https://doi.org/10.1080/13621718.2017.1341363.

[145] C.V. Singh, P. Pachauri, S.P. Dwivedi, S. Sharma, R.M. Singari, Formation of functionally graded hybrid composite materials with Al2O3 and RHA reinforcements using friction stir process, Aust. J. Mech. Eng. 00 (2019) 1–14. https://doi.org/10.1080/14484846.2019.1679583.

[146] J. Epp, X-Ray Diffraction (XRD) Techniques for Materials Characterization, Elsevier Ltd, 2016. https://doi.org/10.1016/B978-0-08-100040-3.00004-3.

[147] M.M. Moradi, H. Jamshidi Aval, R. Jamaati, Effect of tool pin geometry and weld pass number on microstructural, natural aging and mechanical behaviour of SiC-incorporated dissimilar friction-stir-welded aluminium alloys, Sadhana - Acad. Proc. Eng. Sci. 44 (2019) 1–9. https://doi.org/10.1007/s12046-018-0997-5.

[148] F. Khodabakhshi, A.P. Gerlich, P. Švec, Fabrication of a high strength ultra-fine grained Al-Mg-SiC nanocomposite by multi-step friction-stir processing, Mater. Sci. Eng. A. 698 (2017) 313–325. https://doi.org/10.1016/j.msea.2017.05.065.

[149] A. Kumar, L.S. Raju, Influence of tool pin profiles on friction stir welding of copper, Mater. Manuf. Process. 27 (2012) 1414–1418. https://doi.org/10.1080/10426914.2012.689455.

[150] S.A. Hosseini, K. Ranjbar, R. Dehmolaei, A.R. Amirani, Fabrication of Al5083 surface composites reinforced by CNTs and cerium oxide nano particles via friction stir processing, J. Alloys Compd. 622 (2015) 725–733. https://doi.org/10.1016/j.jallcom.2014.10.158.

[151] A. Devaraju, A. Kumar, B. Kotiveerachari, Influence of addition of Grp/Al2O3p with SiCp on wear properties of aluminum alloy 6061-T6 hybrid composites via friction stir processing, Trans. Nonferrous Met. Soc. China (English Ed. 23 (2013) 1275–1280. https://doi.org/10.1016/S1003-6326(13)62593-5.

[152] T.R. McNelley, S. Swaminathan, J.Q. Su, Recrystallization mechanisms during friction stir welding/processing of aluminum alloys, Scr. Mater. 58 (2008) 349–354. https://doi.org/10.1016/j.scriptamat.2007.09.064.

[153] J. Peng, Z. Zhang, J. Huang, P. Guo, Y. Li, W. Zhou, Y. Wu, The effect of the inhomogeneous microstructure and texture on the mechanical properties of AZ31 Mg alloys processed by friction stir processing, J. Alloys Compd. 792 (2019) 16–24. https://doi.org/10.1016/j.jallcom.2019.04.014.

[154] J.A. Calderón, J.E. Henao, M.A. Gómez, Erosion-corrosion resistance of Ni composite coatings with embedded SiC nanoparticles, Electrochim. Acta. 124 (2014) 190–198. https://doi.org/10.1016/j.electacta.2013.08.185.

[155] M.A. Almomani, W.R. Tyfour, M.H. Nemrat, Effect of silicon carbide addition on the corrosion behavior of powder metallurgy Cu-30Zn brass in a 3.5 wt% NaCl solution, J. Alloys Compd. 679 (2016) 104–114. https://doi.org/10.1016/j.jallcom.2016.04.006.

[156] F. Baradarani, A. Mostafapour, M. Shalvandi, Enhanced corrosion behavior and mechanical properties of AZ91 magnesium alloy developed by ultrasonic-assisted friction stir processing, Mater. Corros. 71 (2020) 109–117. https://doi.org/10.1002/maco.201911084.

[157] P. Vijayavel, V. Balasubramanian, Effect of pin profile volume ratio on microstructure and tensile properties of friction stir processed aluminum based metal matrix composites, J. Alloys Compd. 729 (2017) 828–842. https://doi.org/10.1016/j.jallcom.2017.09.117.

Research outcomes

Papers published in journals

1. Bikkina, Venkatesh, Sadasiva Rao Talasila, and Kumar Adepu. "Characterization of aluminum based functionally graded composites developed via friction stir processing." *Transactions of Nonferrous Metals Society of China* 30.7 (2020): 1743-1755. (SCI Expanded, I.F: 2.917)
2. Bikkina, Venkatesh, Sadasiva Rao Talasila, and Kumar Adepu. "Improvement of Mechanical and Corrosion Properties of Al/SiC Functionally Graded Material Using a Novel Hybrid Tool in Friction Stir Processing." *Silicon* (2021): 1-17. (SCI Expanded, I.F: 2.670)
3. Bikkina, Venkatesh, Sadasiva Rao Talasila, and Kumar Adepu. "Influence of hybrid pin profile on microstructural and mechanical properties of Al/SiC graded composites produced by friction stir processing." *Journal of Physics: Conference Series*. Vol. 2070. No. 1. IOP Publishing, 2021. (SCOPUS)
4. Bikkina, Venkatesh, Sadasiva Rao Talasila, and Kumar Adepu. "Investigating the effects of tool offset distance and SiC particles on microstructural and mechanical properties of AA6082/SiC composites via friction stir processing" *Materials today proceedings, 2021* (SCOPUS-accepted)

Papers presented in conference

1. Venkatesh, B., T. Sadasiva Rao, and Adepu Kumar. *"Fabrication and Characterization of Functionally Graded Composites Using Friction Stir Processing."* (ICAMER-2019), NIT Warangal.